ASSESSMENT OF TRANSIENT EFFECTS IN DIESEL INJECTORS AFFECTED BY FOULING AND CAVITATION EROSION

Konstantinos Kolovos

Thesis submitted for the degree of Doctor of Philosophy

City, University of London

School of Mathematics, Computer Science and Engineering

London, UK

March 2021

Contents

Nomenclature

English Symbols

A	Surface	[m^2]	M	Mach number	-
a	blending coefficient	**-**	n	Liquid-dependent constant	-
B	liquid stiffness/elasticity	[Pa]	**n**	Surface normal vector	-
c	Speed of sound	[m/s]	p	Pressure	[Pa]
C_1	Acoustic impedance	[Pa kg/m^3]	Re	Reynolds number	-
C_d	Discharge Coefficient	-	s	entropy	[J/kg K]
C_w	LES model constant	-	S_t	Strouhal number	-
cp	Heat capacity	[J/kgK]			
D	diameter	[m]	T	Temperature	[K]
d_{wall}	Wall distance	[m]			
e	Internal energy	[J/kg]			
E	Total energy	[J/kg]	t	Time	[s]
h_0	Total Enthalpy	[J/kg]	**u**	Velocity vector	[m/s]
k	Thermal conductivity	W/(m K)	$\mathbf{u_g}$	Grid velocity vector	[m/s]
k_B	Boltzmann constant	[J/K]	$\mathbf{u_r}$	Relative velocity vector	[m/s]
k_{ij}	binary interaction parameter	-	V	cell volume	[m^3]
k	von Karman constant	-	vf,	Vapour Volume Fraction	-
L	WALE LES model length scale	[m]	x	Vapour mass composition	-
L_c	Characteristic length	[m]	z	Total mass composition	-

Greek Symbols

β	weighted term fifor the hybrid flux	-	ρ	Density	[kg/m^3]
λ_g	Taylor length scale	[m]	σ	segment diameter	[A]
μ	Dynamic viscosity	[Pa.s]	τ	Stress tensor	[Pa]
σ	segment diameter	[A]	θ	Mass vapour fraction	-

Subscripts

b	Downstream conditions/boiling point	L	Liquid
comp	compressible	V	Vapour
eff	effective	out	exit of the orifice
i	component i/coordinate direction	R	Right side
inc	incompressible	S	Isentropic
f	face	sat	saturation
In or inj	inlet of injector	t	Turbulent

Abbreviations

ALE	Arbitrary Lagrangian–Eulerian	PC-SAFT	Perturbed Chain Statistical Associating Fluids Theory
CN	Cavitation Number	PVRS	Primitive Variable Riemann Solver
EoS	Equation of State	SCL	Space Conservation Law
HEM	Homogenous Equilibrium Model	URANS	Unsteady Reynolds-averaged Navier–Stokes
LES	Large Eddy Simulation	VLE	Vapour Liquid Equilibrium
nc	number of components	WALE	Wall Adapted Large Eddy
NS	Navier-Stokes		

Acknowledgements

More than anything else, I would like to express my deep gratitude to Prof. Manolis Gavaises and Dr. Robert M. McDavid to give me this unique chance to join City University academic group. Also, I am especially grateful for their auspices, trust, motivation, continuous support, guidance and the freedom they gave me to do this research. I thank Dr. Phoevos Koukouvinis, Dr. Ioannis Karathanassis and Dr. Nikolaos Kyriazis for transferring to me their scientific knowledge. I will be thankful to Dr. Carlos Rodriguez who has been helpful in providing advice many times during these years and he was and remains my best role model for a scientist and colleague. I would also like to thank my colleagues Wang Chuqiao, Akis Stavropoulos-Vasilakis, Thodoris Lyras, Hesam Jadidbonab, Milad Heidari Koochi, Georgia Nykteri, Andreas Papoutsakis, Homa Naseri, Mithun Murali Girija, Carlos Rodriguez, Alvaro Vidal and Max Brunhart and all those who contributed directly or indirectly to this work, for the days we spent for their cooperation and the times we spend in the discussing about scientific research. Also, I would like to thank Amalia Petrova for her support and guidance. I wish to thank Nikos Chatziarsenis for helping me to resolve administrative issues.

Most importantly, I thank my parents Nikolaos Kolovos and Konstantina Kolovou for their confidence, sacrifice and their love during all these years and my sisters Dimitra and Politimi Kolovou for their motivation and courage which gave me to overcome all the difficulties during this work. I would especially like to express my warmest thanks to my dear friend L.F, who has always stood by me, supported me, encouraged me and helped me overcoming the difficulties without complaining and without this support I would never have finished this work. Equally important was the support, kindness and help from my close and supportive friends Gianluca Donato Sante Di Muro, Themis Melissaris, Kostas Kritikos, Giannis Patsis and Ilektra-Georgia Apostolidou. This research has been funded by the European Union Horizon-2020 Research and Innovation Programme, Grant Agreement No. 675528.

Konstantinos Kolovos, London April 2021

Thesis contribution

• **Arbitrary Lagrangian–Eulerian (ALE) formulation**: The explicit density-based flow solver is based previous works but extended here to include moving grids. The numerical model employs a set of conservation equations governing the fluid motion, re-casted in a form of space conservation law suitable for moving/deforming meshes using a cell-based mesh Arbitrary Lagrangian–Eulerian (ALE) formulation is used for modelling the injector's needle valve movement.

• **Modified Mach consistent numerical flux**: The modified hybrid numerical flux has been implemented in OF and tested for several cases. The initial numerical flux is a combination of approximate Riemann solvers and previously proposed flux functions. This numerical flux renders the solver stable and accurate especially during the early opening and closing phases.

• **Simulation of transient thermal effects in a fuel injector nozzle using real-fluid thermodynamic closure**: Comparison between a tabulated data approach for a 4-component Diesel fuel surrogate, derived from the Perturbed-Chain, Statistical Associating Fluid Theory (PC-SAFT) Equation of State (EoS) and a widely used barotropic Equation of State (EoS). It revealed that the needle motion affects the thermal boundary layer and possibly the inception and cavity sheet growth and transition, especially at low lifts. Also, it revealed the coherent vortex cavitation structures, their origin and their effects to potential erosion location.

• **Simulation of transient effects in a fuel injector nozzle using real-fluid thermodynamic closure up to 450MPa**: Parametric investigation of the effect of injection pressure (180MPa, 350MPa and 450MPa) using the aforementioned thermodynamic closure. It revealed that with increasing injection pressures, an unprecedented decrease of cavitation volume fraction inside the fuel injector occurs. There is no relevant simulations or experiments reported for cavitation and induced erosion, while considering variable fuel properties due to temperature/pressure gradients, and incorporating transient effects caused by the motion of the needle valve.

Abstract

An explicit density-based solver of the compressible Navier-Stokes (NS) and energy conservation equations has been developed and implemented in the open-source CFD code OpenFOAM®®; the flow solver is combined with two thermodynamic closure models for the liquid, vapor and vapor liquid equilibrium (VLE) property variation as function of pressure and temperature. The first is based on tabulated data for a 4-component Diesel fuel surrogate, derived from the Perturbed-Chain, Statistical Associating Fluid Theory (PC-SAFT) Equation of State (EoS), allowing for thermal effects to be quantified. The second thermodynamic closure is based on the widely used barotropic Equation of State (EoS) approximation between density and pressure and neglects viscous heating. The Wall Adapting Local Eddy viscosity (WALE) LES model was used to resolve sub-grid scale turbulence while a cell-based mesh deformation Arbitrary Lagrangian–Eulerian (ALE) formulation is used for modelling the injector's needle valve movement. Numerical predictions of the fuel heating and cavitation erosion location indicators occurring during the opening and closing periods of the needle valve inside a five-hole common rail Diesel fuel injector are presented. Model predictions are found in close agreement against 0-D estimates of the temporal variation of the fuel temperature difference between the feed and hole exit during the injection period. Two mechanisms affecting the temperature distribution within the fuel injector have been revealed and quantified. The first is ought to wall friction-induced heating, which may result to local liquid temperature increase up to fuel's boiling point while superheated vapor is formed. At the same time, liquid expansion due to the depressurisation of the injected fuel results to liquid cooling relative to the fuel's feed temperature; this is occurring at the central part of the injection orifice. The formed spatial and temporal temperature and pressure gradients induce significant variations in the fuel density and viscosity, which in turn, affect the formed coherent vortical flow structures. It is found, in particular, that these affect the locations of cavitation formation and collapse, that may lead to erosion of the surfaces of the needle valve, sac volume and injection holes. Model predictions are compared against corresponding X-ray surface erosion images obtained from injector durability tests, showing good agreement.

Further, investigation of the fuel heating, vapor amount formation and cavitation erosion location patterns occurring during the early opening period of the needle valve (from 2μm to 80μm) inside a five-hole common rail Diesel fuel injector discharging at 180MPa, 350MPa and

450MPa, are presented. These have been obtained using an explicit density-based solver of the compressible Navier-Stokes (NS) and energy conservation equations; the flow solver is combined with tabulated property data for a 4-component Diesel fuel surrogate, derived from the Perturbed-Chain, Statistical Associating Fluid Theory (PC-SAFT) Equation of State (EoS), allowing for the significant variation of the fuel's physical and transport properties to be quantified. The Wall Adapting Local Eddy viscosity (WALE) LES model was used to resolve sub-grid scale turbulence while a cell-based mesh deformation Arbitrary Lagrangian–Eulerian (ALE) formulation is used for modelling the injector's needle valve movement. Emphasis is placed on the temperature and vapor volume fraction evolution in needle seat passage. Friction-induced heating has been found to increase significantly with increasing pressure drop, especially at needle valve lifts from 2μm to 40μm. At the same time, liquid cooling is occurring due to fuel expansion at the areas of bulk flow away from walls; up to 25 degrees local fuel temperature drop relative to the fuel's feed temperature are calculated. As the needle valve reaches 80 μm the fuel vapor volume, the average temperature into this flow passage and at the exit of the orifice converge to the same values for all injection pressures. The extreme injection pressures induce fuel's jet velocity magnitude of the order of 1100 m/s, which in turn, affect the formation of coherent vortical flow structures into the nozzle's sac volume. It is found, in particular, that the fuel jet velocity variations with increasing discharge pressure, affect the locations of cavitation formation and collapse, which in turn, lead to different potential locations of erosion of the surface of the needle valve.

Thesis Structure

Three journals have been published in which I was the first author during my research period. This thesis is a compilation of all three journals which form a prospective publication format. Basic introduction on recent experimental and CFD studies for Diesel injectors and the objectives of this study are given in Chapter-1, followed by each publication as a separate chapter which will generally contain the following sections: (1) Abstract (2) Introduction with literature review (3) Large-eddy simulation of friction heating and turbulent cavitating flow in a Diesel injector including needle movement (4) Transient cavitation and friction-induced heating effects of diesel fuel during the needle valve early opening stages for discharge pressures up to 450MPa , (5) Preferential cavitation and friction-induced heating of multi-component Diesel fuel surrogates up to 450MPa', (6) Results and (7) Discussion and Conclusions.

Publications

Konstantinos Kolovos, Nikolaos Kyriazis, Phoevos Koukouvinis, Manolis Gavaises, Jason Z. Li, Robert M. McDavid **'Large-eddy simulation of friction heating and turbulent cavitating flow in a Diesel injector including needle movement', Applications in Energy and Combustion Science, Volum 7, Sep 2021, https://doi.org/10.1016/j.jaecs.2021.100037.**

- Comparison between two thermodynamic closure models for the liquid, vapor and vapor liquid equilibrium (VLE) property variation. The first is based on tabulated data for a 4-component Diesel fuel surrogate, derived from the Perturbed-Chain, Statistical Associating Fluid Theory (PC-SAFT) Equation of State (EoS), allowing for thermal effects to be quantified. The second thermodynamic closure is based on the widely used barotropic Equation of State (EoS) approximation between density and pressure and neglects viscous heating.
- Investigation of the transient effects caused by the full motion of the needle valve up to 180 MPa injection pressure.

Konstantinos Kolovos, Phoevos Koukouvinis, Manolis Gavaises **'Transient cavitation and friction-induced heating effects of diesel fuel during the needle valve early opening stages for discharge pressures up to 450MPa', Energies , 14(10), 2923;May 2021, https://doi.org/10.3390/en14102923.**

- Investigation of the transient effects caused by the motion of the needle valve up to 450 MPa injection pressure.
- Address these phenomena and simulate the flow inside a high-pressure Diesel injector discharging at 180MPa, 350MPa and 450MPa considering cavitation and induced erosion, while considering variable fuel properties due to temperature/pressure gradients and incorporating transient effects caused by the motion of the needle valve.

Alvaro Vidal, Konstantinos Kolovos, Martin Gold, Richard Pearson, Phoevos Koukouvinis and Manolis Gavaises **'Preferential cavitation and friction-induced heating of multi-component Diesel fuel surrogates up to 450MPa', Int Journal Heat and Mass Transfer, Vol 166, No 120744, 2021; https://doi.org/10.1016/j.ijheatmasstransfer.2020.120744**

- Investigation of the formation and development of cavitation of a multicomponent Diesel fuel surrogate discharging from a high-pressure fuel injector operating in the range of injection pressures from 60MPa to 450MPa.

- Two approaches have been followed: (i) a barotropic evolution of density as function of pressure, where thermal effects are not considered and (ii) the inclusion of wall friction-induced and pressurisation thermal effects by solving the energy conservation equation. The PC-SAFT equation of state is utilised to derive thermodynamic property tables for an eight-component surrogate based on a grade no.2
- The preferential cavitation of the fuel components within the injector's hole is predicted by Vapor-Liquid Equilibrium calculations; lighter fuel components are found to cavitate to a greater extent than heavier ones.

Konstantinos Kolovos, Nikolaos Kyriazis, Phoevos Koukouvinis, Manolis Gavaises, Jason Z. Li, Robert M. McDavid· **'Large-eddy simulation of turbulent cavitating flow in a Diesel injector including needle movement, two phase cavitation model for Diesel Fuel B0 2015, in OpenFOAM®'**, ***ILASS–Europe 2019, 29th Conference on Liquid Atomization and Spray Systems, 2-4 September 2019, Paris, France,*** https://ilass19.sciencesconf.org/247244/

- This work focuses on potential erosion and on the development vortical structures.
First, the potential erosion regions are predicted though three different indexes, the maximum collapse pressures and the erosion damage model. The latter is coupled with the CFD code. The three indexes are compared with experimental results, from CT scans.

- The structure of the flow is analysed with an emphasis on the interaction between coherent vortical structures and cavitation. The Wall Adapting Local Eddy viscosity (WALE) LES model was used to predict incipient and developed cavitation, while also capturing the shear layer instability, vortex shedding and cavitating vortex formation.

- Moreover, this work revealed the formation of thin and thick string cavitation in the orifice volume and the effects on the flow pattern in the orifice and at the exit of the orifice.

Chapter 1 Introduction

1.1 Fuel injectors

Air pollution, such as soot particles (black carbon), produced in metropolitan areas and megalopolis link to potential short and long term cardiovascular, respiratory and neurodegenerative health effects of black carbon [1]. Additionally, rapid emissions increase is associated with 2°C global warming and potentially warming of 3–4°C with disastrous consequences [2]. Light-duty vehicle liquid fuel demand will be reduced due to increased vehicle efficiency and more electric vehicles. However, the increased commercial activity (bus, rail, plane, truck and marine vessel) will lead to growth transportation fuel demand. Having a large amount of energy, financially affordable and widely available oil will remain the primary transportation fuel [3]. Increased energy efficiency and a shift to lower carbon energy sources will help control CO2 emissions, but not sufficiently to reach a 2°C scenario. To achieve society's emissions aspirations [3] state of the art technologies, innovations and policies will be needed.

For soot capturing different methods like active regeneration or passive Diesel particulate filters are used. Also, cooled exhaust gas recirculation and/or selective catalytic reduction are effective in reducing NOx. Also, use of additives, keeping injectors clean, becomes inevitable in today's engines and in-cylinder soot formation can be significantly reduced when fuel is injected above 2200 bar. Moving forward, investigations with 3000 bar injection pressures reported in show significant soot reductions. Despite the fact that today's nozzles tapered holes known to suppress catastrophic cavitation, at such injection pressures and temperatures cavitation/boiling re-appears unfortunately as an issue even for tapered nozzles [4]. At recent studies injection against the air charge being at supercritical pressure & temperature conditions relative to the liquid fuel reveal that can improve combustion and reduce emissions further [5–8]. However, studies assessing the transient effects of injection of fuels at pressures as high as 4,500 bar under injection conditions, on Diesel Injector cavitation/erosion/boiling are currently missing from the literature.

The increase of the injection pressure constitutes one of three emission reduction strategies in fuel injection systems [9]. Today's commercial fuel injection systems reach 2750 bar while injection pressures as high as 4,500 bar are under investigation. The fuel viscosity could change at an order of magnitude as pressure increases, which and can lead to inaccurate predictions of nozzle discharge coefficient, fuel injected temperature [10] and cavitation [4]. The boiling may take place even in tapered nozzles known to suppress cavitation, due to excess friction and induced heating [4]. Real-size idealised geometries of purpose-built transparent injectors offer optical access and have been used to study flow fields under realistic operating conditions up to 2000 bar [11].

It remains challenging to recognize, understand and simulate cavitation, during this fluid dynamics problem due to complex physical phenomena with different timescales and length scales during this fluid dynamics problem. Cavitation has also a profound impact to fuel atomisation [12]. However, there is only limited information available for realistic nozzle geometries [13–15]. Experiments of Computed Tomography (CT) [16] and X-rays have used to identify the cavitating nozzle flow as a function of injector operation [17–20]. Erosion patterns, eccentric needle motion and even the flow conditions inside the sac volume of the injector during an injection can now be characterized using X-rays. In studies [21–23], visualisation of cavitation in transparent nozzle have been reported and quantitative flow measurements in flow orifices exist [24]. These techniques offer more realistic initial/boundary conditions for subsequent atomisation and simulations. Thus, it becomes a fundamental challenge to simulate real fluid properties including density, viscosity, thermal conductivity, heat capacity and internal energy at injection pressures up to 4,500 bar and temperatures up to the fuel's critical point incorporating the transient's effects of the moving needle. Simulations for the real fuel's properties at pressures as high as 4,500 bar investigating cavitation, vortex cavitation interaction, thermal effects during the early opening and closing injection phases are currently missing from the literature. Similar to challenging thermodynamic modelling for diesel injectors is required in flashing phenomena for cryogenic fuels in aerospace applications for rocket engines towards higher chamber pressures which will result in a higher specific impulse for the engine [25].

In moving-needle high pressure injection systems, the temperature effects are dominant and the complexity of them is driven from the multiphase flow and it's nozzle flow effects. Understanding and predicting cavitation and erosion with the strong interaction between large-scale and micro scale vortex/cavitation dynamics is crucial. The consequence of this co-existence of multi scale flow structures at injection pressures up to 4,500 bar is that none of the thus far developed computational technique addresses that overall, the comparison between different injection pressures shows that there are minor differences in the predicted mean fuel temperature and vapor volume after 60 μm, but significant differences in the temperature distribution and vapor volume inside the sac, needle, and orifice injector regions from 0 to 60 μm. Cavitation often results in violent collapse of the bubbles; pressures may even locally exceed 1GPa [26] producing shock waves strong enough to cause surface erosion.

1.2 State of the art

Unfortunately, such simulations are numerically challenging, especially compressible flow methods and these studies [27–30] represent significant research in CFD. The dynamics of the problem are influenced by the motion and interaction of the discontinuities in the flow (i.e. shock waves, rarefactions and the vapor/liquid contact). For many industrial application simulations, a wide range of cavitation models have been used. Many models are based on a rate equation for the generation of vapor that employs explicit source/sink terms. Vapor production and interaction with the liquid have been used to track the both Eulerian-Eulerian [31–34] and Eulerian-Lagrangian formulations [35,36].

Numerical models like B. Huang et.al and Y Tamura et.al which are available in commercial CFD models utilise the asymptotic or the Rayleigh-Plesset equation representing bubble dynamics [37,38]. They require information on the bubble number density and population present in the liquid and they may include mass transfer between the liquid and the vapor phases and may consider gas content in the liquid but their parameters are case depended. Different, numerical models have incorporated an effective mixture EoS is based on thermodynamic equilibrium assumption, leading to a natural sub-grid scale model able to estimate the vapor volume fraction directly from the cell-averaged fluid state [39].

More specifically, what is missing so far from the state-of-the-art is the coupling of a compressible numerical model and instead of solving a computational demanded EoS at each time step, it will be more efficient to have stored in advance its solution in a thermodynamic mesh so accurately describes real fluid properties at high pressure and high temperature conditions relevant to modern fuel needle moving injection systems. In multiphase compressible flows the speed of sound fluctuates under different flow regime, as a result the flow characterized from subsonic up to supersonic [40]. In pressure-based this fluctuation of speed of sound and the Mach create convergence problems due to the condition number of the numerical system, while in density-based solvers the slow convergence and numerical diffusion are the effects. A unified numerical calculation for low Mach number flows [41,42] and high Mach number [43] is the solution to obtain accurate solutions. But this unified treatment for low and high Mach number often lead to wrong predictions, especially for vortex cavitation [44] which is very sensitive to the numerical diffusion which this treatment could add.

Despite the tremendous progress achieved on the issue of vortex cavitation inside Diesel injectors sac and nozzle volume, one is still unable today to predict its occurrence and development in real size designs under high pressure and high temperature cavitating flows with acceptable accuracy. This modified numerical flux, which under predict the vorticity and cavitation, requires a significant improvement. The motivation of this research lies in understanding and investigating multiphase flows from a numerical point of view and how to control the vortex formation and cavitation in Diesel Injectors.

In general, the numerical approaches for multiphase flow area are unit classified into typical mesh numerical methods and mesh-free approaches. The previous area is classified into inhomogeneous (N-fluid for N phases) and homogeneous (one-fluid) methods. Mesh-free approaches are split into LBM [45] and Particle methods, SPH [46] being the foremost vital among them. Concerning the family of SPH methods, they were originally developed for astrophysical problems [47,48]. However, fifteen years later, SPH was extended to free surface flows by Monaghan [49] and has been widely used for interfacial flows ever since [50,51]. Vila [52] introduced the mathematical framework of the SPH-ALE, thus on overcoming the drawbacks of the standard SPH method. In follow-up studies, Marongiu et al. [53] applied this strategy in the free surface flow of Pelton turbines.

Traditionally, SPH strategies will simply handle material deformation, while not the requirement of mesh deformation techniques and that they provide solutions freed from dissipation. However, they suffer from some serious drawbacks; because of the distribution of the particles within the numerical domain, the order of the spatial accuracy isn't easy and might vary inside the domain. Consequently, in areas with a scarce population of particles or non-uniformly distributed particles, spatial accuracy is downgraded. In multi-component models (inhomogeneous methods) there's no mechanical equilibrium between the phases (nonzero slippery velocity), therefore every section is characterised by its own velocity and pressure field. Though this approach is additional realistic, it's some serious disadvantages in observe, like the high computational cost because of the suitable closure and interface relations required for every phase (N continuity, momentum and energy equations area unit solved for N phases).

On one hand, Wallis in [54] and a 2-fluid model [55] by Baer and Nunziatio are the significant contributions of multi-component models. Saurel and Abgrall [56] extended the two-fluid model for multi-phase compressible flows. On the other hand, in HEM all phases behave as a mixture and there is mechanical equilibrium due to one pressure and one velocity field. This numerical framework is further extended if there is or not thermodynamic equilibrium. Thermodynamic non equilibrium methods are categorized into three different approaches; (1) interface tracking, (2) interface capturing and (3) mass transfer models. In the interface tracking methods, such as the MAC technique, front-tracking methods, the volume-tracking approach and IBM, the moving boundary (interface) predefined or not is calculated by the interface nodes of the computational mesh while the location of the inner mesh nodes, is not prescribed and several techniques are used in order to maintain good computational mesh quality.

In MAC method, the marker particles were used to identify the different fluid regions on a fixed computational domain [57,58] and were implemented for bubble collapse simulations [59] by Plesset and Chapman. The interface is explicitly described by the computational grid in the front tracking methods, which was developed by Glimm et al. [64] and by Unverdi and Tryggvason [60]. FrontTier developed by Glimm et al. [62] is the commonly used package for front tracking methods. FronTier was improved with topological bifurcations and assessed by Du et al. [40] and they assessed the performance of the front-tracking methodology. Front tracking methods resolve accurate the interface between the two phases and it is commonly used for large deformations of the surface to be simulated; in sharp interfaces for large scale problems and model diffuse interfaces in smaller scales problems. The drawbacks are that they cannot capture large topological changes though [61], their complexity, since they are adding or removing nodes in areas of stretched or compressed cells, respectively [60]. For fluid- structure interaction applications the immersed boundary method (IBM) was developed by Peskin [62] and for representing the interface between two phases on Cartesian grids [63]. While The implementation of the IBM is simple from adding a source term in the NS equations and the Eulerian variables represented on a fixed Cartesian mesh and the Lagrangian variables on a freely moving curvilinear mesh however the solid or the interface motion is not accurately described.

Volume of fluid (VOF) [64] is the most characteristic discontinuous interface-capturing method, where the main idea is to calculate the vapor volume fraction which defines the interface as a step function. The most common used continuous interface-capturing methods approach is the level-set method [65,66] where the interface is implicitly reconstructed by a field variable and is described as the zero level-set of some function. Although the VOF method was originally developed and has been mainly used for incompressible flows [64,67,68], it has been also extended to compressible fluids [69–74]. More recently, Shukla et al. [73] solved the multi-component compressible flow equations with an interface compression technique aiming to capture the thickness of the interface within a few cells. Geometric VOF methods with arbitrary unstructured meshes have implemented in software OpenFOAM® [75] and in software Gerris, an open source incompressible VOF solver with adaptive mesh refinement capabilities suitable for droplet or bubble simulations, [76].

A significant disadvantage for interface capturing methods is that they are numerically expensive especially for capturing thousands or millions of bubbles in an industrial case simulation. Also, where liquid and vapor densities become similar, pressures is close to the critical pressure and surface tension diminishes, a clear separation between the two phases is controversial. In mass transfer models, the different regions share the same velocity, pressure and temperature; however, the mass transfer phenomena are time-dependent and not instantaneous, which was the case in HEM. In mass transfer models, the main drawback is that the transport equations for the volume (or mass) fraction of the vapor with source terms to model phase change which is incorporated in the NS system of equations are empirical, case and time dependent, and thus calibration is necessary. Mass transfer models are based on the kinetic theory of gases, [34,77]or they adopt condensation and vaporisation terms; cavitation is described with respect to the growth and collapse process of vapor bubbles such as the models in [33,77,78].

On one hand in HEM model the two-phase regime is in thermodynamic and mechanical equilibrium but is questionable if it is valid in metastable thermodynamic states. On the other hand in HEM model the two phases share the same velocity, pressure field and temperature (in case of thermal effects) [39] and is accurate enough for medium and large-scale simulations of cavitating flows. The model is based on an Equation of State (EoS) for the pure phases and no empirical parameters and calibration are needed. Despite the fact that the vapor-liquid interface is not explicitly defined this is not so important, since the bubble interface can be estimated by the density as a result such models are still widely used for industrial applications due to simplicity. HEM models have been used for several applications, either macroscopic or microscopic ones and they can be either barotropic (pressure depends only on the density) or they can include temperature effects. HEM Barotropic models have been employed in several studies such as [79–84]. On the other hand, HEM with temperature effects has been employed by Saurel et al. [85] and by Schmidt, Sezal, Adams et al. for hydrofoil [86] and bubble cluster simulations or for modelling the flow in injection nozzles [87,88]. Works with real fluid thermodynamics, the work of Dumbser [89] for cavitating flows around hydrofoils and to the work of N. Kyriazis for single bubble collapse [90]. Furthermore, a pioneering investigation of cavitation dynamics and erosion in microchannels was [91], examining different geometries of square orifices, resembling the injection orifice of an actual injector. In the above works, density-based solvers were utilized in order to model the hyperbolic nature of the equations and to capture expansion, rarefaction and strong shock waves which were formed.

HEM models have been also used for Diesel injector simulations [87], microchannels [82]and for estimating erosion [92] and detection of the shock formation and propagation in three-dimensional cloud cavitation on hydrofoils [86]. For the sake of completeness, it is also worth mentioning a number of recent works employing HEM models, focusing on cavitation and sprays at transcritical and supercritical conditions of ECN Spray-A, using LES and real fluid thermodynamics (Peng-Robinson Equation of State) [93] . The same methodology has also been used to detect cavitation in internal injector flows [94]. However, these investigations did not involve any attempt to describe erosion. If the average flow temperature variation of the liquid can be negligible in some cases, the energy equation can be omitted and thus, barotropic cavitation models have been successfully employed for the prediction of cavitation either on macroscopic or on microscopic applications [95–97]. A compressible approach for simulating larger scale simulations of industrial interest, such as Diesel injectors and predicted cavitation with a more detailed insight has performed by Sezal et al. [88] and the collapse pressure peaks indicators that were noticed, could be used as of potential erosion locations [88,98]. Salvador et al. [99] have been worked in different aspects of Diesel injectors, starting from validation cases and expanded into the effect of geometrical features on the hydraulic performance of the injectors [100]) and LES simulations in OpenFOAM® [101].

Another group of investigations employs the Homogeneous Relaxation Model (HRM), as a mass transfer model, to capture phase change effects. The idea behind the model is to relax the metastable liquid state to reach an equilibrium as liquid/vapor mixture in a finite and often user-calibrated, time-scale. Applications involve flashing where the model was initially conceived, but over time, was adapted for cavitation as well [102]. Further works in the field of fuel injection involve [103] , where the authors analyse transient phenomena of needle opening or needle closing with Large Eddy Simulation (LES), as well as the resulting atomisation patterns, in single hole or multi-hole diesel injectors of the Engine Combustion Network (ECN) database. Since then, the HRM model has been used for a variety of applications, including marine injectors for industrial RANS simulations [104] and attempts to devise an erosion metric criterion have also recently performed [105] , whereas it has proven to have decent agreement against X-ray densitometry of the spray [106].

For the sake of completeness, it is also worth mentioning a number of recent works employing HEM models, focusing on cavitation and sprays at transcritical and supercritical conditions of ECN Spray-A, using LES and real fluid thermodynamics (Peng-Robinson Equation of State), [107]. The same methodology has also been used to detect cavitation in internal injector flows [108]. However, these investigations did not involve any attempt to describe erosion.

The study of [109] confirms the importance of considering local pressure in the improved form of the Rayleigh–Plesset (R-P) equation and illustrates the influence of the liquid compressibility for cavity modelling and appropriate capturing of the collapse pressure. In [110] a fully compressible four-equation model for multicomponent two-phase flow solver, coupled with a real-fluid phase equilibrium model employing the Peng-Robinson (PR) EoS for each phase, is used to demonstrate its capability in predicting phase change effects in simplified shock tube cases and orifices. In [111] the flow inside the same heavy-duty Diesel injector as the one studied in the present work has been performed. In this past work of the authors, the needle valve motion, compressibility and turbulence effects have been considered utilising a pressure-based solver. The recorded pressure peaks obtained have been correlated with the erosion development as identified from X-ray scans of used injectors. Validation of the numerical method and cavitation model was performed in, where X-ray CT scans confirmed the predictions of 3D volumetric cavitation distribution and erosion locations. LES with the employed cavitation erosion model was found able to predict the relevant flow and cavitation aggressiveness features with satisfactory accuracy.

Concerning works with needle movement, Koukouvinis et al. have implemented a layering algorithm, adding/removing a layer of cells as the needle moves in FLUENT Ansys [111]. The transient effects due to the needle movement have been also taken into account by Devassy et al. in AVL FIRE software [112,113] and Batistoni and Grimaldi [114]. In [115] the moving needle effects of a Diesel injector on the development of the cavitating flow and spray flow characteristics parameters were investigated by He et al. and in [116] Margot et al. simulated a diesel injector needle movement using commercial software STAR-CD. Significant contribution in the field of mesh motion in pistons and GDI injectors has been also made by Montorfano, Piscaglia et al. [117–120];they implemented a parallel algorithm for layer addition-removal in OF and performed LES studies. Wu et al. [121] expanded the idea of Dynamic Length-Scale Resolution Model (DLRM), which includes an adaptive rescaling procedure for both turbulent length and time scales, for a simplified square-piston engine. One of the state of the art studies for moving-needle Diesel injectors is, [122]. In [123] Stavropoulos developed IBM in OpenFOAM® coupled with multiphase compressible solver suitable for cavitation. Örley et al. [122] employed the conservative cut-element-based IBM for modelling the needle motion and took into account the vapor and gas phases as well incorporated LES turbulence model. They employed a barotropic two-phase two-fluid model, where all phases are represented by a HEM approach and the cavitation model is based on a thermodynamic equilibrium assumption.

Overset method has used for challenging problems like a bullet fling through the muzzle flow field [124]. Khaware et al. has validated the accuracy of the overset method for cavitating flow problems using a multi-phase RANS flow solver and a homogeneous mixture model in [125]. Koci et al. [126] has used the dynamic Cartesian cut-cell mesh moving method in CONVERGE® v2.3 CFD package for the numerically solve the governing equations of fuel injector nozzle flow on a discretized computational domain by the finite volume methodology with the VoF method was used to simulate multiphase flow. Arbitrary Lagrangian Eulerian (ALE) framework with geometric conservation laws have been used by Guventurk et al. [127] for simulating a single rising bubble in a Newtonian fluid.

On the one hand the mentioned methods for the moving computational domain are characterized by some numerical demands especially for simulating the thermal effects for a multiphase compressible flow under 450MPa injection pressure. For example (1) Higher Reynolds numbers requires high grid resolution and higher order scheme will lead to numerical oscillations, (2) Is significant to accurately resolve the boundary layers on surfaces not aligned with the grid lines without unphysical oscillations in the region of sharp corners when dealing with compressible fluids, (3) Need to accurately resolve the boundary layers on surfaces not aligned with the grid lines and sharp boundary edges requires high grid resolution and (4) additional computational load due to the interpolation process.

On the other hand, ALE method has some disadvantages like; (1) more complex grid generation and more difficult set up to move the computational grid; (2) during calculation it is necessary to compute the geometrical information for the computational grid and large deformations may lead to skewed cells. However, for this challenging and demanding study the advantages of ALE method make it appropriate. Most crucial and significant for the accurate prediction of the viscous heating is that the computational grid is aligned with the boundary layer. Also, is suitable for high Re number and because all the cells are within the flow field and accurately resolve the boundary layer on the wall using stretched boundary elements parallel to the flow achieving y+ with a minimal number of cells. The mass conservation is determining for a density based explicit solver like this is used in this study.

In this research, a Diesel injector simulation has been performed in OpenFOAM® by utilising a density-based solver with a modified Mach number consistent numerical flux appropriate for capturing the turbulence and the high collapse pressure. A two-step barotropic EoS, the Tait equation for the liquid and an isentropic resembling relation for the liquid-vapor mixture has been initially used. A second closure based on tabulated data has been used for a 4-component Diesel fuel surrogate, derived from the Perturbed-Chain, Statistical Associating Fluid Theory (PC-SAFT) Equation of State (EoS), allowing for thermal effects to be quantified. Simulation of a needle-moving Diesel injector with real fluid thermodynamics at high operating pressures up to 450 MPa is now feasible. For the multiphase solver developed in OpenFOAM®, the HEM approach is extended by Arbitrary Lagrangian–Eulerian (ALE) formulation is used for modelling the injector's needle valve movement.

Reference	Pressure/density-based	Cavitation model	Needle motion	Properties	Temperature effects	Turbulence model	Erosion
88	Density	HEM	Fixed	Barotropic	No	Inviscid	No
91	Density	HEM	Fixed	Barotropic	No	Inviscid	Yes
94	Density	HEM	Fixed	Real-fluid	No	Inviscid	No
102,104	Pressure	HRM/ mass transfer	Fixed	Real-fluid	No	RANS k-ε	No
168,268	Pressure, two-fluid	Eulerian, R-P	Fixed	Fixed	No	LES Multi–fluid	Yes
82	Density	HEM	Fixed	Barotropic	No	LES ALDM	Yes
105	Pressure	HRM/ mass transfer	Fixed	Barotropic	No	LES Dynamic 1-eq	Yes
103	Pressure	HRM/ mass transfer	Cut-Cell	Real-fluid	No	LES Dynamic 1-eq	No
162, 111	Pressure	Mass transfer	Fixed & ALE	Barotropic	No	LES WALE	Yes
112	Pressure, two-fluid	Mass transfer	ALE	Fixed	No	RANS k-ε	Yes
155	Pressure	Mass transfer	ALE	Barotropic	No	LES WALE	No
122	Density	HEM	IB/Cut cell	Barotropic	No	LES Implicit	Yes
110	Density	HEM	Fixed	Real-fluid	Yes	Inviscid	No
10,169, 170,172	Pressure	Lagrangian R-P	Fixed	Real-fluid	Yes	RANS k-ε	No
171	Pressure	Mass transfer	Fixed	Real-fluid	Yes	RANS k-ω SST	No
107, 108	Density	HEM	Fixed	Real-fluid	Yes	RANS k-ε, LES	No
220	Density	HEM	Fixed	Real-fluid (PC-SAFT)	Yes	LES WALE	No
93	Density	HEM	Fixed	Real-fluid	Yes	LES Smagorinsky	No
178	Pressure	HEM	Fixed	Real-fluid (PC-SAFT)	Yes	LES WALE	No
113	Pressure	Mass transfer	ALE	Fixed	Yes	RANS k-ε / k-ζ-f	Yes
172	Pressure	Lagrangian R-P	Fixed & ALE	Real-fluid	Yes	RANS k-ε	No
106	Pressure	HRM/ mass transfer	Cut-Cell	Real-fluid	Yes	RANS k-ε	No
Current work	Density	HEM	ALE	Real-fluid (PC-SAFT)	Yes	LES WALE	Yes

Table 1.1: Summary of models utilised for resolving the flow in diesel injector nozzles.

In addition to the numerical advancements, the literature review (see Table 1.1) and to the best of the author's knowledge, there is no relevant simulations reported for cavitation and induced erosion in fuel injectors, while considering variable fuel properties due to temperature/pressure gradients and incorporating transient effects caused by the motion of the needle valve. The developed numerical methodology addresses these phenomena for the first time.

1.3 Objectives

The aspiration of the current work is to develop a numerical tool in OpenFOAM® so as to predict cavitation in industrial compressible multiphase flow applications incorporating moving geometries such as those for high-pressure Diesel injectors. The most significant objectives summarised below:

- To develop an accurate in space and time FV method for moving computational domains for cavitating flows in OpenFOAM®.
- To modify a Mach number consistent numerical flux to handle the transition from incompressible to highly compressible flows in turbulence regions.

- To develop a numerical model for the tested fuel physical properties up to 4,500bar, LES resolving simultaneously the in-nozzle flow. Simulations utilising the real-world fuels and realistic/research injection cycle conditions.

- To develop/extent numerical methodologies required for the simulation of cavitating compressible flows and surface erosion indication at macroscopic (engineering) level. Relevant methodologies to be developed include (a) an LES model using a barotropic model, (b) an LES using a thermodynamic table.

- To apply the validated models to cases of industrial interest aiming to implement them as design tools to industrial practice.

- To perform verification and validation of the numerical algorithm against experimental results for several cases (injector nozzles)

2 Outline

In Chapter 3 the numerical model is described, including the governing equations for an ALE framework, the barotropic and the tabulated data approach and their derived thermodynamic closure, as well as the space and time discretization, the modified numerical flux as they have been implemented in OpenFOAM®. Model predictions are compared against corresponding X-ray surface erosion images obtained from injector durability tests for industrial applications, showing good agreement. In Chapter 4 investigation of the fuel heating for industrial applications, vapor formation and cavitation erosion location patterns occurring during the early opening period of the needle inside a five-hole common rail Diesel fuel injector discharging at pressures up to 450MPa are presented. Friction-induced heating has been found to increase significantly with increasing pressure drop. The extreme injection pressures induce fuel's jet velocity magnitude of the order of 1100 m/s, which in turn, affects the formation of coherent vortical flow structures into the nozzle's sac volume. It is found, in particular, that the fuel jet velocity variations with increasing discharge pressure, affect the locations of cavitation formation and collapse, which in turn, lead to different potential locations of erosion of the surface of the needle valve. In Chapter 5 investigation of the in-nozzle flow and cavitation forming in heavy-duty Diesel injector at injection pressures up to 450MPa at 350 μm fixed needle lift, using a realistic multicomponent Diesel surrogate. Two different methodologies have been utilised: one neglecting the thermal effects and one where the energy equation is solved considering thermal effects due to wall-induced friction and fuel depressurisation. In Chapter 6 a two-phase cavitation barotropic model for Diesel Fuel B0 2015 has been used for the analysis of the turbulent flow field during the opening phase of the injection. This work revealed the formation of thin and thick string cavitation in the orifice volume and the effects on the flow pattern in the orifice and at the exit of the orifice. String cavitation in the orifice is observed and coherent cavitation structures both in the axial line as string cavitation and on the orifice surface as shear-induced cavitation. Violent collapse events of cavitation structures are detected during the opening phase. Moreover, this work revealed the formation of thin and thick string cavitation in the orifice volume and the effects on the flow patter n in the orifice and at the exit of the orifice. Finally, In Chapter 7 the most important conclusions are drawn and future work is proposed.

3 Simulation of transient effects in a fuel injector nozzle using real-fluid thermodynamic closure

Abstract

Numerical predictions of the fuel heating and cavitation erosion location indicators occurring during the opening and closing periods of the needle valve inside a five-hole common rail Diesel fuel injector are presented. These have been obtained using an explicit density-based solver of the compressible Navier-Stokes (NS) and energy conservation equations; the flow solver is combined with two thermodynamic closure models for the liquid, vapor and vapor liquid equilibrium (VLE) property variation as function of pressure and temperature. The first is based on tabulated data for a 4-component Diesel fuel surrogate, derived from the Perturbed-Chain, Statistical Associating Fluid Theory (PC-SAFT) Equation of State (EoS), allowing for thermal effects to be quantified. The second thermodynamic closure is based on the widely used barotropic Equation of State (EoS) approximation between density and pressure and neglects viscous heating. This is a theoretically derived model, based on the perturbation theory, that requires only three molecular-based parameters per component for fluid property calculations. There are several advantages using the PC-SAFT compared to a cubic equation of state for calculating fluid properties such as the speed of sound. - The Wall Adapting Local Eddy viscosity (WALE) LES model was used to resolve sub-grid scale turbulence while a cell-based mesh deformation Arbitrary Lagrangian–Eulerian (ALE) formulation is used for modelling the injector's needle valve movement. Model predictions are found in close agreement against 0-D estimates of the temporal variation of the fuel temperature difference between the feed and hole exit during the injection period. Two mechanisms affecting the temperature distribution within the fuel injector have been revealed and quantified. The first is ought to wall friction-induced heating, which may result to local liquid temperature increase up to fuel's boiling point while superheated vapor is formed. At the same time, liquid expansion due to the depressurisation of the injected fuel results to liquid cooling relative to the fuel's feed temperature; this is occurring at the central part of the injection orifice. The formed spatial and temporal temperature and pressure gradients induce significant variations in the fuel density and viscosity, which in turn, affect the formed coherent vortical flow structures. It is found, in particular, that these affect the locations of cavitation formation and

collapse, that may lead to erosion of the surfaces of the needle valve, sac volume and injection holes. Model predictions are compared against corresponding X-ray surface erosion images obtained from injector durability tests, showing good agreement.

3.1 Introduction

Global actions for mitigating the impact of transportation on climate change have pushed governments and professional bodies to target an up to 20% reduction in CO_2 emissions and further limitation of particulate matter mass and NOx from heavy-duty Diesel, marine and aviation engines [128]; such combustion systems are responsible for about 2/3^{rds} of total liquid fossil fuels utilisation in transportation. To achieve today's and future emission standards, injection pressures beyond 200 MPa and multiple injections are required, resulting into liquid jet velocities of the order of 700 m/s [129], as they improve mixing and combustion [130]. At such conditions, the Reynolds and liquid-phase Mach numbers in the nozzle orifices are of the order of 30,000 and around 0.7, respectively; thus, flow is turbulent and compressible, while depending on nozzle hole geometry and needle valve motion, phase-change (cavitation) is typically occurring. On one hand, cavitation collapse could remove surface deposits [131], [132–134] and enhances primary jet break up [135–138] during nominal operating conditions; on the other hand, cavitation collapse could cause material erosion [139], [140], and as a result, affects the durability of various components of the fuel injection equipment; see selectively [141–144]. The violent change in the cavitation cloud volume during collapse causes pressures and temperatures that may even exceed 1 GPa and thousand degrees Kelvin, respectively [90]. Experiments on cavitation in Diesel injection systems have been reported as early as in the '50s [145]; different nozzle geometries have been utilised to reveal its effect on the structure of the injected liquid jets qualitatively [146]. Advanced experimental techniques, such as laser-pulsed light transmission measurements give information about the fluid density and pressure measurements under overall stationary, highly turbulent and cavitating flow conditions [147]. Shadowgraph schlieren imaging [148] applied to cavitating flows in generic geometries can reveal information for the flow, with pressure waves generated during bubble collapses. Moreover, the understanding and identification of the interaction between turbulence and vortex [149] or string cavitation [150] and their influence on jet and spray characteristics is necessary in order to understand the subsequent air-fuel mixing.

Detailed numerical studies of multi-phase flows in various fuel injectors have been presented since the ‘90s by solving the incompressible unsteady Reynolds-averaged Navier–Stokes equations (URANS), see for example [151], [150], [12]. The strong correlation between internal nozzle flow, string cavitation and primary spray atomization was shown in [152] while the recent works of the author’s have shown the influence of needle valve movement during the opening, closing and dwelt time of the needle valve [153] and [154–156]. Further studies analysed cavitating flows using high-speed digital imaging to capture the instantaneous spatial and temporal characteristics of geometric as well as string cavitation structures [157], [158]; more recent studies employing X-rays [159], [11] have provided quantitative data for the cavitation volume fraction, which allows thorough validation of the relevant models. Along the lines of these recent developments, the prediction of cavitation erosion has been also the subject of extensive research. In [160] a methodology employing flow solvers of the RANS equations has been proposed for cavitating flows; this was found capable of predicting the flow regions of bubble collapse and the potential aggressiveness to material damage. In [161] cavitation was modelled with the use of a barotropic Homogenous Equilibrium Model (HEM) making it suitable for erosion prediction inside a high-pressure fuel pump. The μm-scale of injectors makes experimental flow characterization challenging. Experiments of erosion damage can provide data about the locations of high structural stresses, which could be linked to cavitation; but they do not produce insight to all features of the underlying flow and thermodynamic conditions needed for the optimization of the performance of the injector. In [162] and [163] the impact of the large vortical structures within the nozzle flow and the interaction with incipient and developed cavitation in multi-phase flows was assessed, highlighting the necessity of employing LES to resolve such flows; this was combined with both a barotropic and a mixture model for simulating cavitation. Multi–phase CFD simulations considering flow compressibility can capture the pressure waves generated by collapsing vapor clouds and their impact on nearby surfaces. In [164] a density-based solver of the 3D inviscid Navier–Stokes equations was used. In [165] the turbulence structure was analysed with emphasis put on the interaction between cavitation and coherent flow motion. The numerical work of [122] on Diesel injectors involves the immersed boundary method for resolving the needle motion, compressibility of liquid, vapor and non-condensable gases. The authors have achieved an impressive simulation of a complete 9-hole Diesel injector, including injection in air, aiming to study the influence of cavitation and the transient effects of the needle on the emerging jets. In [111] the flow inside the same heavy-duty Diesel injector as the one studied in the present work has been performed. In this past work of the authors, the needle valve motion, compressibility and turbulence effects have been considered utilising a pressure-based solver. The recorded pressure peaks obtained have been correlated with the erosion development as identified from X-ray scans of used injectors. Validation of the numerical method was performed using the erosion model proposed in [95]; this is based on the physical description of phenomena from cavitation cloud implosion and pressure waves and pit formation depth. The coupling between CFD and the erosion model was based on the use of the mechanical properties of hardened AISI 52100 steel [166]. LES with the employed cavitation erosion model was found able to predict the relevant flow and cavitation aggressiveness features with satisfactory accuracy. More recent works [167], [168] have employed a two-fluid model on the simulation of cavitation, erosion and effects of sprays; the overall performance of such models relative to mixture models was assessed.

Despite their complexity, all aforementioned cavitation models have ignored viscous heating effects. However, the flow during the discharge of the fuel is characterized by strong velocity gradients, which induce wall friction and consequently, can result to significant fuel heating. Only limited number of works address fuel heating/cooling and phase-change in high pressure Diesel injectors. The first studies [169], [170], [10], [171] from the authors have utilised URANS and have been performed under fixed needle valve conditions; they revealed two opposing processes strongly affecting the fuel injection quantity and temperature; the first one, known as Joule-Thomson effect, is related to the depressurisation of the injected liquid, which results to fuel temperatures even lower than that of the feed. On the other hand, the strong heating produced by wall friction increased significantly the fuel temperature above the boiling point in the near wall regions where viscous effects are dominant. In follow up works, [172], [4] the transient effects owning to the needle motion have shown significant variations in temperature during its opening/closing phase, suggesting that simulations performed at fixed needle lift cannot represent the actual phenomenon. Still, these works have utilised fuel properties from [173] and have not considered the link between cavitation and induced erosion. Recently, new experiments on the properties of diesel fuel at elevated pressures and temperatures have been reported; this has allowed for development and calibration of the PC-SAFT EoS, as reported by the authors in [174–181]; tabulated data have been derived for various fuel surrogates coving the range of properties variation occurring within high pressure fuel injectors and thus allowing for accurate estimation of the effects of fuel property variation to be considered. Still, such effects have not been studied in relation to transient effects caused by the motion of the needle valve.

From the above review, and to the best of the author's knowledge, it seems that there no relevant simulations reported for cavitation and induced erosion, while considering variable fuel properties due to temperature/pressure gradients and incorporating transient effects caused by the motion of the needle valve. The aim of the current work is to address these phenomena and simulate the flow inside a high-pressure Diesel injector considering these complications. For this purpose, the explicit density-based solver flow solver reported in [90] has been implemented in OpenFOAM and has been coupled with tabulated fuel property data derived from the PC-SAFT EoS, as documented in [174–180] and [182]. The injector needle valve movement is represented by the ALE approach, as proposed in [183], guaranteeing enforcement of the Space Conservation Law (SCL). One of the important features of the developed model is the combination of the Wall Adaptive Eddy (WALE) [184] LES model. Model predictions are also compared to those obtained using the isothermal barotropic model while results from both simulation approaches are compared against the experimental data reported in [111] for a 5-hole diesel injector.

The paper is structured as follows: first, the mathematical and physical models are presented. Then, the discretization and the thermodynamic closures are analysed followed by the description of the Diesel injector geometry, computational setup and erosion patterns. Then the limitations of the numerical model are discussed, followed by the analysis of the three-dimensional flow-field; this includes analysis of viscous fuel heating and cooling due to depressurisation. Next, the flow-field for the full injection cycle presented while in the final section, the results from the computational analysis are compared with the erosion pattern retrieved from experiments.

3.2 Mathematical and physical model

The explicit density-based flow solver is based on the works of [90], [111], [185] and [161] but extended here to include moving grids. The mathematical model employs a set of conservation equations governing the fluid motion, re-casted in a form of space conservation law suitable for moving/deforming meshes. The equations with a notation of [183] and written in weak (integral) form given below; bold denotes vector/tensor and italic scalar variables:

- Continuity equation:

$$\frac{\partial}{\partial t}\int_V \rho dV + \int_A (\rho \mathbf{u}_\mathrm{r}) \cdot \mathbf{n} dA = 0 \tag{3.1}$$

Here, ρ represents the fluid density, $\mathbf{u_r}$ is the relative velocity of the fluid in respect to the velocity of the moving grid, $\mathbf{u_g}$, defined as $\mathbf{u_r} = \mathbf{u} - \mathbf{u_g}$, $\mathbf{n}$ is the surface normal to the local grid face; V index implies volume integral and A surface integral.

- The momentum conservation equation:

$$\frac{\partial}{\partial t}\int_V \rho \mathbf{u} dV + \int_A (\rho \mathbf{u} \otimes \mathbf{u}_\mathrm{r}) \cdot \mathbf{n} dA = -\int_A p \mathbf{n} dA + \int_A \boldsymbol{\tau} \cdot \mathbf{n} dA \tag{3.2}$$

Here, p denotes the fluid pressure and $\boldsymbol{\tau}$ is the viscous stress tensor, defined as:

$$\boldsymbol{\tau} = \mu_{eff} [\nabla \mathbf{u} + (\nabla \mathbf{u})^T] - 2/3 \mu \nabla \cdot \mathbf{u} \tag{3.3}$$

where μ_{eff} is the effective viscosity of the fluid, including both turbulent (μ_t) and laminar (μ) viscosities.

- Energy conservation equation:

$$\frac{\partial}{\partial t}\int_V \rho E dV + \int_A (\mathbf{u}_\mathrm{r} \rho E) \cdot \mathbf{n} dA = -\int_A p \mathbf{u} \cdot \mathbf{n} dA + \int_A (k_{eff} \nabla T) \cdot \mathbf{n} dA + \int_A (\boldsymbol{\tau} \cdot \nabla \mathbf{u}) \cdot \mathbf{n} dA \tag{3.4}$$

where: E represents the total energy as the sum of internal energy, e, and kinetic energy $K = \frac{1}{2} u^2$, T is the temperature of the fluid and k_{eff} is the effective thermal conductivity of the fluid, including both turbulent (k_t) and laminar (k) thermal conductivity.

- The volume change of cells due to mesh motion can be expressed as:

$$\frac{\partial}{\partial t}\int_V dV + \int_A \mathbf{u}_\mathrm{r} \cdot \mathbf{n} dA = 0 \tag{3.5}$$

For the system closure, expressions for pressure, p, and temperature, T, are necessary to complete equations (3.2) and (3.4). These are obtained from the thermodynamic closure, or Equation of State (EoS) employed, which enables to define relations of $T=f(\rho, e)$ and $p=f(\rho, e)$.

3.3 Numerical schemes

The speed of sound in a cavitating flow may vary from O(3) to effectively near zero in the mixture region. Hence, in some parts of the domain the flow can be considered incompressible, whereas in others it is highly compressible. This renders calculations problematic with density based solvers, as they tend to be diffusive in the near incompressible regime, converging to incorrect states [41]. In this work, a hybrid numerical scheme is used, implemented as discussed in [90]; this scheme involves blending of the Mach number (M) consistent numerical flux of [186], with a compressible variant based on the Primitive Variable Riemann Solver (PVRS - see [187]). The blending is done based on the local Mach number to enhance solver stability; when the Mach number is small, the scheme reverts to the Mach-consistent numerical flux, whereas when the Mach number is large, it switches to the PVRS-variant. Time advancement is performed using a four stage Runge-Kutta method. The allowable step size is usually determined based on the following three factors: absolute (linear) stability, robustness (nonlinear stability) and accuracy as described also in [187]. Moreover during this work it was observed that using a high weighted term β Eq(25) [185], for example the blending coefficient α =10, or higher, for both thermodynamic models, the compressible-incompressible contribution at the hybrid flux of the interface pressure Eq(22) [185] influences vortex origin, size, development and reduces or even eliminates vortex cavitation. Also, it was evident that vortices could dissipate in the centre of the nozzle's sac volume, leading to significantly lower amount of overall vapor in comparison with the case where α =1 was used. The further reduction of the α coefficient does affect the amount of vapor in the injector volume or vortex behaviour attached on solid boundaries or forming closed loops, as expected from the Helmholtz second theorem. The reason is that the high α coefficient influences the momentum numerical flux by rendering the numerical solution much more diffusive. Using an α coefficient very close to zero (e.g. 0.01), the expected vortex behaviour is recovered, but solution stability is adversely affected. Hence a modification of the blending is proposed here in equation (3.6) below:

$$\alpha = \alpha_{min} + \left(M_f - M_{min}\right) * (\alpha_{max} - \alpha_{min}) / (M_{max} - M_{min}) \tag{3.6}$$

where M_f, M_{max} and M_{nin} denote the Mach number of the surface of the computational cell, and its upper and lower limits, respectively; if the Mach number is higher than the corresponding upper limit value, the α coefficient is set equal to this value. In this way, the amount of vapor in the injector volume or the origin and size of vortices is not influenced, while also renders the solver stable especially during the early opening and closing phases. The modified numerical flux based on Eq(25) [185] is shown in Figure 3.1. As shown, a range of α coefficients from 0.01 (for low Mach number regions) to 5 (for high Mach number regions can be used.

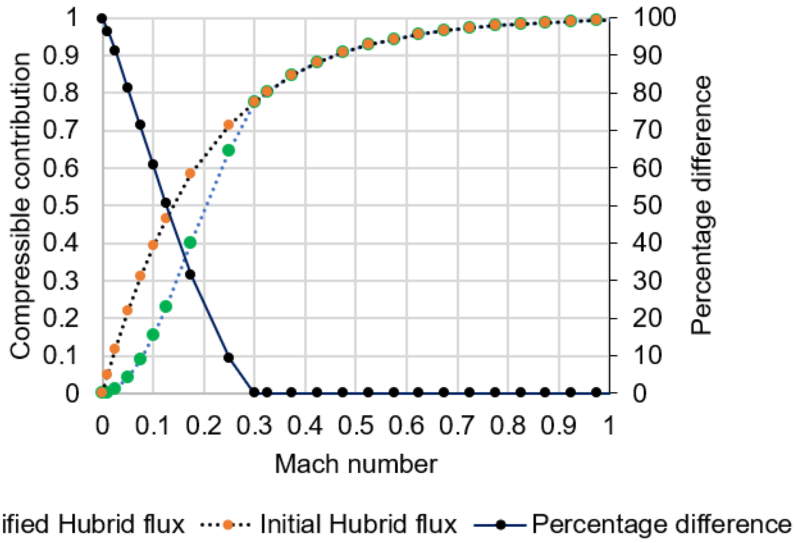

Figure 3. 2: Illustration of the contribution of the weighted term β (Eq(25) [185]) on the interface pressure as described in Eq(22).

3.4 Thermodynamic closure 1: Thermodynamic properties derived from the PC-SAFT EoS

To address the dependency of physical and transport properties on pressure and temperature, as well as the phase-change characteristics among different fuel components, a technique employing thermodynamic tables is adopted, as described by the authors in [90]; to give an example, the variation of fuel density, dynamic viscosity, heat capacity and conductivity with respect to P-T conditions in the fuel injector is up to 30%, 10^4 %, 40% and 60%, respectively. The advantage of using a table is that it offers flexibility, since a wide range of data can be easily exchanged, while achieving accuracy and low computational cost; this is particularly true when considering complex real-fluid EoS, such as the libraries of NIST [188] or the PC-

SAFT EoS [189]. The table is two dimensional, expressed in terms of the decimal logarithm of density and internal energy, over an interval of ρ:0.001 to 1100kg/m^3 and e: -1455kJ/kg to 5000kJ/kg, corresponding to min/max T of 275-2027K and p of 1Pa to 3420 MPa; this space is discretised with 500 points for both density and internal energy. Values are stored for all thermodynamic, physical and transport properties, such as pressure (p), temperature (T), enthalpy (h), entropy (s), heat capacity at constant pressure (cp), speed of sound (c), thermal conductivity (k), dynamic viscosity (μ) and vapor volume fraction (vf); intermediate values are found using bilinear interpolations.

In combination with this EoS, transport properties such as viscosity and thermal conductivity can be calculated using an entropy scale approach with a good degree of accuracy as reported in [190], [191], while surface tension is modeled using the density gradient theory [192]. Entropy scaling is an intriguingly simple approach for correlating and predicting transport properties of real substances and mixtures. Entropy scaling relies on a suitable definition of a dimensionless thermal conductivity, where the thermal conductivity is divided by a reference thermal conductivity. Indicatively, the three-dimensional phase diagram derived from the above PC-SAFT EoS for the 4-component surrogate Diesel fuel utilised here, is shown in Figure 3.2.

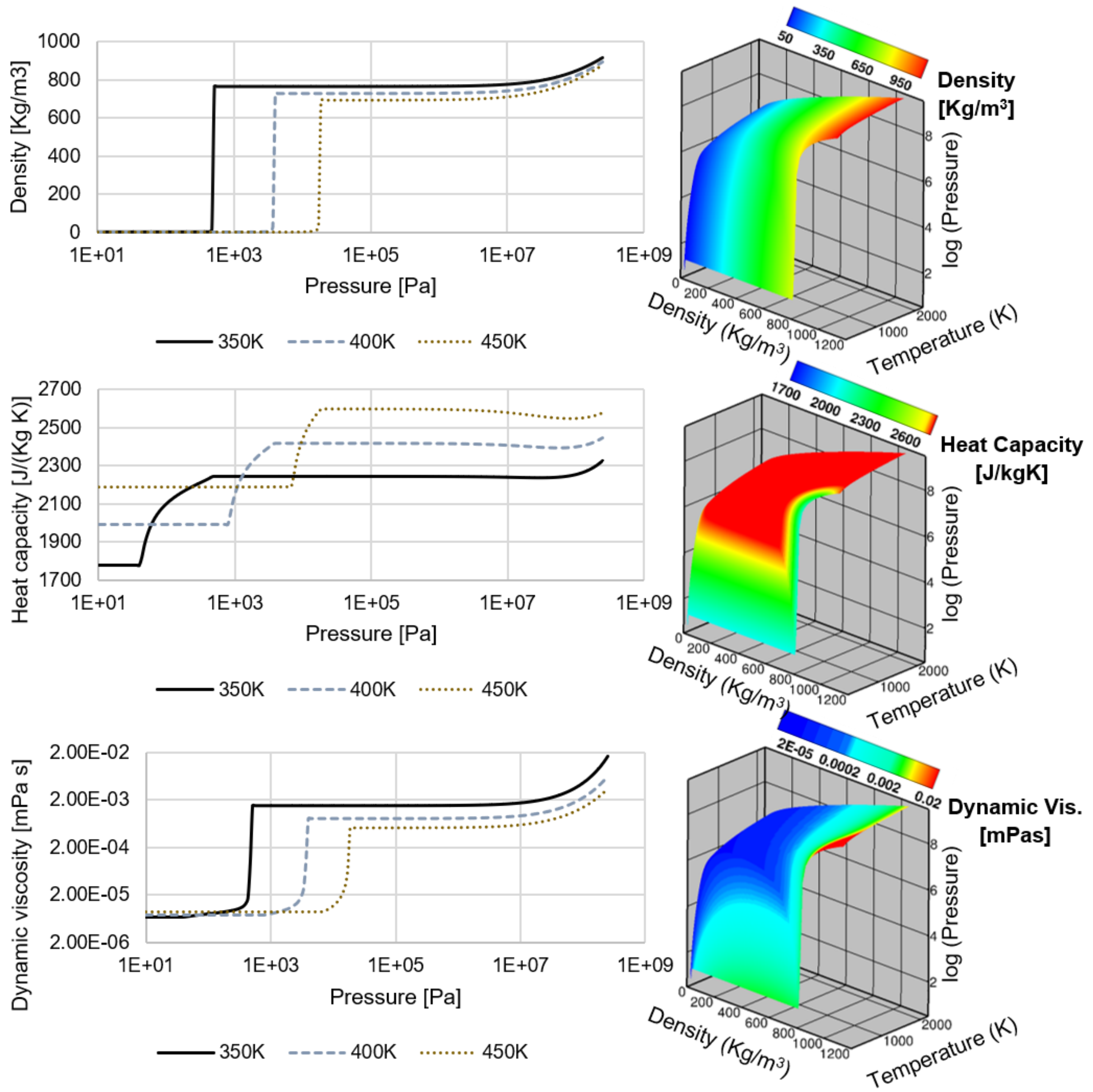

Figure 3. 3. Illustration of variation of density, heat capacity and dynamic viscosity of the 4-component Diesel fuel surrogate utilised; both two- and three- dimensional plots are shown.

3.5 Thermodynamic closure 2: Barotropic EoS

A two-step barotropic EoS has been used by the authors in [111]; the modified Tait EoS was employed for the liquid phase and the isentropic approximation proposed in [165] was used for the liquid-vapor mixture, as shown by equation (3.7). In this relationship, C1 is a coefficient that emulates isentropic vaporisation of the liquid; n=7.15 (see [193]) is a liquid-dependent constant while $\rho_{sat.\ L}$ is the saturation density of the liquid at saturation pressure p_{sat}. The properties of the liquid are considered at 396K [111], which is the average temperature between the estimated maximum and minimum temperatures within the computational domain.

$$p(\rho) = \begin{cases} (B + p_{sat})\left[\left(\frac{\rho}{\rho_{sat,L}}\right)^n\right] - B, & \rho \geq \rho_{sat,L} \\ p_{sat} + C_1\left[\frac{1}{\rho_{sat,L}} - \frac{1}{\rho}\right], & \rho < \rho_{sat,L} \end{cases} \quad (3.7)$$

$$B = \frac{\rho c^2}{n}, \qquad c = \sqrt{\left(\frac{\partial p}{\partial \rho}\right)_S}, \quad (3.8)$$

Moreover, in equation (3.7) the coefficient B indicates the liquid stiffness/elasticity. In Table 3.1 and 3.2, the numerical values for the reference state for computing the Tait parameters are provided. The saturation points properties for the liquid and the vapor phases are provided in Table 3.3 while Figure 3.3 illustrates the variation of density with pressure at the reference temperature of 396K.

Table 3. 1. Thermophysical properties at 180 MPa, 396K.

Property	unit	value
Inlet pressure	[10^6 Pa]	180
Density	[kg/m^3]	860
Speed of sound	[m/s]	1700

Table 3. 2. Thermophysical properties at 5 MPa, 396K.

Property	Unit	value
Outlet pressure	[10^6 Pa]	5
Density	[kg/m^3]	733
Speed of sound	[m/s]	1070

Property	unit	value
Saturation pressure	[Pa]	3600
Saturation density, L	[kg/m^3]	727
Speed of sound	[m/s]	950
Saturation density, V	[kg/m^3]	0.1

Viscosity, L	[Pa s]	0.000859
Viscosity, V	[Pa s]	7.49* 10^{-6}

Table 3. 3. Fluid parameters for 396K.

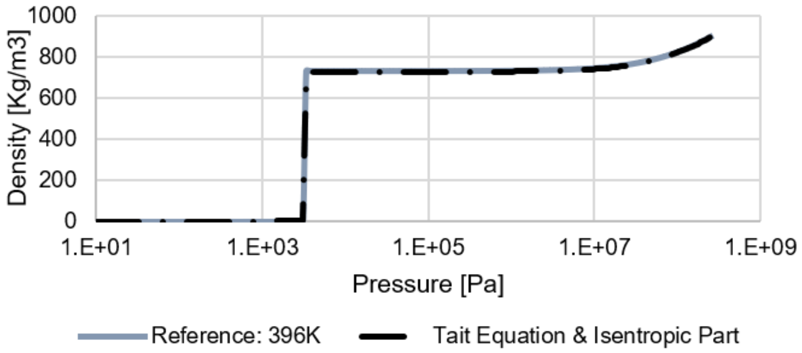

Figure 3. 4**.** Utilised density variation with pressure, as predicted by the relevant barotropic fluid EoS.

3.6 Description of the examined injector and testing conditions

The simulated geometry is presented in Figure 3.4, while specific dimensions of the injector featuring slightly tapered holes are given in Table 3.4. The injector consists of five orifices, but only the 1/5th of the full injector was simulated, employing symmetry boundary conditions. The computational mesh used consists of a hexahedral block-structured zone, while an unstructured tetrahedral zone is used in the sac volume upstream of the orifice entrance. Mesh motion is performed with a cell-based deformation algorithm, which moves the computational points and cells and stretches them uniformly. The needle lift was initially set at 0.6 μm with 5 cells placed in the needle seat flow passage. The initial flow field was obtained from a steady-state simulation performed at the minimum lift. The total cell count at the minimum lift is ~0.9 million and reaches a peak of 1.5 million at full needle lift. The computational mesh of the sac volume and injection hole, which do not change throughout the simulation, are shown in Figure 3.4b and Figure 3.4c, respectively. Also, Figure 3.4 shows the combustion chamber volume which is filled with liquid at initialization and pressure boundary condition at the outlet is set according to Table 3.6. Figure 3.5 shows the inlet pressure and needle valve lift, as predicted using the 1-D system performance analysis software, and used as boundary conditions in the CFD simulations. The needle motion is assumed to be in the axial – z direction only; no eccentricity effects are considered. In Table 3.5 and Table 3.6, the numerical values for the reference state for the inlet and outlet, respectively, are provided. The simulations were carried out using the WALE model [194]. Based on the cell sizes indicated in Table 3.7 and the flow conditions, it is possible to make an estimate of the Kolmogorov and Taylor scales of fluid motion for this case, also shown in Table 3.7. The Taylor length scale gives a characteristic size of inertial scales transitioned to viscous scales and can be used as a resolution target that is respected in the LES. The time step used is 0.5 ns, which corresponds to an acoustic Courant number (CFL) of 0.7; this is also smaller than the Kolmogorov time scale throughout the computational domain.

Table 3. 4. Geometric dimensions of the examined injector.

	unit	value
Max. Needle radius	mm	1.711
Orifice length	mm	1.262
Orifice diameter Inlet	mm	0.37
Orifice diameter Outlet	mm	0.359
Sac volume	mm^3	1.19
K-factor (Din-Dout)/10	-	1.1

Property	unit	value
Inlet pressure	[MPa]	180
Inlet Temperature (Thermodynamic closure 1)	[K]	350
Inlet Density (Thermodynamic closure 1)	[kg/m^3]	885.5
Inlet Temperature (Thermodynamic closure 2)	[K]	396
Inlet Density (Thermodynamic closure 2)	[kg/m^3]	863.5

Table 3. 5. Boundary conditions at the inlet.

Table 3. 6. Boundary conditions at the outlet.

Property	unit	value
Outlet pressure (Thermodynamic closure 1,2)	[MPa]	5

As shown in Table 3.7 the injector mesh topology has been divided in three topologies with different characteristics. The Reynolds number into the injector varies significantly between the needle seat, sac and orifice volume. Given the flow conditions inside the injector the Reynolds number is ~60000 for the needle and orifice region and ~45000 for the sac volume. The following values correspond to Taylor length scales, λ_g:

$$\lambda_g = \sqrt{10} Re^{-0.5} L \tag{3.9}$$

Table 3. 7**.** Taylor microscale of fluid motion for the injector's different part.

Region	**Taylor length scale**	**Smaller cell**	**Kolmogorov time scale**
Needle Seat	3 µm	1 µm	1.5 ns
Sac Volume	9 µm	7 µm	8 ns
Orifice	4.7 µm	3 µm	2.2 ns

Besides the mentioned criteria the turbulent kinetic energy should be resolved and wall function has been used to avoid very fine mesh towards the wall (y+ criteria). The near wall flow was treated with two wall functions: (i) kqRWallFunction for the turbulent kinetic energy and (ii) nutkwallfunction for the turbulent viscosity.

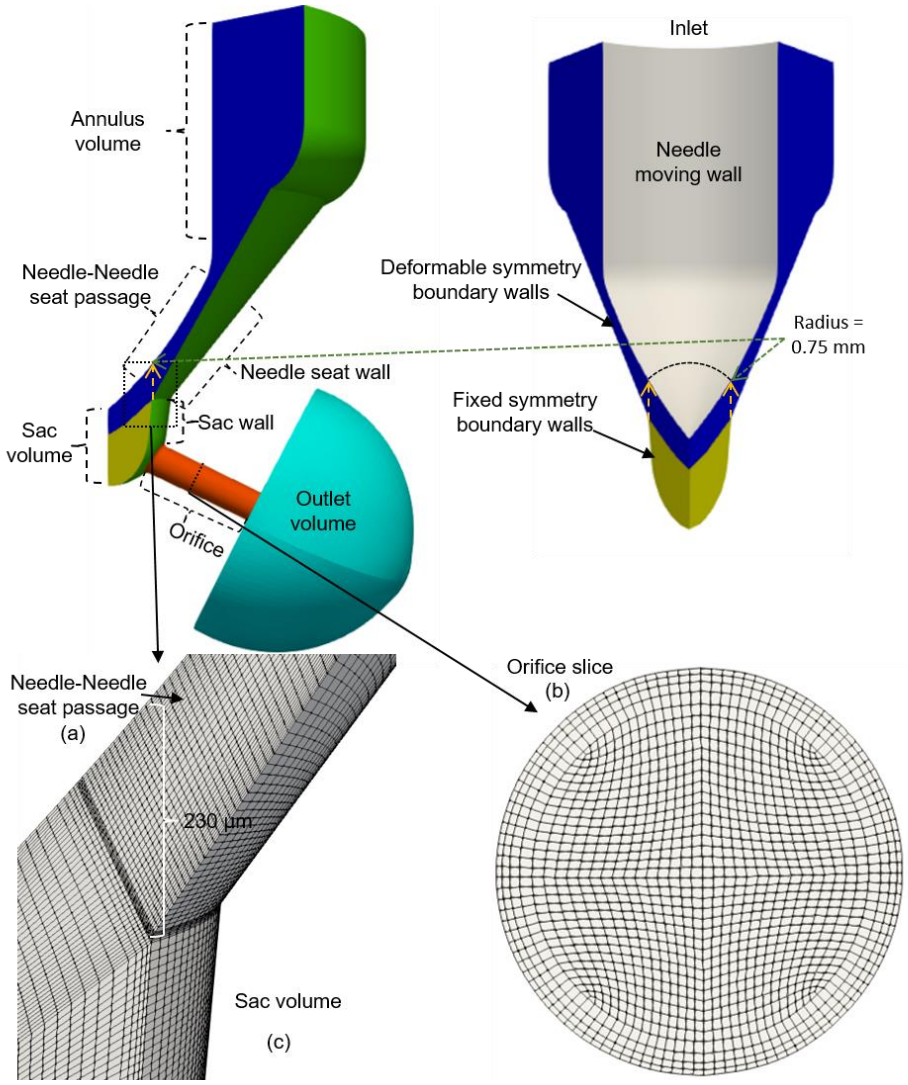

Figure 3. 5**.** Naming convention of injector surfaces (top) and 3D view of the computational domain at 70 µm needle lift (bottom).

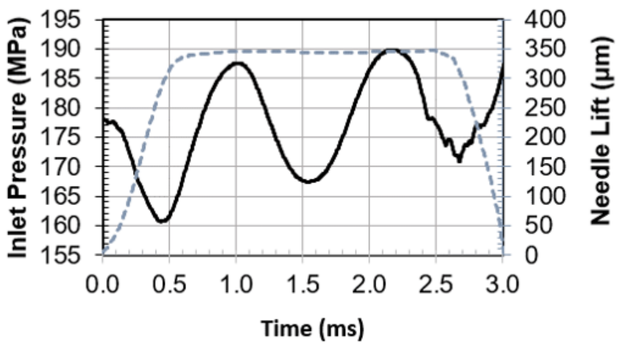

Figure 3. 6**.** Injection pressure and needle lift utilised as boundary conditions.

3.7 Injector endurance tests and X-ray erosion patterns testing conditions

Accelerated cavitation erosion durability tests have been performed in an endurance test rig, located at Caterpillar US research and development centre. Endurance testing is conducted for several thousand hours, with injection pressure at 1.1–1.5 times the injector rated operating pressure. The testing fuel is periodically replaced to maintain quality. The injectors are mounted on the head block of the test rig and the injected fuel is collected by the collector block and the rate tube; the downstream pressure adjusted by the pressure regulator at the end of the rate tube. The test rig has a heat exchanger to keep Diesel fuel temperature controlled at 40±1°C in the fuel tank and a computer which collects the data and controls the injection frequency. After the pressurization of the fuel at the nominal pressure of 180 MPa, the fuel reaches 350K, which is the feed temperature at the inlet of the injector. The erosion patterns from the endurance tests have been reported in [111] and they are consistent for all injectors tested at the same time intervals. The needle valve but not the needle seat is affected by erosion, since a deep erosion ring with mean radius of 0.75 mm is visible; for comparison, the larger radius of the nozzle's sac volume is 0.75 mm and the radius of the needle is 1.71mm, as shown in Figure 3.4. In the nozzle holes, the injector is generally less prone to erosion damage; surface pits have been observed only on the hole's top side. Finally, only minor signs of erosion damage inside the sac volume have been observed, that become apparent after thousands of hours of continuous operation.

3.8 Limitations and link to previous works

Limitations arising from both the validity of the models themselves utilised and the selection of the specific conditions investigated, include: (1) the dependency/accuracy of the simulations on the equations describing the fuel properties as function of pressure and temperature; (2) the assumption of local mechanical and thermal equilibrium, i.e. vapor and liquid have, locally, the same velocity (no slip) and same temperature, utilised in order to predict the amount of fuel that cavitates; (3) the assumption of adiabatic nozzle walls and (4) the lack of detailed validation against experimental data. A short evaluation of those factors is provided below, before the presentation of the results.

(1) The dependency/accuracy of the simulations on fuel properties as function of pressure

and temperature is considered by utilising the PC-SAFT EoS. This EoS [189,190] has been previously used with the Diesel surrogates [195] of this work and compared with experimental results up to 500MPa and 600K for density, viscosity and volatility, [181] with an accuracy of 1.7% for density, 2.9% in volatility and 8.3% in viscosity. Other Diesel properties, such as thermal conductivity, at extreme conditions up to 450MPa and 360K can also be found accurately predicted by PC-SAFT [176], [175], [181] with an accuracy of 3%. It can thus be claimed that the selected EoS is a good compromise for studying such effects in high pressure fuel injectors.

(2) One of the main assumptions in the described methodology is the mechanical and thermodynamic equilibrium between the liquid and the vapor phases. With regards to the mechanical equilibrium assumption, the recent study from the authors using a two-fluid model has confirmed that differences between liquid and vapor velocities are less than 10% and only in localised locations of the flow [168]; they have been found not to affect the overall growth rate and production of vapor. With regards to thermodynamic equilibrium, a metastable, i.e. non-thermodynamic equilibrium, state occurs when the pressure of the liquid drops below the saturation pressure and no vapor is formed, leading to liquid tension, due to the rapid expansion of the liquid [196,197]. The relaxation time of the tensile stresses, i.e. those acting in the metastable state, was numerically estimated to be of the order of 10ns for a vertical tube filled with liquid, impacted vertically and producing an expansion wave of 30MPa. The concentration used in this study was infinitesimally small, and would significantly overpredict this time scale in real systems; nevertheless, it is possible to use this time-scale to observe that, as the residence time of the fluid in the injection hole has a value of the order of ~1.5μs for the 180MPa case studied here, the time to reach thermodynamic equilibrium would be ~150 times faster.

(3) In the absence of information of either the internal (i.e. in contact with the fuel) or the external surface of the injector as well as its detailed geometry and assembly on the cylinder head, make any assumption for estimating the heat transfer between the metallic nozzle and the fuel practically impossible. Nevertheless, older studies [4] have estimated the heat transfer based on some gross approximations of those parameters; it clearly suggests that due to the very short time scale of the injection event relevant to the time it takes for wall heat

transfer to give an appreciable effect: less than 0.2% variation in the amount of cavitation forming and 0.07ΔT degrees in the mean fuel exit temperature, where stands for the temperature difference when adiabatic walls are considered. Thus, the adiabatic wall assumption is a good approximation for this specific case.

(4) Quantitative experimental data (i.e. vapor volume fraction and velocity flow field) are available only for enlarged nozzle replicas operating at significantly lower pressures. Such validation works have been thoroughly reported from the authors utilising similar models to those reported here. More specifically, the barotropic homogeneous mixture model has been have been validated against the 3D distribution of vapor fraction within the validation uncertainty (±7%, including both numerical and experimental uncertainties) [162], [97]. Further validation has been obtained for the flow field distribution, cavitation frequency shedding and turbulent velocities in the same single-hole injector against high energy X-ray phase contrast imaging (XPCI) measurements for conditions covering a range of cavitation regimes (incipient, fully developed and vortex/string cavitation) [159], [198]. Additionally, validation against Laser Doppler Velocimetry (LDV) measurements has been also reported [162]; this study has also utilised the WALE LES model for turbulence, as it has been proved that can reproduce accurately the turbulent structures found in Diesel nozzles. These studies suggest this model is capable of capturing both incipient and developed cavitation turbulent features. In the present study, the Reynolds number is ~[900-15000] and thus, it is within the range of applicability of the selected model. As the vaporous core of cavitating vortices has been found to be in the order of 20μm [199], the smallest cell size of ~2μm used is small enough to capture the smallest scales present in the flow that can potentially lead to vortex cavitation. Inspection of the calculated flow fields for the tested conditions here suggest that there are no under-resolved vortical structures that may cavitate and significantly influence the obtained results. Moreover, for injection pressures in the range of 180MPa, the same simulated injector geometry was previously validated for predicting cavitation erosion damage utilising the barotropic model. Turning to thermal effects, there are no experiments for the temperature variation that can be used for validation. Here results will be presented against 0-D predictions of the mean fuel heating up as it discharges through the fuel injector while predictions against the erosion data available are further utilised for the validation of the model.

3.9 Comparison against 0-D thermodynamic model predictions

Due to lack of experimental data, a 0-D thermodynamic model is used to estimate the fuel temperature variation between inlet and outlet using equation (3.10); adiabatic nozzle walls and no work exchange under fixed lift conditions have been assumed, while the generation of turbulence has been ignored. The comparison against the CFD predictions is shown in Figure 3.6 as a function of the nozzle discharge coefficient, which is also presented on the same plot; as mentioned earlier, this has been predicted by utilising the two thermodynamic closures. It is reminded that the nozzle discharge coefficient is defined as the ratio between the actual injected fuel mass over the ideal one that would have been obtained without any pressure losses. For fuel injectors, the discharge coefficient changes from zero when the needle valve is closed and takes its maximum value at full lift.

$$T_{out,0D} = T_{out}\frac{\left(h_{0,in} - h_{0,out}\right)}{h_{0,in}} + T_{out} \tag{3.10}$$

These estimations have been obtained assuming an initial fuel temperature of 350K. An increase in temperature is observed, particularly during the needle opening and closing periods, where an increase up to 100 degrees is estimated by both the CFD and the 0-D models. Overall, it can be seen that almost identical predictions from both models have been obtained for the mean temperature variation between the inlet and the outlet as function of the needle valve movement. Some differences observed during the very early stages of the needle valve are attributed to transient effects, which are not considered by the 0-D model. Peak values are mainly concentrated into the needle seat passage, starting from its narrowest gap and extending well inside the nozzle's sac volume. Liquid expansion compensates some of the expected fuel heating while cooling is predicted for Cd values higher than 0.8. After the first and second stage of the needle valve opening, the average fuel temperature is very close to the value estimated assuming isentropic expansion of the injected fluid, which justifies the use of the barotropic model at sufficiently high needle lifts. Finally, the average fuel temperature seems to be noticeably higher during opening (up to ~470K) when compared to closing (up to ~440K).

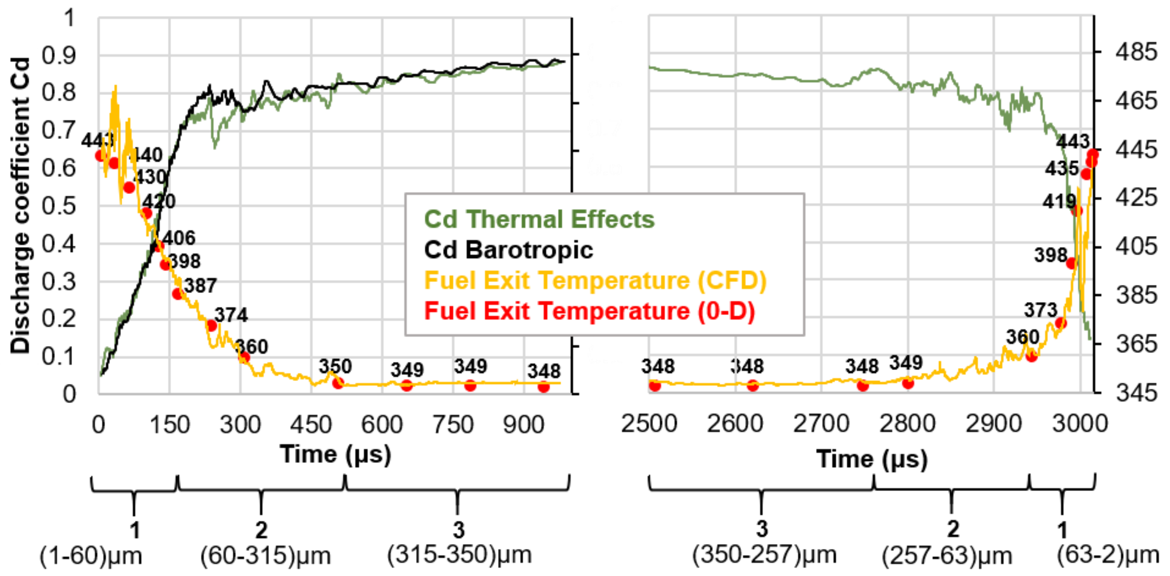

Figure 3. 7**.** Nozzle discharge coefficient and fuel exit temperature during the opening (left) and closing (right) phase during injection. The Cd coefficient has been calculated based on the theoretical mass flow rate and on the calculated mass flow rate from CFD results, at 1 μm before orifice exit.

3.10 Cavitation development during the opening and closing phases

The opening period of the injection event can be divided into three stages. During the first stage, cavitation appears at the needle seat passage, inside the sac volume and in the orifice. During the second stage, a transition of the cavitation from the lower to upper orifice surface is predicted. Unstable vortex string formations initiate from the needle tip, travel into the orifice inlet and cavitation occurs only in the orifice; sheet cavitation formation is observed at the upper orifice surface and large stable vortical and vapor structures, aligned with the flow direction, dominate. During the third stage, the flow is attached at the vertical wall of sac volume while fully developed cavitation formation is observed at the upper orifice surface. The first stage lasts between 0-150 μs (60 μm), followed by the second stage realized during 150-500 μs (315 μm); and finally, the third stage lasts between 500-985 μs (350 μm). During stage 1, the Cd values are lower than 0.4. During this stage, both thermodynamic closure 1 and 2, as mentioned above, predict similar trends for the Cd, vapor volume fraction and turbulence formation. Figure 3.7 shows the maximum velocity and the vapor volume formed in the needle seat passage during this time period; a clear vapor formation and shedding pattern can be observed. Vapor formation blocks the liquid fuel through the needle seat passage which results to a decrease in the velocity.

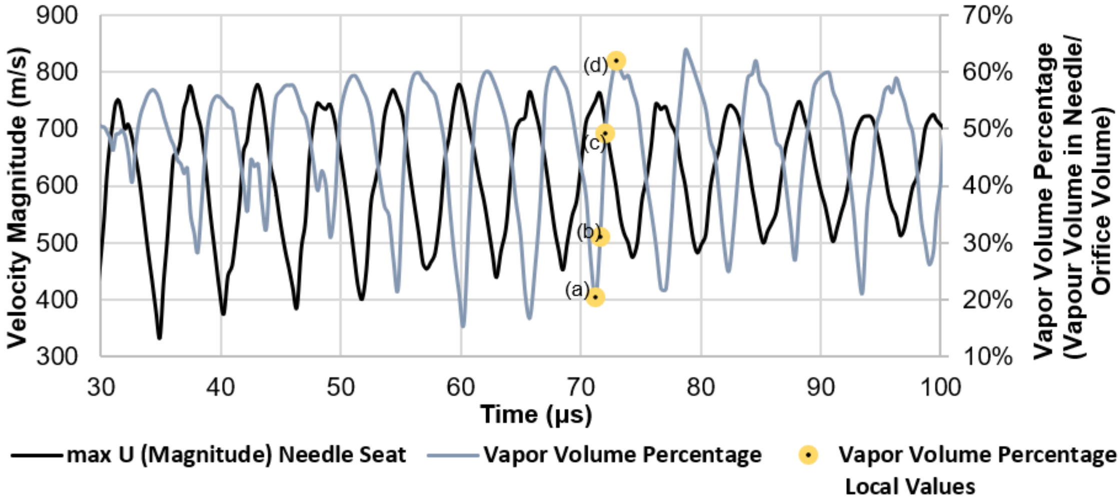

Figure 3. 8. Temporal evolution of maximum velocity magnitude and vapor volume percentage at the narrowest point at the needle seat passage; lift increase from 12 μm to 35 μm during the plotted time. The points (a) to (d) are indicated as a reference to following figures.

One representative vapor shedding cycle during the opening phase of the needle valve is shown in Figure 3.8. The cavitation formation and development at the needle seat passage is closely related to the unsteady recirculation zone and the vortex-cavitation shedding in the sac volume intake or close to vertical sac wall, indicated as VCS_1. Cavitation appears at the needle seat, inside the sac volume and in the orifice, as shown in Figure 3.8(a-c).

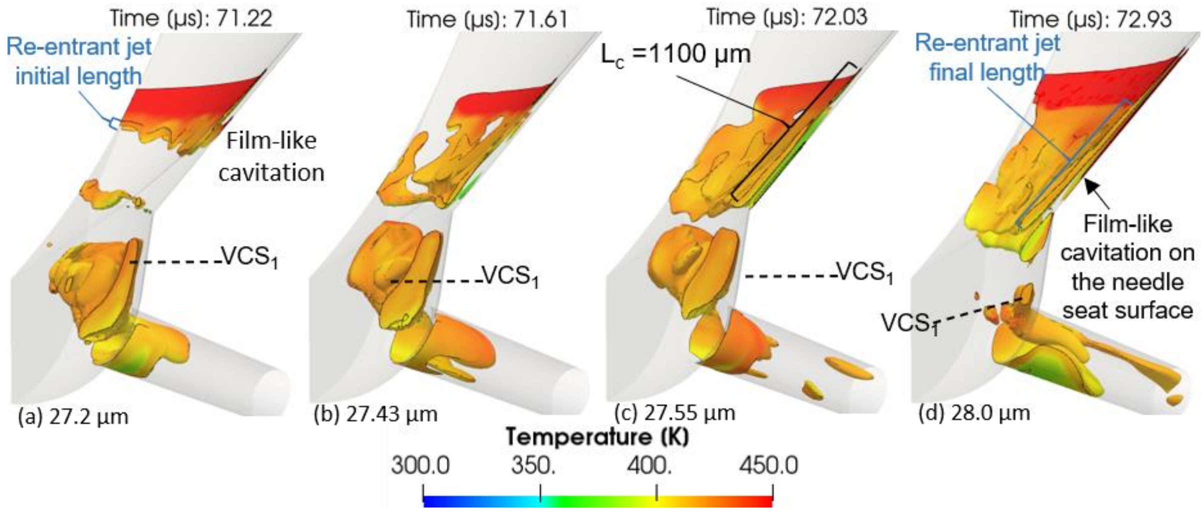

Figure 3. 9. Snapshots of vapor iso-volume coloured by fuel temperature with vapor volume fraction α = 0.01-1.0 of a representative vapor shedding cycle during the opening of the needle valve from 26.2 μm to 27.2 μm. The selected time instances from (a) to (d) correspond to those indicated in Figure 3.7.

The initial length of the re-entrant jet and the initial length of the detached cavity from the surface increase until they reach their maximum values, as shown in Figure 3.8(d). In order to define the frequency of the cavitation cloud shedding, the Strouhal number is calculated based on [200]. As observed from these consecutive instances, vortex cavitation appears within the sac volume; a wall-attached sheet cavity is also observed at the periphery of the nozzle orifice. In Figure 3.8(a), the sheet-to-cloud cavitation transition originates. The mean length of the attached cavity on the needle surface was chosen for the characteristic length L_c, as depicted in Figure 3.8(c), while the average velocity U_c is estimated to be ~650m/s. The number of the repeating shedding events during the opening phase is 28 and their duration is ~160μs. Using equation (3.11), the Strouhal number is ~0.3.

$$St = \frac{fLc}{Uc} \tag{3.11}$$

The normalised volume of cavitation formed during the injection period is shown in Figure 3.9. During the opening and closing of the needle valve, where cavitation dominates in the needle seat area and the sac volume, the vapor volume is normalised with the volume of the sac volume; while for the period of the injection cycle, where cavitation only appears inside the nozzle hole, normalisation is done using the volume of the injection hole. During the early opening stages of the needle valve, the amount of the vapor does seem to be noticeably higher for the full thermodynamic closure than that predicted from the barotropic model. This trend also persists over the whole simulation period.

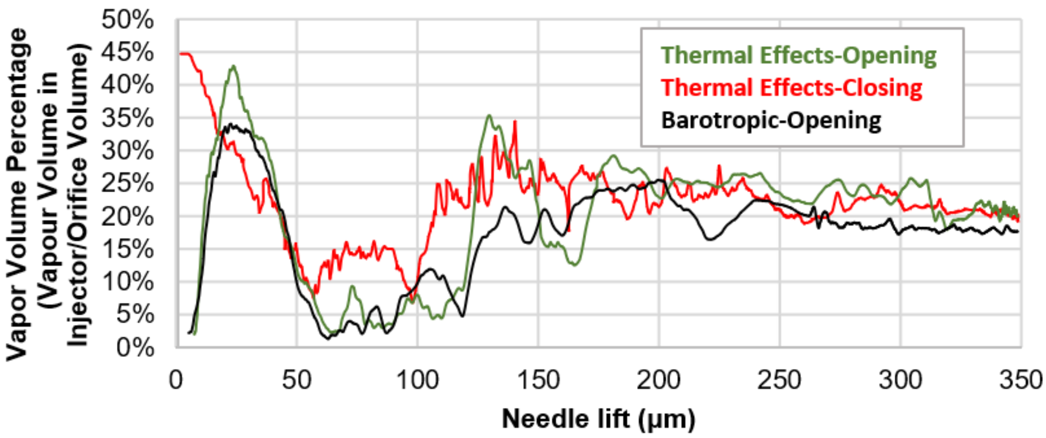

Figure 3. 10. Vapor volume fraction in the injector volume during the opening and closing phase of the needle valve. Before 150 μs (60 μm) and after 2950 μs (63 μm) the vapor volume is normalised with the total injector's sac and orifice volumes. During these times,

normalisation only with the orifice volume is performed. It is noted that at zero needle lift the sac volume is 3.1 times larger than the volume of the orifice.

During the early stage of closing, which lasts from 2500 µs (350 µm) to 2750 µs (257 µm) and denoted as ‘stage 3’ in Figure 3.6 and Figure 3.9, similar flow and cavitation patterns to those predicted during opening are realised. The injection period with the same flow characteristics mentioned as stage. Differences are realised during the following two stages; ‘stage 2’ lasts between 2750 µs (257 µm) and 2970 µs (63 µm) followed by ‘stage 1’ lasting from 2970 µs (63 µm) to 3015 µs (1.6 µm). The amount of cavitation vapor formed shows noticeable differences, up to 12% especially for lower than 35 µm needle lift and up to 15% between 120 and 140 µm needle lift. The amount of the vapor does seem to be noticeably different between opening and closing; calculated differences are 2%-3% for the same needle lift.

3.11 Differences between the thermodynamic closure 1 and 2

Figure 3.9 revealed that the vapor volume fraction values vary significantly during the injection event. At some local points the amount of the vapor shows noticeable increase with fluctuations for the full thermodynamic closure case when compared to the barotropic model. This is due to both viscous heating and the formation of different vortical and vapor structures into the sac and orifice volume, forming during the first and the second phases of the needle valve, respectively. As shown in Figure 3.10, the comparison between the different thermodynamic models reveals that the velocity, dynamic viscosity and temperature profiles show different trends; this explains the difference in the percentage of vapor volume fraction. The plotting slices into the orifice shown in Figure 3.10 are placed at the hole inlet, middle and just before the exit of the orifice. Comparison between Figure 3.10(a) and Figure 3.10(b) reveals that by neglecting the temperature variations in the case of the barotropic model leads to a more uniform density distribution; as a result, this leads to the suppression of the swirling flow developing inside the nozzle’s sac volume. Another reason for the differences between the full thermodynamic and barotropic model is the effect of the baroclinic torque, which cannot be included in a barotropic model, as it is by default zero when the barotropic assumption is utilised. The total derivative of vorticity ω for compressible non-barotropic flow is given, according to [201], by equation 3.11. The first term on the RHS of the equation is the compressibility term; compressibility increases vorticity, while the following term represents the change in vorticity from vortex stretching and tilting [202]. The third term is the rate change of vorticity due to baroclinicity effect [202]; this term is zero for a barotropic flow, since pressure and density spatial gradients are aligned; the last term represents the change from viscous dissipation.

$$\frac{D\omega}{Dt} = -\omega\nabla \cdot \boldsymbol{u} + \omega\nabla\boldsymbol{u} + \frac{\nabla\rho \times \nabla p}{\rho^2} + \nu\nabla^2\omega \tag{3.11}$$

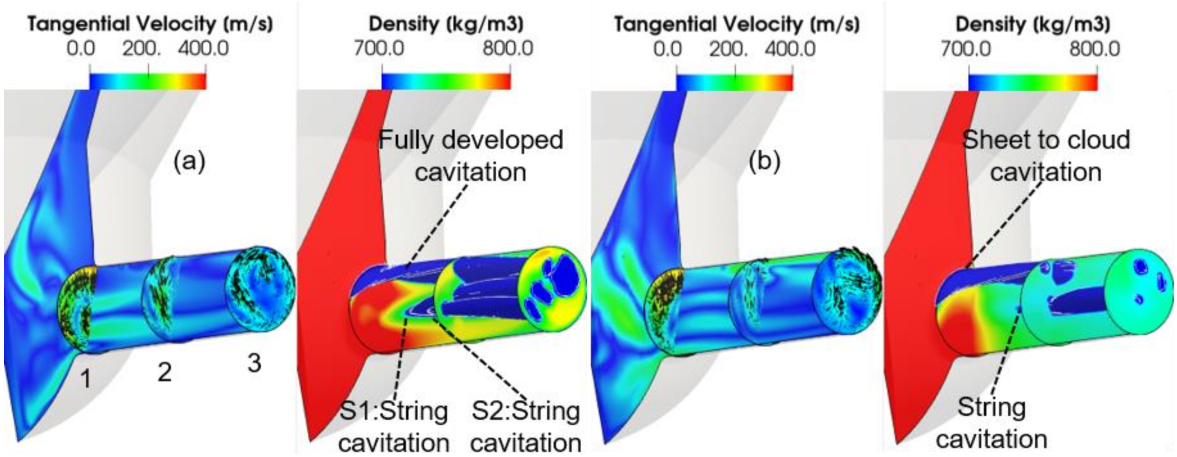

Figure 3. 11**.** Instantaneous tangential velocity and density distribution on slices normal to the orifice and at the midplane of the injector, at time instant 248μs (132 μm needle lift) using (a) full thermodynamic model and (b) barotropic model.

The injector's sac volume and orifice exhibit different temperatures as is depicted in the following Figures. Some regions are at inlet temperature (350K) or even lower, while others have temperature higher than 390K, due to viscous heating on the needle surface and on the orifice upper wall. As a result, the viscosity field is not uniform; that gives rise to vortex formation, which, in turn leads to formation of cavitation. These strong coherent large-scale vortices underlie on the needle tip surface or the sac volume, causing strong string cavitation extending into the orifice volume. Furthermore, in Figure 3.10(a), three different cavitation structures are evident, which have complex shapes. The first one is the fully developed cavitation at the upper surface of the orifice wall, which detached from the wall after slice 2. The other two cavitation structures are the two counter rotating vortices indicated as string cavitation S_1 and S_2 in Figure 3.10(a). S_1 and S_2 are long and narrow extending to the exit of the injection hole. The S_1 and S_2 are results of the strong swirl of the flow into the sac volume and due to acceleration of the flow as the cross-sectional area of the orifice decreasing.

3.12 Analysis of the flow field and vapor structures

At the first time instant, a highly fluctuating transition from sheet to cloud cavitation, creates a well-established vapor structure into the needle seat passage, as explained in Figure 3.8, forming a recirculation zone; The next depicted time instant highlights the interaction of vortex cavitation with the flow inside the sac volume up to the needle wall surface, as illustrated in Figure 3.11(b), while in Figure 3.11(c) the unstable cavitation structure occupies the region close to the sac wall and before the orifice entrance. One part of the fuel is moving backward into the passage close to the curve needle surface. At the same time, part of the fuel moves parallel to the sac vertical wall. As a result, the upwards flow collides with the high velocity jet, which comes through the needle seat passage at the sac inlet and changes the direction of the jet, as shown in Figure 3.11(b-d). The third column shows the detaching cloud sequence, which is a consequence of the vortex shedding. The vortex structure VC_1 gains rotation due to the vortex stretching. The size and circulation may be connected with the sheet length and the vapor cloud detachment [203].

In Figure 3.12, focus is placed on the visualisation of the swirl formation [204] and the evolution of vortex cavitation along the orifice length. During the second opening and closing phases, the flow is characterized by sheet-like cavities at the upper wall of the orifice and by aligned vortical vapor cavities into orifice volume. Coherent longitudinal vortical structures in the sac volume cavitate into the orifice volume. These vortices (C_1 and C_3) originate from the needle tip as depicted in Figure 3.12 (a) as strong unstable spiralling tip needle vortex and (c) or from the possible interaction with the other orifices like C_2, Figure 3.12(b). This is in agreement with the Helmholtz second theorem stating that vortices cannot terminate in the bulk of a fluid; they must attach on a solid boundary or form closed loops [205]. One significant observation is that at the centre of the initial core of these vortexes, C_1, C_2 and C_3 the Mach number is even lower than 0.1 because the velocity is too low. Due to the acceleration of the fuel into the orifice, the resulting streamwise velocity gradient stretches these vortices, the streamwise vorticity increases and when the pressure drops below the vapor pressure, vortex cavitation appears.

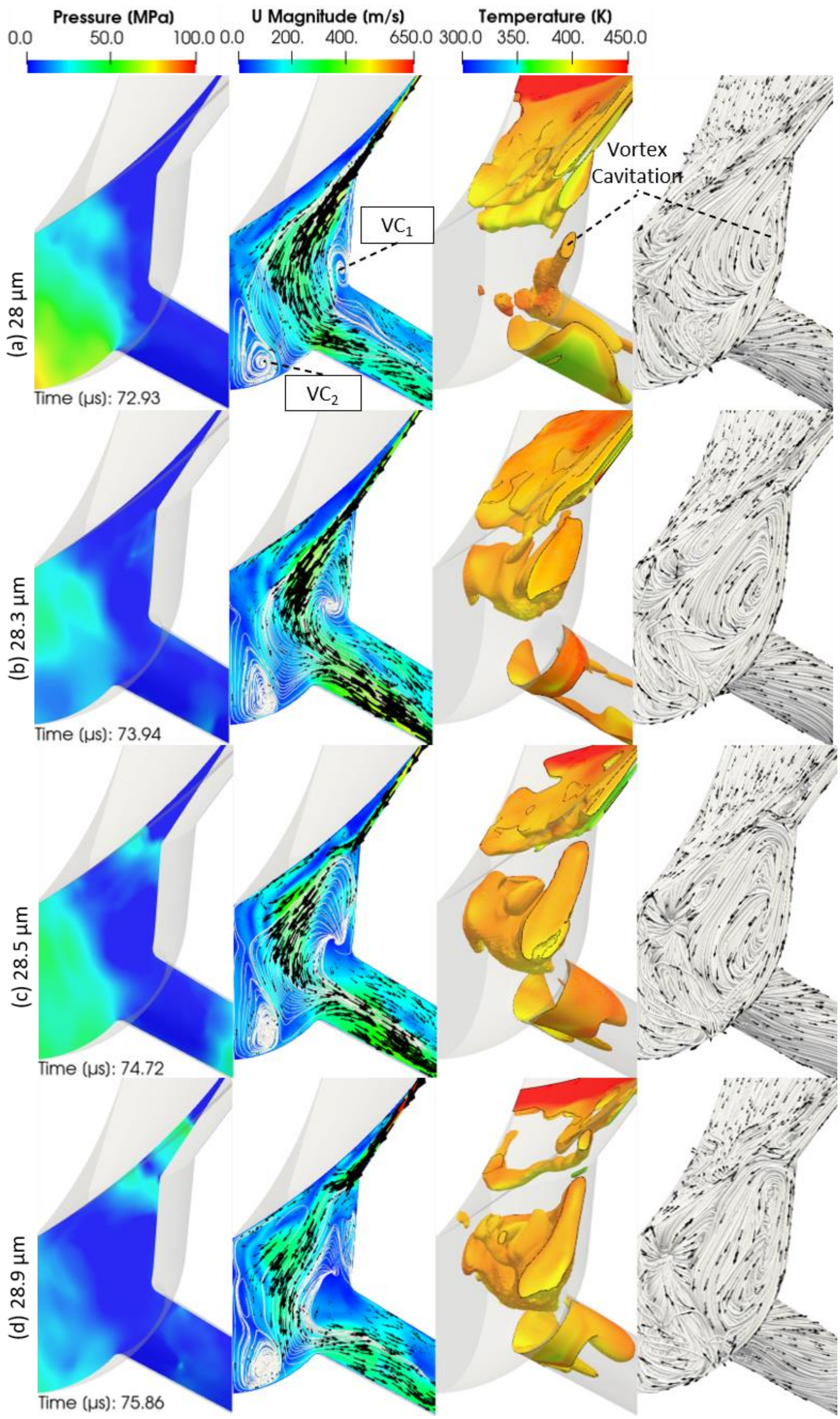

Figure 3. 12**.** 3D visualization of the flow during the needle movement from 28 µm to 29.2µm corresponding to; a representative vapor and vortex shedding cycle. Snapshots are presented at time instants (a)–(d) as indicated on the symmetry plane, showing the instantaneous pressure (first column), velocity field (second column); vapor volume fraction coloured with fuel temperature (third column) and flow streamlines (forth column) are also plotted.

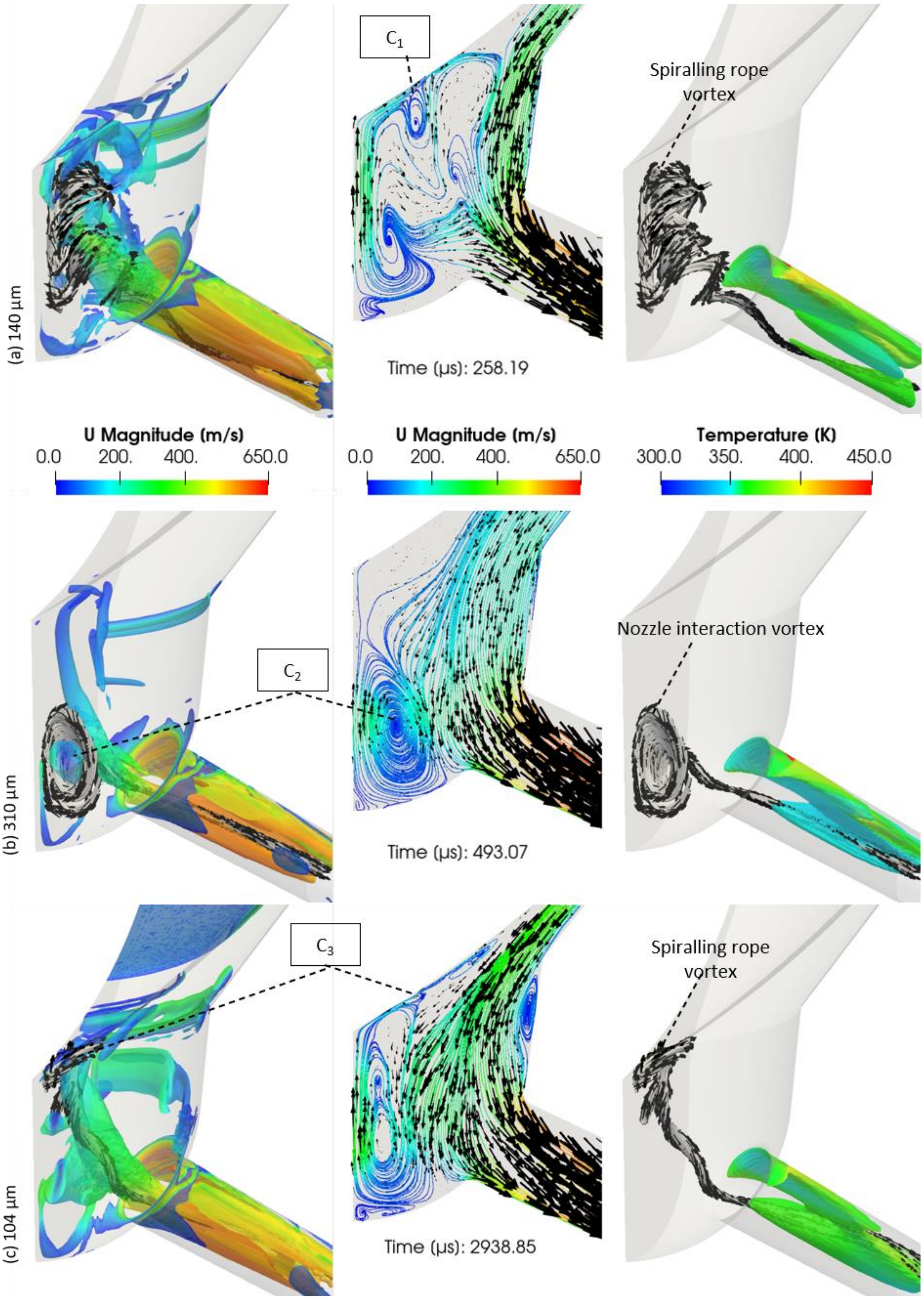

Figure 3. 13**.** 3D visualization of a representative vapor and vortex shedding cycle at time instances correspond to (a) 140 µm opening phase, (b) 310 µm opening phase and (c) 104 µm closing. First column: The iso-surfaces of q criterion with q = 2.2 × 10^{12} are colored by the velocity magnitude; Second column: flow streamlines at the midplane of the injector coloured by the velocity magnitude; Third column: vapor volume fraction coloured by fuel temperature and flow streamlines.

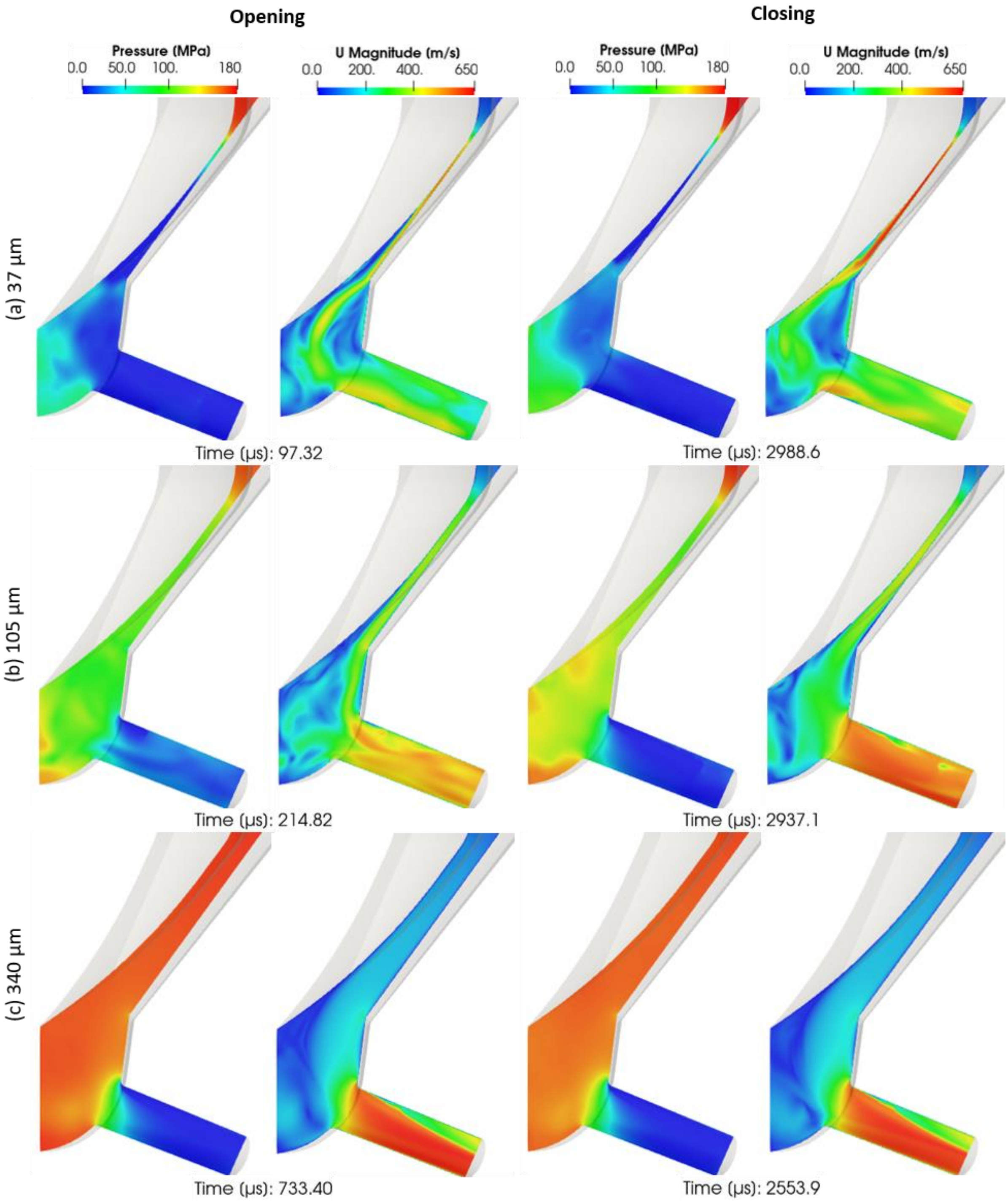

Figure 3. 14. Snapshots of instantaneous pressure and velocity magnitude at time instances corresponding to (a) 37 µm, (b) 105 µm and (c) 340 µm.

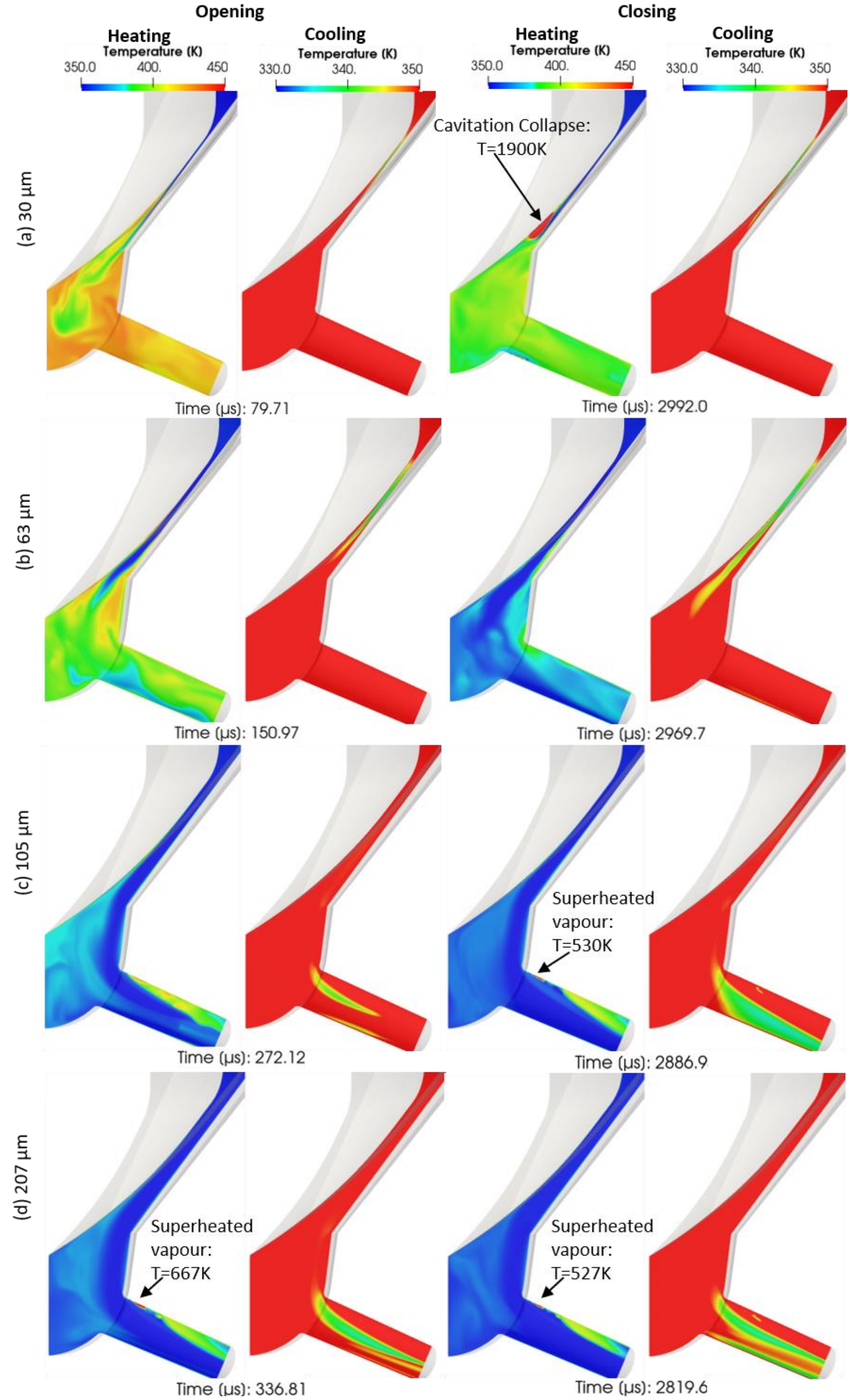

Figure 3. 15**.** Snapshots of instantaneous temperature field on the mid-plane of the injector. The time instants correspond to needle lifts (a) 30 µm, (b) 63 µm, (c), 150 µm and (d) 207 µm.

In Figure 3.13(a) and (b) the pressure and velocity magnitude fields reveal a different behaviour during the opening and closing phases. During the closing phase, higher fuel mass flow quantities are injected from the nozzle, due to the higher velocity magnitude; the descent of the needle pushes forcefully the fuel mass through the injector and therefore higher Cd is calculated.

Also, the unsteady flow of the fuel jet and the turbulence inside the sac volume create pressure variations in the sac volume which explain the different pressure field between the opening and closing phases at this low lift. At 105 μm needle lift during the closing phase, the downward needle displacement pushes the fuel, having feed temperature, through the needle into the sac volume and then towards the injection hole. The pressure inside the sac volume is ~150 MPa, while during the opening is approximately 5 MPa lower. The differences between the opening and the closing phase progressively disappear near full lift as illustrated at 340 μm.

3.13 Analysis of fuel heating and cooling

The fuel heating and cooling is shown on the mid-plane of the injector in Figure 3.14. As seen in Figure 3.14(a), at 30 μm the strong viscous heating produced by wall friction leads to higher fuel temperature during the opening of the needle valve than during its closing. At a higher needle lift of 63 μm, shown in Figure 3.14(b), both viscous heating and cooling of the fuel take place. Predictions indicate that the liquid fuel temperatures in the needle seat passage are 15K degrees lower than that of the inlet fuel temperature. As seen in Figure 3.14(b) the cooler fuel jet is more extended during the closing phase than in opening phase. Moreover, during the needle valve closing, the downwards displacement of the needle valve pushes the fuel from the sac volume towards the injection hole, resulting to a decrease of the average fuel temperature at the exit of the nozzle. With regards to the temperature of the vapor, at sufficiently high needle lift, the fuel temperature at the upper surface of orifice can exceed the fuel boiling temperature, resulting to superheated vapor.

Two additional processes affect the temperature of the formed vapor. During cavitation formation, the expansion of the vapor results in temperature decrease, while during vapor collapse, occurring further down inside the hole orifice, significantly higher temperature compared to the surrounding liquid are observed. Moreover, the faster closing phase plays a significant role on the development of different thermal boundary layer into the needle seat passage, as depicted in Figure 3.14(b) and (c). This fuel cooling process is related to the de-pressurisation of the fuel; the low pressure due to fuel acceleration and the absence of high-pressure gradients and velocity gradients at the centre of the needle seat passage. As seen, the cooler region in the orifice volume extends and covers a larger region of the orifice volume at higher Cd values. At a higher lift, the strong viscous heating produced by wall friction increases significantly inside the injection hole. The fuel temperature at the upper orifice surface can exceed the fuel boiling temperature. Figure 3.14(c)-(d), superheated vapor appears on the injector wall, close to the inlet.

3.14 Analysis of cavitation pattern

Figure 3.15(a) shows the vapor volume inside the injector at 15 μm needle lift during both the opening and closing phases; the cloud is additionally presented coloured by the local temperature. Part of the sac volume is occupied by a symmetric vortex cavitation pattern. The vapor inside the injector at this needle lift during opening is up to 27% of the nozzle's sac volume, while during closing even higher values up to 34% are calculated. At the same time, sheet cavitation is forming in the needle seat passage, while cavitation is also forming inside the injection hole. Until the 214.82 μs and 105 μm lift, cavitation inception forms at the entrance of the orifice, as seen in Figure 3.15(b). Before that injection time, cavitation forms close to the lower orifice surface and cavitation structures span in the whole orifice length forming thin string cavitation that may even exit from the orifice. Following, a transition of the cavitation from the lower to upper orifice surface is predicted while during most of the remaining injection time cavitation inside the orifice primarily originates from the top corner of the hole entry, while vortex (or string) cavitation is also observed. Although these patterns are present during both the opening and closing periods, some differences can be observed. In Figure 3.15(b) transition from sheet to fully developed cavitation formation is observed at the upper orifice surface and unstable streamwise aligned vortex cavitation structure appear in the orifice volume.

The differences on location, growth and appearance of vapor structures in Figure 3.15(b) are related to the higher Cd, around 0.1, predicted during closing and less to the level of heating because the temperature difference is only 20K. At 174 μm lift, coherent cavitation structures appear in the whole nozzle hole, as seen in Figure 3.15(c). Fully developed sheet cavitation formation is observed at the upper orifice surface and large scale vortical and vapor structures in the axial direction now dominate the flow. Due to the tapered shape of the nozzle holes, these vortices are further stretched and cause vortex cavitation.

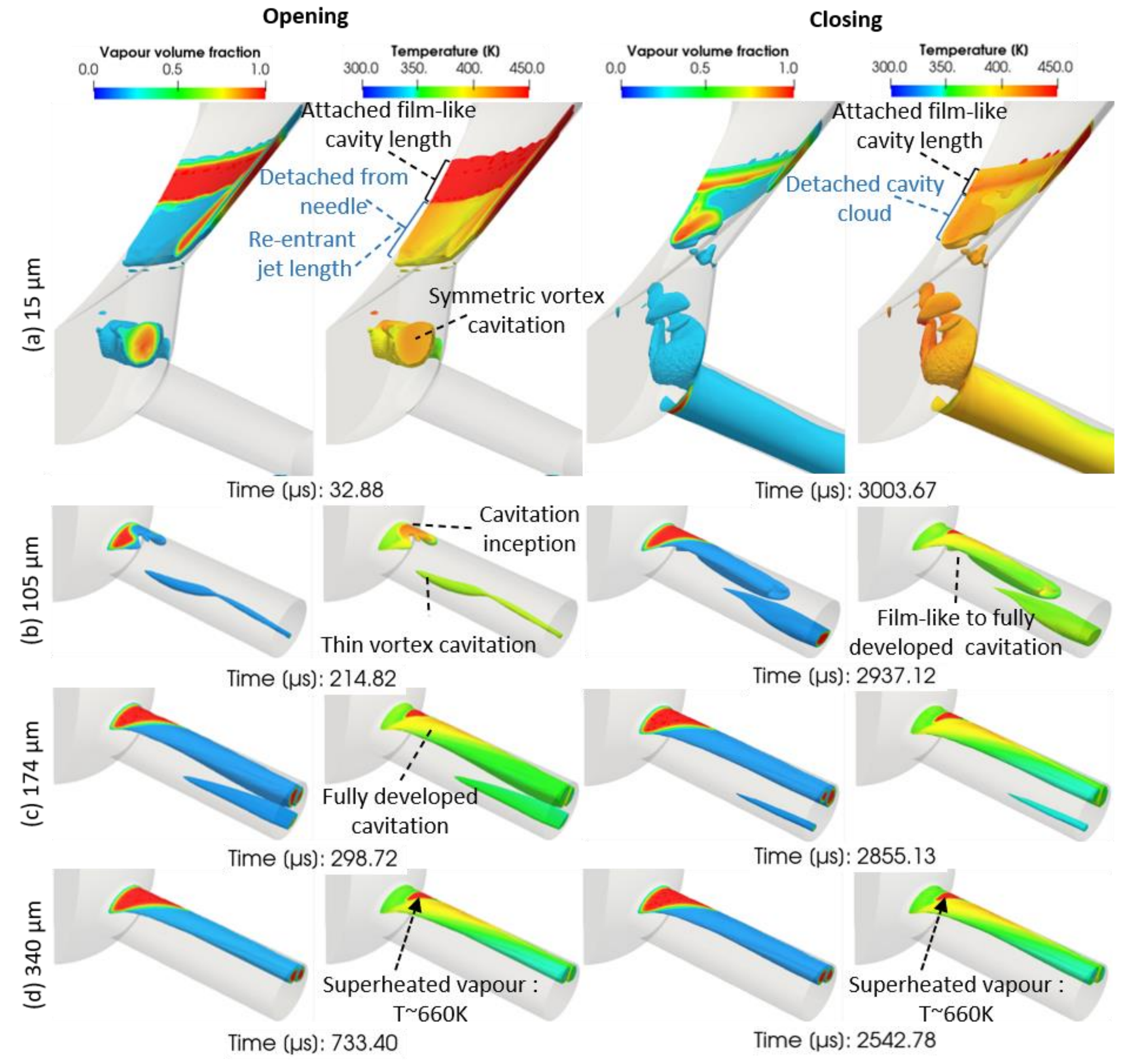

Figure 3. 16**.** Snapshots of cavitation formation coloured by the temperature and vapor volume fraction during the opening and closing of the needle valve. The time instants correspond to needle lifts (a) 15 μm, (b)105 μm, (c)174 μm and (d)340 μm.

The difference on location, growth and appearance of string cavitation in Figure 3.15(c) is connected to the higher level of fuel cooling at the centre of the orifice during the closing phase. As seen in Figure 3.15(d), at 340 μm lift, the amount of vapor is almost identical during opening; the same applies to the value of the Cd, average fuel temperature and the identical pressure, temperature and velocity magnitude fields.

3.15 Analysis of erosion pattern and erosion assessment

The determination of possible erosion areas during the design process of Diesel fuel injectors is a significant factor for efficient operation and durability. In Figure 3.16, the development of the potential erosion due to local maximum accumulated pressure peaks on the injector surfaces is shown. From the experiments a clear pattern is identified with erosion formation on the needle surface in the form of a deeply engraved ring shape. The pressure peaks are predicted in the needle seat passage region between 13 μm and 40 μm. Considering the other surfaces of the nozzle, sac is less affected by erosion very close to orifice inlet. In the nozzle holes, the injector is generally less prone to erosion damage, where minor pits on the top side of the injection hole entrance are observed. Moreover, some signs of erosion damage inside the sac volume exist. At the hole inlet, the two locations with potential erosion are predicted very well from the simulation results.

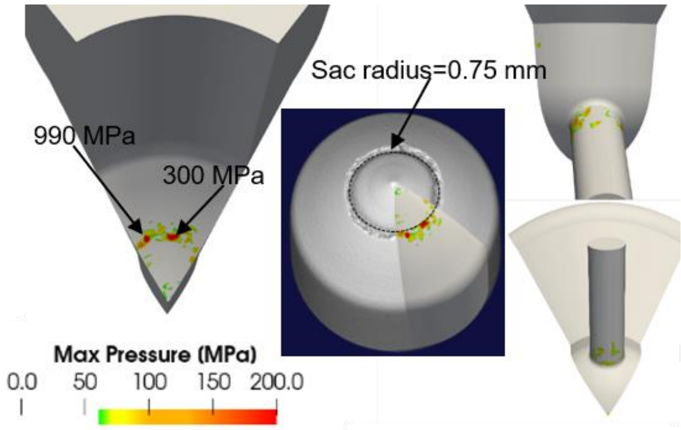

Figure 3. 17**.** Spatial distribution of accumulated pressure peaks on the surfaces of the needle valve, sac volume and injection hole; the black line denotes a radius of 0.75 mm where the erosion damage on the needle surface occurs.

The following Figure 3.17 depicts the pressure peaks pattern predicted during the opening and closing at the needle seat region. It is reminded that this small part of the closing phase lasts ~19μs, while the opening lasts ~80 μs. As it can be seen, high frequency local pressure fluctuations take place on the needle seat during the opening period. These fluctuations are the result of the sheet to cloud cavitation transition. However, strongest collapse events are located on the needle surface at the end of the injection phase. High frequency pressure peaks reaching levels of 300MPa and 990MPa during opening and closing, respectively. Based on the combined data of the collapse pressures and the distribution of maximum wall pressures, a significantly higher risk of cavitation erosion on the needle valve surface can be expected during the closing phase. The pressure peaks on the upper orifice surface, starts to form during the transition of cavitation from the lower to the upper orifice surface, as well as during the second stage of the opening, due to cavity shedding developing near this region at the same stages of closing phase. The scale of collapse pressures, like those on orifice entrance, may not be high enough to cause changes to injector material, but the high boiling temperatures, around 660K, with exposure time duration of 2ms at 340 µm lift potentially could potentially contribute to that [206]. The confirmation and noticeable observation for the erosion pattern into the needle seat passage is that erosion is predicted only on the needle surface at radius 0.75mm, in agreement with the experiments.

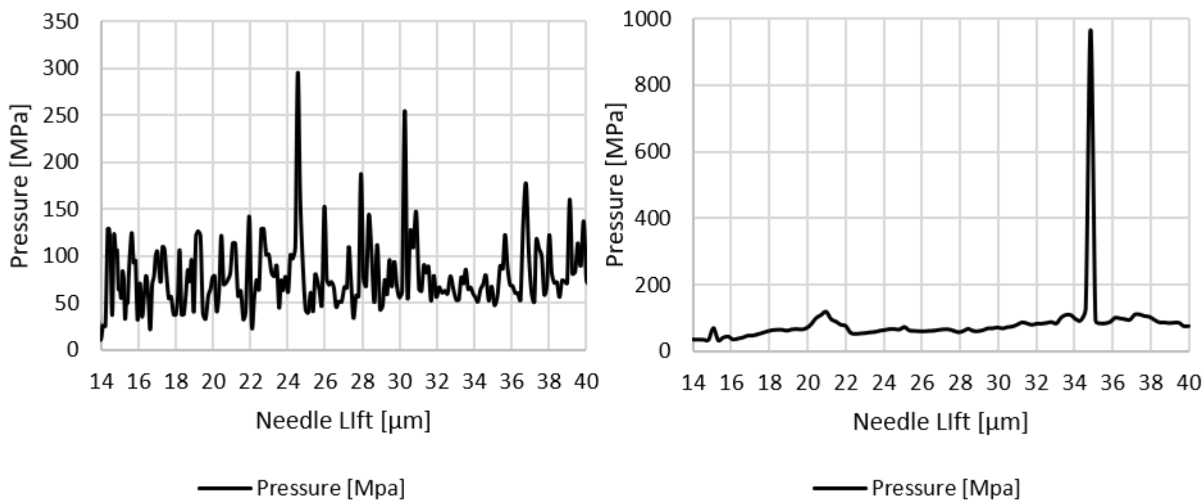

Figure 3. 18**.** Peak collapse detector pressures during the needle opening phase (right) and during the needle closing phase (left), recorded during the period when the needle lift moves between 14µm to 40.

3.16 Conclusions

A compressible explicit density-based solver of the Navier-Stokes and energy conservation equations has been employed for simulating the development of cavitation in a five-hole common rail Diesel injector geometry. Two thermodynamic closure models for the liquid, vapor and vapor liquid equilibrium (VLE) property variation as function of pressure and temperature were examined. The first is based on tabulated data for a 4-component Diesel fuel surrogate, derived from the Perturbed-Chain, Statistical Associating Fluid Theory (PC-SAFT) EoS and allowed for thermal effects to be quantified; the second was based on the widely used barotropic EoS approximation between density and pressure that neglects viscous heating. Model predictions were found in perfect agreement against 0-D estimates of the temporal variation of the mean fuel temperature difference between the injector's inlet and outlet during the injection period.

Two mechanisms affect the temperature distribution within the fuel injector. The first is ought to the strong viscous heating produced by wall friction, leading to significant increase of the fuel temperature at the upper orifice surface where local temperatures can exceed the fuel's boiling temperature and superheated vapor is forming. At the same time, liquid expansion due to depressurisation results to liquid cooling relative to the fuel's feed temperature; this is observed at the central part of the injection orifice.

These temperatures gradients induce significant variation of the fuel physical properties locally, which in turn, affect the formed flow structures and in particular the interaction between coherent vortical structures. While the sub-cooled region into the injector is more evident during the closing phase of the needle valve, the heated region is more pronounced during the opening phase; it is evident that the needle motion affects the thermal boundary layer and possibly the inception and cavity sheet growth and transition, especially at low lifts. The origin of these vortex cavitation structures was traced into the sac volume and on needle tip surface. Predictions from the full thermodynamic closure model for the peak pressures on the walls of the nozzle were also compared against corresponding X-ray derived surface erosion images obtained from durability tests. Locations of erosion on the surfaces of the needle valve, sac volume and injection holes were in good agreement with the relevant observations.

Overall, the comparison between those two thermodynamic closure models discloses that there are minor differences in the predicted nozzle discharge coefficient but significant differences in the temperature distribution inside the fuel injector, the mean injection temperature and the vapor volume fraction inside the injector's volume.

4 Transient cavitation and friction-induced heating effects of diesel fuel during the needle valve early opening stages for discharge pressures up to 450MPa

Abstract

Investigation of the fuel heating, vapor formation and cavitation erosion location patterns inside a five-hole common rail Diesel fuel injector, occurring during the early opening period of the needle valve (from 2μm to 80μm), discharging at pressures up to 450MPa, is presented. Numerical simulations have been performed using an explicit density-based solver of the compressible Navier-Stokes (NS) and energy conservation equations. The flow solver is combined with tabulated property data for a 4-component Diesel fuel surrogate, derived from the Perturbed-Chain Statistical Associating Fluid Theory (PC-SAFT) Equation of State (EoS), which allows for the significant variation of the fuel's physical and transport properties to be quantified. The Wall Adapting Local Eddy viscosity (WALE) LES model was used to resolve sub-grid scale turbulence while a cell-based mesh deformation Arbitrary Lagrangian–Eulerian (ALE) formulation is used for modelling the injector's needle valve movement. Friction-induced heating has been found to increase significantly with increasing pressure drop. At the same time, Joule-Thomson cooling up to 25 degrees local fuel temperature drop relative to the fuel's feed temperature are calculated. The extreme injection pressures induce fuel jet velocities in the order of 1100 m/s, affecting the formation of coherent vortical flow structures into the nozzle's sac volume.

4.1 Introduction

Although CO2 emissions during 2020 have decreased due to the COVID-19 pandemic, other global greenhouse gas concentrations (methane (CH4) and nitrous oxide (N2O)) in the atmosphere continue to rise. Overall, the short-term reduction in CO2 emissions is expected to have a negligible long-term impact on climate change [207]. At the same time, the forecasted unprecedented scale of COVID-19 economic recovery measures must consider sustainable low-carbon technologies that require implementation of long-term technology changes for achieving a reduction in emissions. The projected increases in heavy-duty global transportation-related energy demands through 2040 is driven by economic activity [3], which leads to increased commerce and movement of goods across oceans, nations and cities. For example, a light commercial vehicle (LCV) for intra-city deliveries has different energy needs versus a heavy commercial vehicle (HCV) for cross-country shipments of goods. Additionally, truck fleets are often quite different from region to region. Enhancements in technology and operations will improve the fuel efficiency and consumption in these diverse sectors, which is dependent on the type of truck and its use [3]. As electrification technologies and infrastructure for such continue to be developed, an energy and transportation powersystem portfolio consisting of a range of solutions including efficient engines with ultra-low emissions will be required to mitigate the environmental consequences of fossil fuel utilisation. High pressure fuel injection in particular and fuel composition are some of the key technologies affecting engine efficiency and emissions.

Diesel surrogates could lead to decrease in soot formation during combustion in Diesel engines [208], [209], [210], [211], [212], while multiple injections significantly reduce both soot and NOx emissions [213]. Also the increasing consumption of biofuels may give a major effect against global warming [214], [210], [215]. Experimental data has shown that increasing injection pressure will cause a reduction in soot formation [216]. An extended experimental study performed up to 320 MPa revealed that if the same mass is injected at higher injection pressures the injection and combustion processes may be optimized significantly. Combustion times are significantly reduced by injection pressure increase, as the atomization and vaporisation efficiency is improved [217]. Detailed experimental work analysed the behaviour of the evaporation, mixing and combustion of a diesel spray at injection pressures up to 500 MPa and revealed improved mixing results and higher spray velocities [130].

However, the µm-scale of injectors makes experimental flow characterization inside the injector challenging, especially under such high injection pressures. In particular, increasing injection pressure is linked to very high fuel velocities combined with high fuel temperatures, sharp pressures and temperature gradients, leading to formation of cavitation. Although cavitation collapse may remove surface deposits [132], [133] and improve primary jet break-up [135–138], it may also damage the injector material [139], [140] and reduce the injector mass flow rate performance [218] [219] [4] [10].

A limited number of studies address fuel heating/cooling and phase-change in high pressure Diesel injectors. In follow up work, [172], [4] the transient effects resulting from needle motion have shown significant variations in temperature during its opening/closing phase, suggesting that simulations performed at fixed needle lift cannot represent the actual phenomenon. Further, these works have utilised fuel properties from [173] and have not considered the link between cavitation and induced erosion. Recently, new experiments on the properties of diesel fuel at elevated pressures and temperatures have been performed, allowing for the development and calibration of the PC-SAFT EoS, as reported by the authors in [174–181]. Another study accurately predicted the thermal conductivity of fuels at high temperature and at 450 MPa pressure conditions using entropy scaling [176]. Relevant to this study, thermophysical properties such as density and viscosity were modelled using the PC-SAFT theory at pressures up to 4500 bar [181]. Theoretical predictions have been made for up to 400 MPa resulting in satisfactory accuracy for the density, isothermal compressibility and volumetric thermal expansion. Tabulated data has been derived for various fuel surrogates covering the range of properties variation occurring within high pressure fuel injectors and thus, allowing for accurate estimation of the effects of fuel property variation to be considered. The recent publication [220] described a more accurate way to predict the effect of a realistic multicomponent Diesel surrogate properties variation at different conditions using PC-SAFT [181]. The aim of the that work was to investigate the in-nozzle flow and cavitation formation in heavy-duty Diesel injector under fixed needle valve conditions, and up to 450 MPa injection pressure.

Still, such effects have not been studied in relation to transient effects caused by the motion of the needle valve up to 450 MPa injection pressure. From the above review, it seems that there are no relevant simulations or experiments reported for cavitation and induced erosion, while considering variable fuel properties due to temperature/pressure gradients, and incorporating transient effects caused by the motion of the needle valve. The aim of the current work is to address these phenomena and simulate the flow inside a high-pressure Diesel injector discharging at 180MPa, 350MPa and 450MPa. For this purpose, the explicit, density-based flow solver reported in [90] has been implemented in OpenFOAM and has been coupled with tabulated fuel property data derived from the PC-SAFT EoS, as documented in [174–180] and [182]. The injector needle valve movement is represented by the ALE approach, as proposed in [183], guaranteeing enforcement of the Space Conservation Law (SCL). One of the important features of the developed model is the incorporation of the Wall Adaptive Eddy (WALE) [184] LES model. Model predictions are also compared against the experimental data reported in [111] for a 5-hole diesel injector.

The paper is structured as follows: first, the mathematical and physical model is presented. Then, the discretization and the thermodynamic closure are analysed followed by the description of the Diesel injector geometry and the computational setup, followed by the analysis of the three-dimensional flow-field for the early opening injection phase; this includes analysis of viscous fuel heating and cooling due to depressurisation. Next, the flow-field for the early opening injection phase is presented while in the final section, the results from the computational analysis are compared with the erosion pattern retrieved from experiments. Limitations such as: (i) the lack of detailed validation against experimental data; (ii) the assumption of local mechanical and thermal equilibrium adopted; and (iii) the assumption of adiabatic nozzle walls, are evaluated in detail in [220], [221] and thus, they are not repeated here.

4.2 Mathematical and physical model

The explicit density-based flow solver is based on the works of [90], [111], [185] and [161]. The mathematical model employs a set of conservation equations governing the fluid motion, re-casted in a form of space conservation law suitable for moving/deforming meshes. The equations with a notation of [183] and written in weak (integral) form given below; bold denotes vector/tensor and italic scalar variables:

- Continuity equation:

$$\frac{\partial}{\partial t}\int_V \rho dV + \int_A (\rho \mathbf{u}_\mathrm{r}) \cdot \mathbf{n} dA = 0 \tag{4.1}$$

Here, ρ represents the fluid density, $\mathbf{u_r}$ is the relative velocity of the fluid in respect to the velocity of the moving grid, $\mathbf{u_g}$, defined as $\mathbf{u_r} = \mathbf{u} - \mathbf{u_g}$, $\mathbf{n}$ is the surface normal to the local grid face; *V* index implies volume integral and *A* surface integral.

- The momentum conservation equation:

$$\frac{\partial}{\partial t}\int_V \rho \mathbf{u} dV + \int_A \left(\rho \mathbf{u} \otimes \mathbf{u}_r\right)\cdot \mathbf{n} dA = -\int_A p \mathbf{n} dA + \int_A \boldsymbol{\tau} \cdot \mathbf{n} dA \tag{4.2}$$

Here, p denotes the fluid pressure and $\boldsymbol{\tau}$ is the viscous stress tensor, defined as:

$$\tau = \mu_{eff}[\nabla \boldsymbol{u} + (\nabla \boldsymbol{u})^T] - 2/3\mu \nabla \cdot \boldsymbol{u} \tag{4.3}$$

where μ_{eff} is the effective viscosity of the fluid, including both turbulent (μ_t) and laminar (μ) viscosities.

- Energy conservation equation:

$$\frac{\partial}{\partial t}\int_V \rho E dV + \int_A \left(\mathbf{u}_r \rho E\right)\cdot \mathbf{n} dA = -\int_A p\mathbf{u} \cdot \mathbf{n} dA + \int_A \left(k_{eff} \nabla T\right)\cdot \mathbf{n} dA + \int_A \left(\boldsymbol{\tau} \cdot \nabla \mathbf{u}\right)\cdot \mathbf{n} dA \tag{4.4}$$

where: E represents the total energy as the sum of internal energy, e, and kinetic energy $K = \frac{1}{2}u^2$, T is the temperature of the fluid and k_{eff} is the effective thermal conductivity of the fluid, including both turbulent (k_t) and laminar (k) thermal conductivity.

- The volume change of cells due to mesh motion can be expressed as:

$$\frac{\partial}{\partial t}\int_V dV + \int_A \mathbf{u}_r \cdot \mathbf{n} dA = 0 \tag{4.5}$$

For the system closure, expressions for pressure p and temperature T, are necessary to complete equations (4.2) and (4.4). These obtained from the thermodynamic closure, or Equation of State (EoS) employed, which enables to define relations of $T=f(\rho, e)$ and $p=f(\rho, e)$.

4.3 Thermodynamic model: Thermodynamic properties derived from the PC-SAFT EoS

Instead of solving the EoS for each time step, a technique similar to that described by the authors in [90] is employed. A structured thermodynamic table containing the thermodynamic properties derived from the PC-SAFT EoS [189] is utilised, as explained in [221].

4.4 Description of the examined injector and testing conditions

The simulated geometry is presented in Figure 4.1, while specific dimensions of the injector featuring slightly tapered holes are given in Table 4.1. The injector consists of five orifices, but only 1/5th of the full injector was simulated, employing symmetry boundary conditions. The computational mesh used consists of a hexahedral block-structured zone, while an unstructured tetrahedral zone is used in the sac volume upstream of the orifice entrance. Mesh motion is performed with a cell-based deformation algorithm, which moves the computational points and cells and stretches them uniformly. The needle lift was initially set at 1 μm with 5 cells placed in the needle seat flow passage. The initial flow field was obtained from a steady-state simulation performed at the minimum lift. The computational mesh of the sac volume and injection hole, which do not change throughout the simulation are shown in Figure 4.1c and Figure 4.1b, respectively.

	unit	value
Max. Needle radius	mm	1.711
Orifice length	mm	1.262
Orifice diameter Inlet	mm	0.370
Orifice diameter Outlet	mm	0.359
Sac volume	mm^3	1.190
K-factor (Din - Dout)/10	-	1.1

Table 4. 1. Geometric dimensions of the examined injector.

Table 4. 2. Boundary conditions at the inlet.

Property	unit	180 MPa Injection Pressure	350 MPa Injection Pressure	450 MPa Injection Pressure
Inlet pressure	[MPa]	180	350	450
Inlet Temperature	[K]	350	350	350
Inlet Density	[kg/m^3]	885.5	948.7	979.8

Table 4. 3. Boundary conditions at the outlet.

Property	unit	180 MPa Injection Pressure	350 MPa Injection Pressure	450 MPa Injection Pressure
Outlet pressure	[MPa]	5	5	5

Table 4. 4. Reynolds number into the injector.

	Reynolds number Needle seat	Reynolds number Sac volume	Reynolds number Orifice volume
180 MPa Test case	~55,000	~50,000	~55,000
350 MPa Test case	~60,000	~58,000	~61,000
450 MPa Test case	~72,000	~68,000	~70,000

The following values correspond to Taylor length scales, λ_g:

$$\lambda_g = \sqrt{10} Re^{-0.5} L \tag{6}$$

Figure 4.2 shows the inlet pressure and needle valve lift used as boundary conditions in the CFD simulations. Both 350MPa and 450MPa cases use the same boundary condition for the needle lift. However, it is noted that this lift profile is optimized for the 350 MPa case as predicted using an 1-D hydraulic system performance analysis software. The needle motion is assumed to be in the axial – z direction only. No eccentricity and residual fuel effects are considered; such effects are investigated in [153,155,156,222,223]. In Table 4.2 and Table 4.3, the numerical values for the reference state for the inlet and outlet, respectively, are provided. The simulations were carried out using the WALE model [194]. Based on the cell sizes indicated in Table 4.5 and the flow conditions, it is possible to make an estimate of the Taylor scales of fluid motion for this case, also shown in Table 4.5. The Taylor length scale gives a characteristic size of inertial scales transitioned to viscous scales and can be used as a resolution target that is respected in the LES. The time step used is 0.5 ns, which corresponds to an acoustic Courant number (CFL) ~ 0.7 for the 180MPa case and (CFL) ~ 0.5 for the 350MPa and 450MPa test cases. This is also smaller than the Kolmogorov time scale throughout the computational domain.

As shown in Table 4.4 the injector geometry has been divided in three topologies with different characteristics. The Reynolds number into the injector varies significantly between the needle seat, sac and orifice volume. Given the flow conditions inside the injector the Reynolds number is ~60,000 for the needle seat and orifice regions and ~45,000 inside the sac volume.

Table 4. 5**.** Taylor microscale of fluid motion for the injector's different part.

Region	**Taylor length scale 180MPa**	**Taylor length scale 350MPa**	**Taylor length scale 450MPa**	**Smaller cell 180MPa**	**Smaller cell 350/450MPa**
Needle Seat	3 μm	1.6 μm	1.4 μm	1 μm	1 μm
Sac Volume	9 μm	6.2 μm	5.5 μm	7 μm	5 μm
Orifice	4.7 μm	3.8 μm	3.4 μm	3 μm	1.8 μm

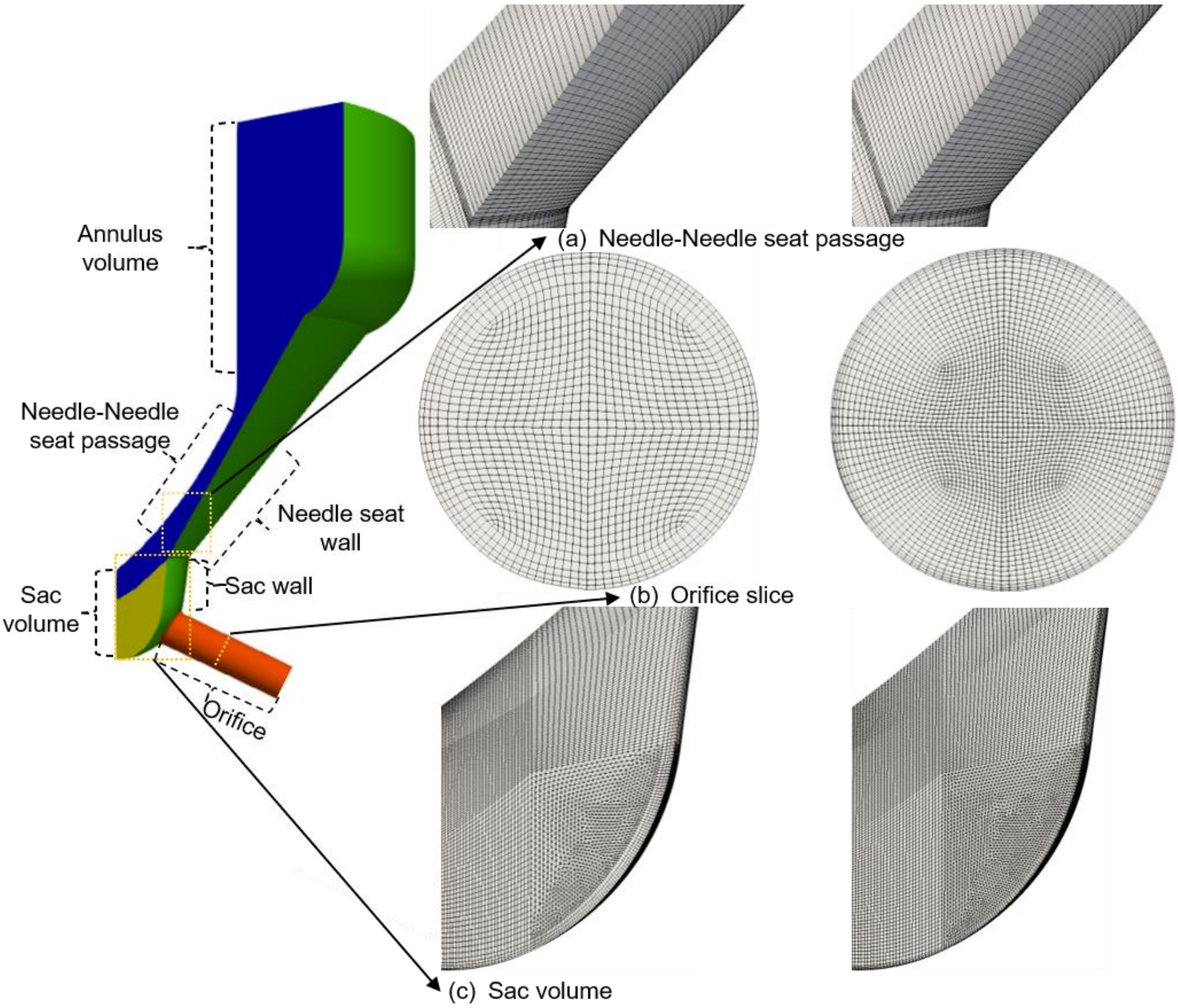

Figure 4. 1**.** Naming convention of injector surfaces and 3D view of the computational domains at 70 μm needle lift for different injection pressures.

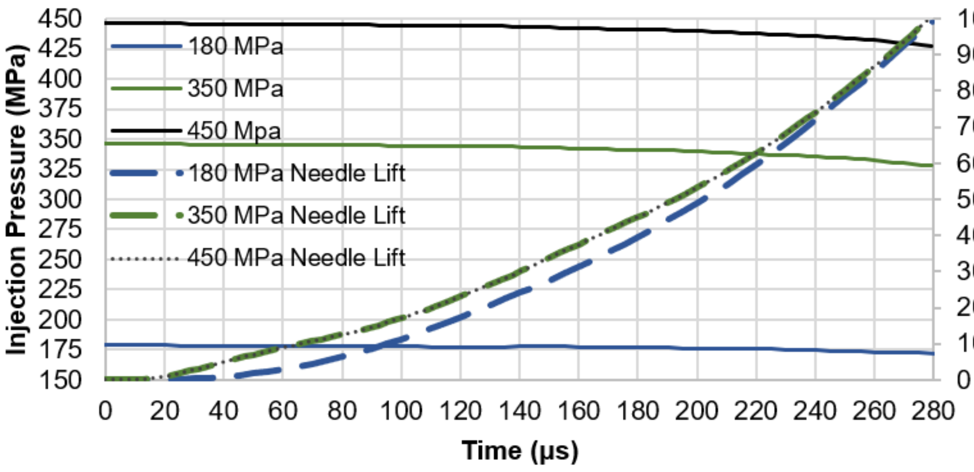

Figure 4. 2**.** Injection pressure and needle lift profile utilised as boundary conditions until 100µm needle lift.

4.5 Cavitation development during the early opening phase

During the early opening stage, which lasts between 0-80 µm, cavitation appears at the needle seat passage and inside the sac volume. Gradually, cavitation disappears from the needle valve seat and establishes only in the orifice volume; a transition of cavitation formation from the lower to upper side of the orifice entrance is predicted. As shown in Figure 4.3 the mass flow rate values are lower than 0.17 kg/s for the 180MPa case and lower than 0.25 kg/s and 0.3 kg/s for the other two cases, respectively. Using the theoretical mass flow rate from Table 4.6 the numerical model predicts a discharge coefficient (Cd) at needle lift 80 µm of ~0.89, ~0.78 and ~0.72.

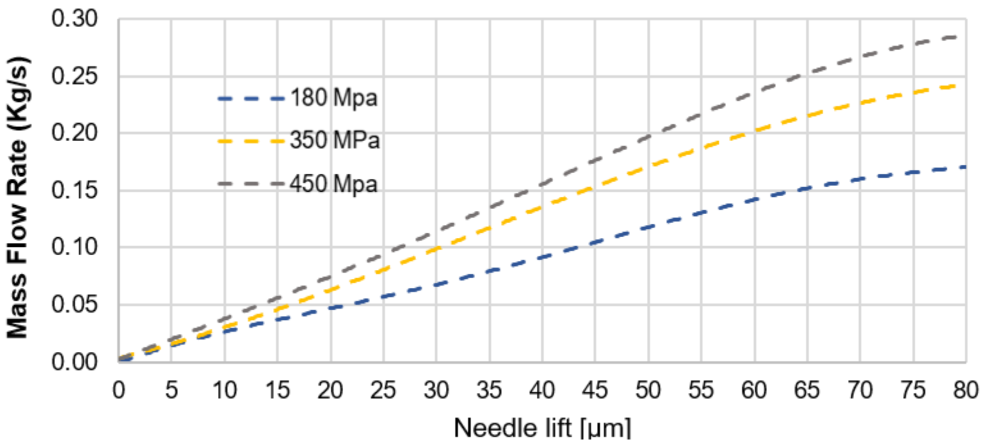

Figure 4. 3**.** Mass flow rate at the orifice exit for all cases.

Table 4. 6. Theoretical mass flow rate at 80 µm open needle valve.

Property	unit	180 MPa Injection Pressure	350 MPa Injection Pressure	450 MPa Injection Pressure
Mean pressure in sac volume	[MPa]	150	270	350
Mean density in sac volume	[Kg/m3]	853	872	890
Theoretical mass flow rate	[Kg/s]	0.19	0.31	0.39

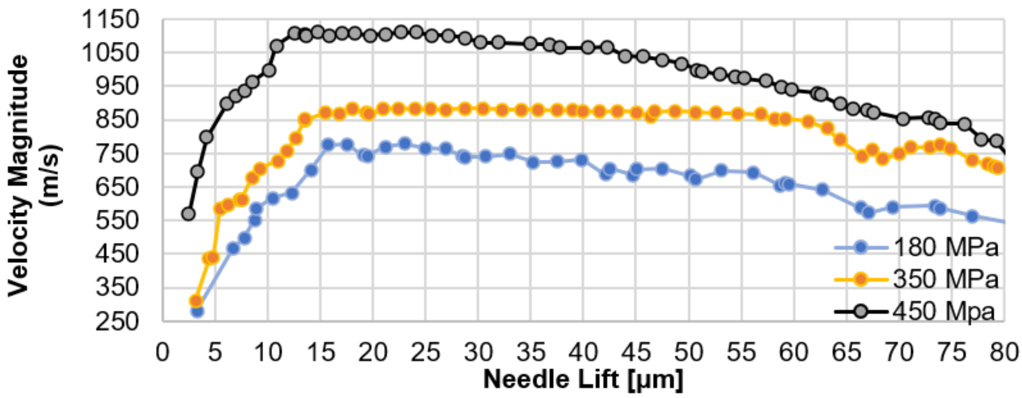

Figure 4. 4. Temporal evolution of maximum velocity magnitude at the narrowest point at the needle seat passage; lift increase from 0 µm to 80 µm during the simulated time.

Figure 4.4 shows the maximum velocity developed in the needle seat passage during this time period; For instance, at 20 µm the velocity for the 180MPa case is ~750 m/s and increases up to 850m/s and 1100m/s for the 350MPa and 450MPa, cases, respectively. The normalised volume of cavitation vapor during this injection period is shown in Figure 4.5. Vapor volume is normalised by the sum of the injector's needle seat passage, sac and orifice volumes. Cavitation dominates in the needle seat area and the sac volume. The increased pressures found overall also affect the amount of vapor volume. Differences are realised during the following two stages; 'stage 1' lasts between 0 µm and 20 µm, followed by 'stage 2' lasting from 20 µm to 60 µm. The instantaneous total amount of vapor in the domain shows noticeable differences especially for lower than 20 µm needle lift, up to 60%, 45% and 43% for the 450MPa, 350MPa and 180MPa cases, respectively. During stage 1, the amount of the vapor does seem to be noticeably higher for the 450MPa case; but this trend is seen only during that short period, where the needle valve is lift is below 20 µm.

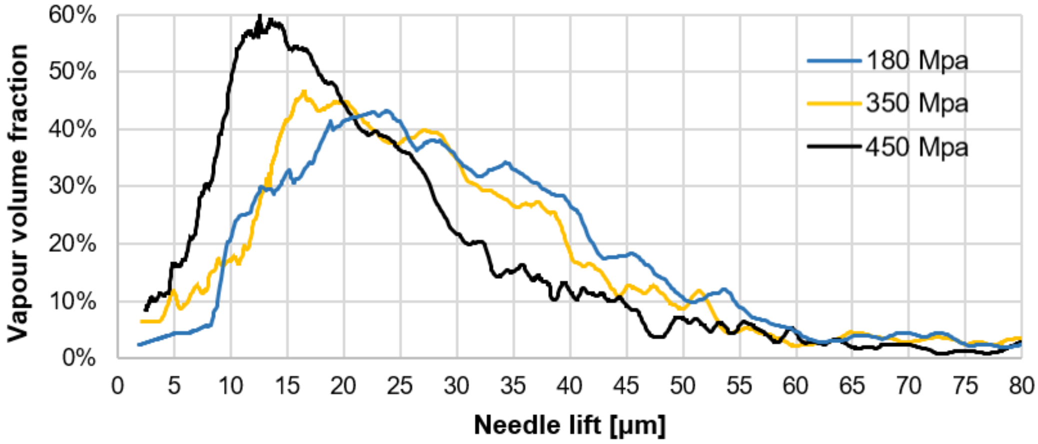

Figure 4. 5. Vapor volume fraction in the injector volume during the early opening phase of the needle valve. The vapor volume is normalised with the sum of the needle seat passage volume below the narrowest point, the injector's sac and orifice volumes. It is noted that at zero needle lift the sac volume is 3.1 times larger than the volume of the orifice.

During the early stage of opening, similar flow patterns for all injection pressure cases are predicted. Figure 4.6 shows the vapor volume inside the injector at different injection pressures, with the cavitation cloud coloured by the vapor volume fraction and the local temperature. In Figure 4.6(a) at 20 µm, needle lift sheet cavitation forms in the needle seat passage. Part of the sac volume is occupied by vortex cavitation pattern while cavitation is also forming inside the injection hole. Vapor appears on the needle surface wall, and the vapor temperature exceeds the fuel boiling temperature for both the 350 and 450 MPa cases. Fully developed cavitation as well as a cavitating vortex form for the higher injection pressures, while cavitation forms at the periphery of the entrance nozzle orifice for the 180MPa case. As seen in Figure 4.6(b), sheet cavitation in the needle seat passage has been reduced significantly for all cases when compared to Figure 6(a). The vapor volume inside the injector's sac volume has almost disappeared for the 450MPa case compared to the previous needle lift for the same injection pressure. However, at 180MPa cavitation is more extended compared to the 450 and 350 MPa cases for the same needle lift. This difference is related to the higher local pressures developing into the sac, as depicted in Figure 4.7. In Figure 4.6(c) cavitation remains on the needle upper surface for the 350 and 450 MPa cases due to higher jet velocity developing in needle seat passage.

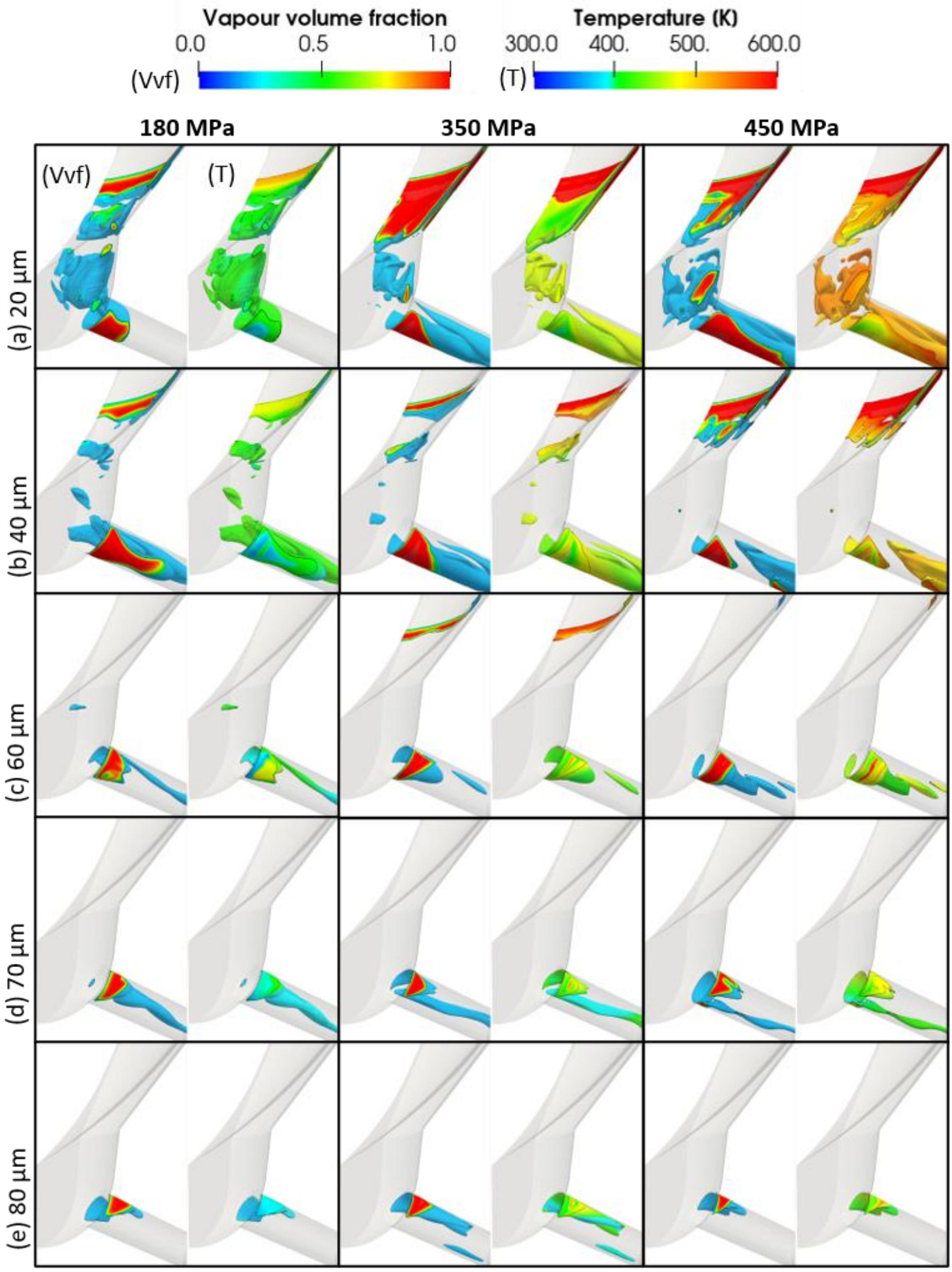

Figure 4. 6**.** Snapshots of cavitation formation coloured by both the vapor volume fraction and temperature during the opening of the needle valve. The time instants correspond to needle lifts of: (a) 20 µm, (b) 40 µm, (c) 60 µm, (d) 70 µm and (e) 80 µm.

There is no vapor formation inside the injector's sac volume for the 350 MPa and 450MPa cases. However, for the 180MPa case, vortex cavitation appears despite the fact that the vortex coherent structure is smaller than in the other two cases. In Figure 4.6(d) cavitation forms close to the upper orifice surface and cavitation structures span in the whole orifice length forming a thinner string cavitation for the 450MPa. In Figure 4.6(e) fully developed cavitation formation is observed at the upper orifice surface and unstable streamwise aligned vortex cavitation structure appear in the orifice volume. As seen in Figure 6(e), at 80 μm lift, the amount of vapor is almost identical between the 180MPa and 450MPa cases.

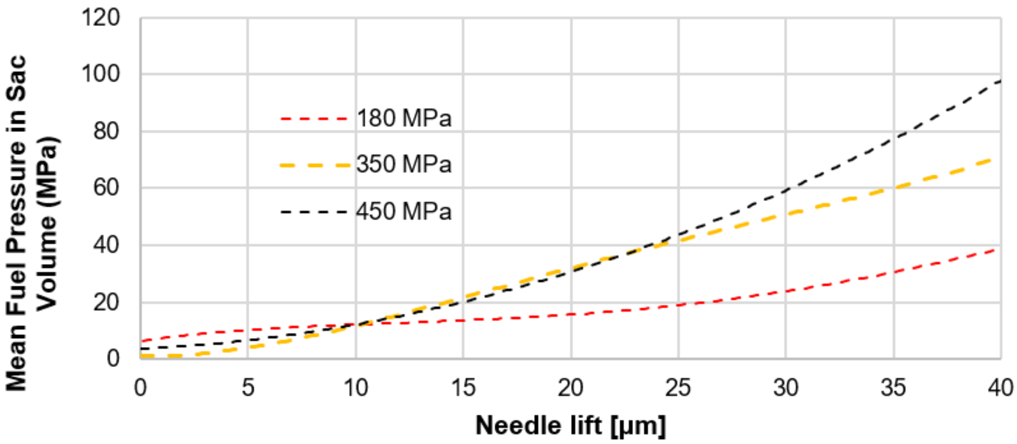

Figure 4. 7. Temporal evolution of fuel pressure in the injector's sac volume; lift increase from 0 μm to 40 μm during the plotted time.

4.6 Analysis of fuel heating and cooling

CFD predictions have been obtained assuming an initial fuel temperature of 350K. As shown in Figure 4.8, the comparison between the temporal evolution of fuel temperature at the exit of the injector's orifice and at the sac volume entrance reveals that the temperature profiles show different trends even for the same injection pressure.

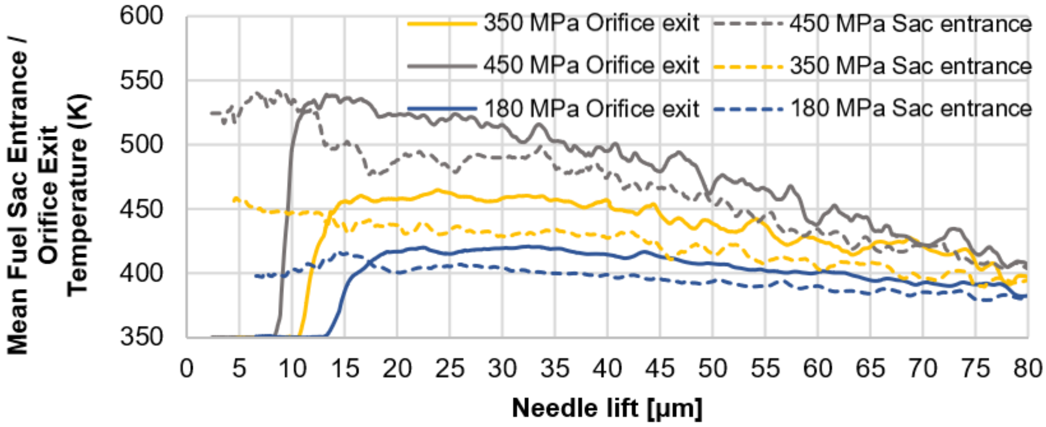

Figure 4. 8**.** Temporal evolution of fuel temperature at the exit of the injector's orifice (solid lines) and at the sac entrance (dashed lines); lift increase from 0 µm to 80 µm during the plotted time.

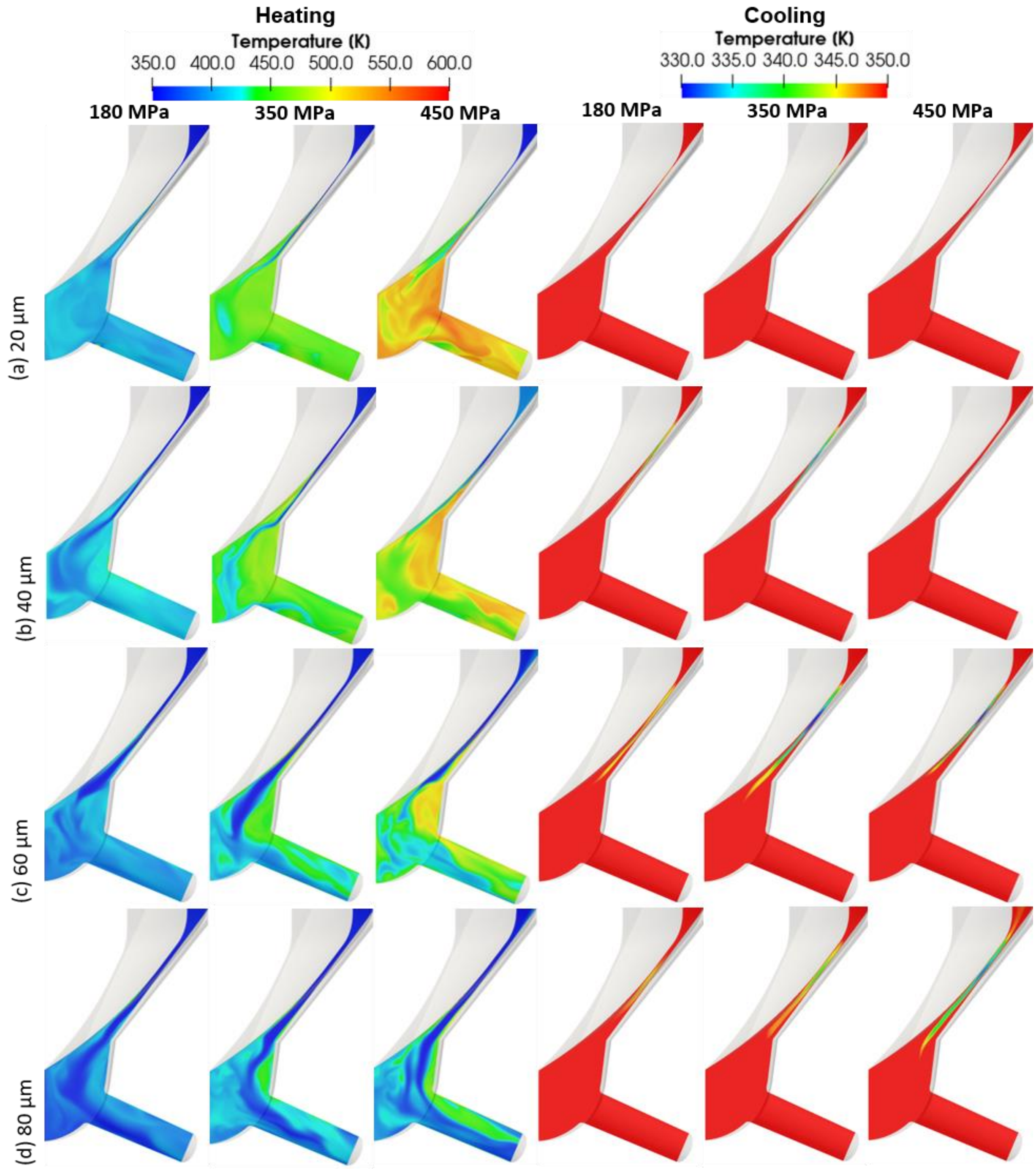

Figure 4. 9**.** Snapshots of instantaneous temperature field on the mid-plane of the injector. The time instants correspond to needle lifts of: (a) 20 μm, (b) 40 μm, (c) 60 μm and (d) 80 μm.

An increase in temperature is observed, particularly during the needle early opening, 0 – 15 μm, where an increase up to ~80, ~110 and ~180 degrees is estimated for the 180, 350 and 450 MPa injection pressures, respectively. This pattern after the needle seat passage may be caused by the presence of the cooling effect for all the cases after that 60 µm lift. Another observation is that the average fuel temperature at sac entrance is very close to the average fuel temperature at orifice exit for all cases only before the fuel jet into the needle seat passage reaches the maximum velocity profiles, as depicted in Figure 4.4.

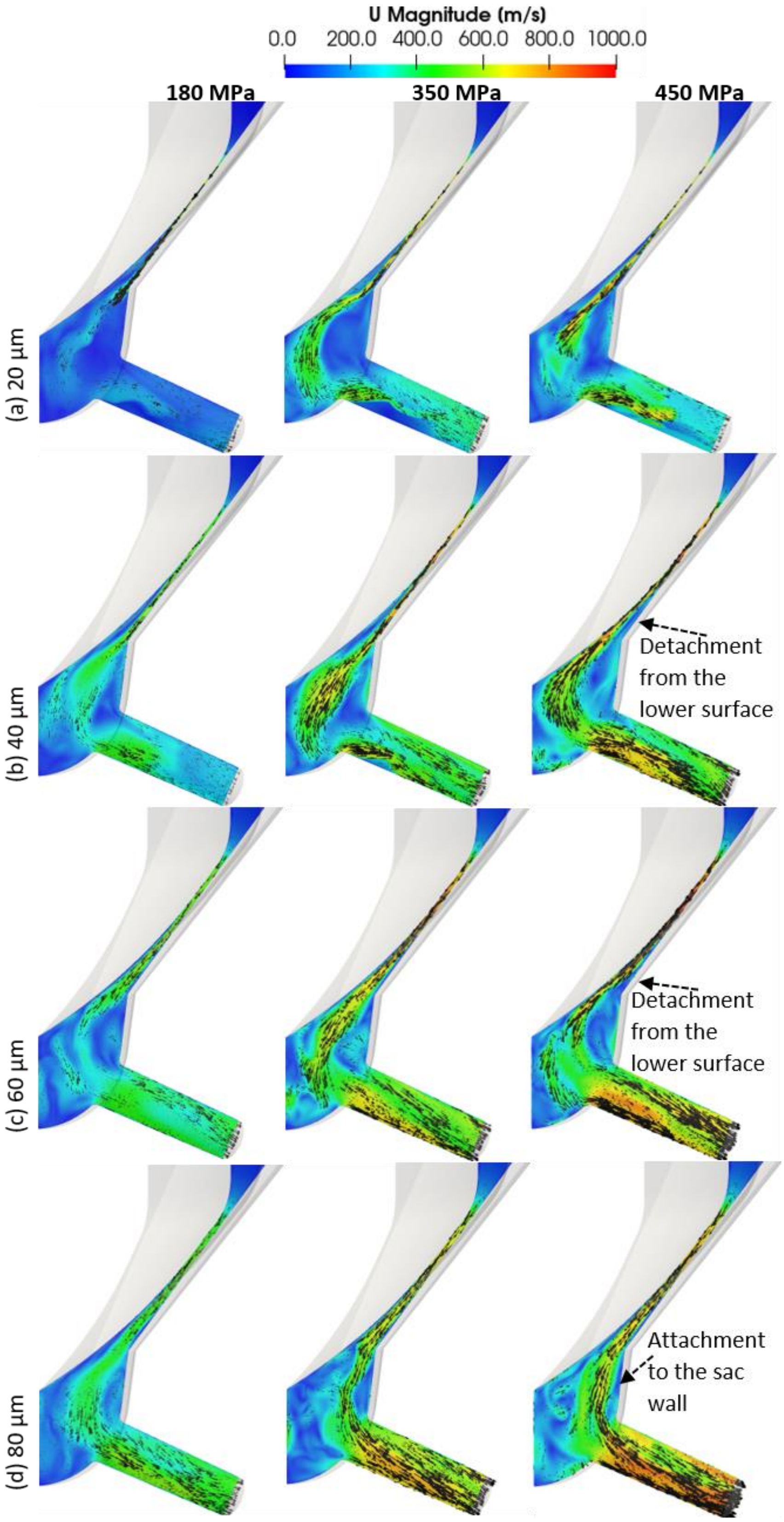

Figure 4. 10**.** Snapshots of instantaneous velocity magnitude and flow field vectors plotted at time instances corresponding to (a) 20 µm, (b) 40 µm, (c) 60 µm and (d) 80 µm.

After 60 μm lift a gradually smaller difference is observed for the temperature profile between the sac entrance and the orifice exit. The increase of the fuel temperature after entering the sac volume increases with the increase of the injection pressure, due to the more pronounced effect of viscous heating. The fuel heating and cooling during the opening of the needle valve is shown on the mid-plane of the injector in Figure 4.9. As seen in Figure 4.9(a), at 20 μm the strong viscous heating induced by wall friction leads to higher fuel temperature for the 450MPa case, while there is initial fuel cooling at the narrowest gap of the passage only for the 180 and 350MPa cases. This fuel cooling process is related to the "Joule-Thomson effect".

4.7 Analysis of the flow field and vortex structures

In Figure 4.10 the velocity magnitude fields reveal a similar behaviour during the opening under different injection pressures but with some significant differences about the flow near to sac vertical wall. The unsteady flow of the fuel jet and the strong turbulence inside the sac volume make the jet detach from the needle seat surface as depicted in Figure 4.10(b,c) for the 450MPa case, while for the other cases the jet remains attached during the early opening. Also, at 80 μm needle lift in Figure 4.10(d) the flow is more attached to the vertical wall of the sac volume for the 450MPa case.

In Figure 4.11, focus is placed on the visualization of the vortex formation and its evolution into the sac volume. The depicted time instances highlight the interaction of this vortex structure with the flow inside the sac volume up to the needle wall surface, as illustrated in Figure 4.11(a-b). One part of the fuel is moving backward into the passage close to the curve needle surface. At the same time, part of the fuel moves parallel to the sac vertical wall, and as a result, the upwards flow collides with the high velocity jet, which comes through the needle seat passage at the sac inlet and changes the direction of the jet. In Figure 4.11 a large unstable vortex structure occupies the region close to the sac wall and before the orifice entrance, while a smaller vortex structure is developing at the lower surface of the center region of the sac volume. One significant observation is that the vortices' locations are the same for all cases. However, their growth is different; the higher the injection pressure the stronger the upper vortex with velocity magnitude (close to sac vertical wall) reaching 300 m/s, 380 m/s and 500 m/s, for the three injection pressures, respectively, as shown in Figure 4.11(a-b).

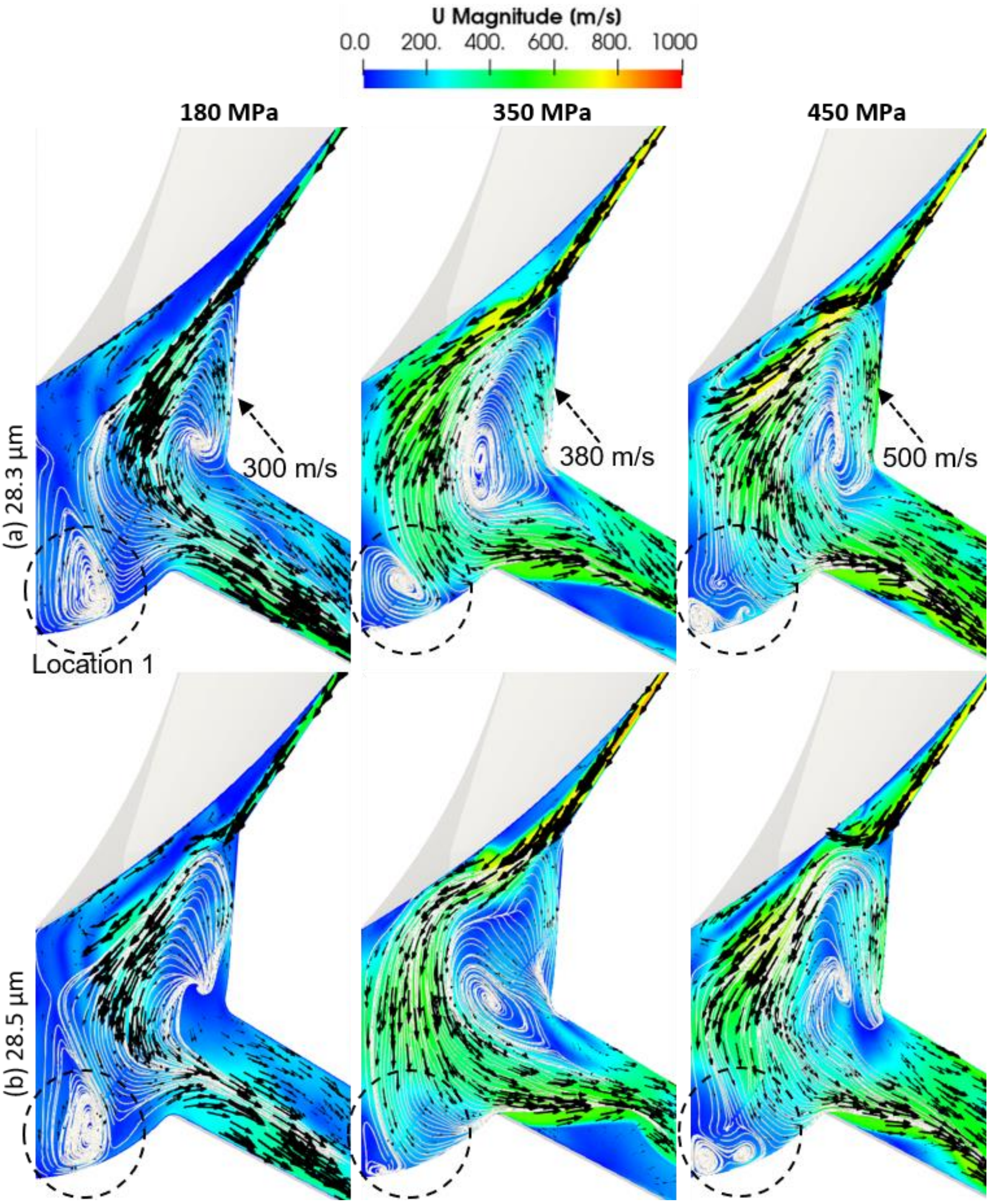

Figure 4. 11**.** Snapshots of the predicted flow field and flow streamlines at selected time instants (a) and (b).

4.8 Analysis of erosion pattern and erosion assessment

The mitigation of possible erosion areas during the design process of Diesel fuel injectors is a significant factor for efficient operation and durability. In Figure 4.12, potential erosion areas, due to local maximum accumulated pressure peaks on the injector surfaces, are shown. From the experiments, a clear pattern is identified with erosion formation on the needle surface in the form of a deeply engraved ring shape, as analysed in [111]. The pressure peaks are predicted in the needle seat passage region between 10 μm and 45 μm needle lift. Considering the other surfaces of the nozzle, the sac is less affected by erosion very close to the orifice inlet. In the nozzle holes, the injector is generally less prone to erosion damage, where minor pits on the top side of the injection hole entrance are observed. Moreover, some signs of erosion damage inside the sac volume exist. The value of the pressure peaks and the location of the erosion ring on the upper orifice surface are strongly corelated with: (1) the vortex pattern in the sac volume; and (2) with the velocity of the fuel jet, from the needle seat passage to sac volume. As reported in[111], [221], these locations of cavitation erosion for the 180MPa case have been confirmed experimentally. However, under higher injection pressures, there is no experimental data.

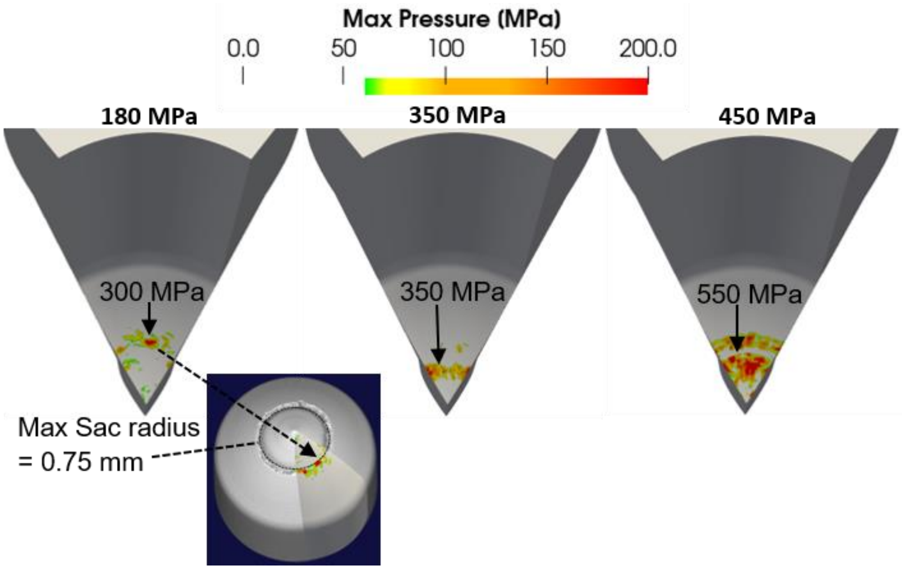

Figure 4. 12**.** Spatial distribution of accumulated pressure peaks on the surfaces of the needle valve. Strongest collapse events are located on the needle surface, reaching up to 550MPa for the 450MPa case.

4.9 Discussion

Two mechanisms affect the temperature distribution within the fuel injector. The first is due to the strong viscous heating produced by wall friction, leading to significant increase of the fuel temperature at the upper orifice surface, where local temperatures can exceed the fuel's boiling temperature and superheated vapor forms. At the same time, liquid expansion due to depressurisation results in liquid cooling relative to the fuel's feed temperature. This is observed at the central part of the injection orifice. Results indicate that with increasing injection pressures, an unprecedented decrease of cavitation volume inside the fuel injector occurs. This has been attributed to the shift of the pressure drop from the feed to the back pressure within the injection orifice as fuel discharges. Moreover, a significant increase of temperature in the needle seat passage takes place during the early stages of the needle valve opening, due to the very high velocity magnitude, on the of order 1000m/s. Additionally, stronger fuel cooling at the bulk of the flow is predicted. It is evident that the needle motion affects the thermal boundary layer and the inception and growth of the formed cavity sheet, especially at low needle lifts. Finally, the size and growth of strong vortices inside the sac volume influence the locations expected to be more vulnerable to cavitation erosion. Overall, the comparison between these injection pressures discloses that there are minor differences in the predicted mean fuel temperature and vapor volume after 60μm, but significant differences in the temperature distribution and vapor volume inside the sac, needle and orifice injector regions from 0 to 60 μm.

4.10 Conclusions

A compressible explicit density-based solver of the Navier-Stokes and energy conservation equations has been employed for simulating the development of cavitation in a five-hole common rail Diesel injector. The thermodynamic closure model is based on tabulated data for a 4-component Diesel fuel surrogate, derived from the Perturbed-Chain, Statistical Associating Fluid Theory (PC-SAFT) EoS, which enabled the strong variation of fuel properties with injection pressure to be quantified. It is evident that a reliable prediction transient cavitation (erosion-sensitive areas due to collapse events) and friction-induced heating effects during the needle moving can only be predicted accurately by including the unsteady needle motion.

In the present study, the effect of non-condensable gas which is necessary to understand how the flow phenomena inside a high-pressure injection system (450MPa), like fuel temperature distribution, turbulence, vortex cavitation and vapor, influence jet and spray formation and atomization characteristics for a more efficient mixing and combustion process, has not been considered.

Chapter 5 Preferential cavitation and friction-induced heating of multi-component Diesel fuel surrogates up to 450MPa

Abstract

The present work investigates the formation and development of cavitation of a multicomponent Diesel fuel surrogate discharging from a high-pressure fuel injector operating in the range of injection pressures from 60MPa to 450MPa. The compressible form of the Navier-Stokes equations is numerically solved with a density-based solver employing the homogeneous mixture model for accounting the presence of liquid and vapor phases, while turbulence is resolved using a Large Eddy Simulation approximation. Simulations are performed on a tapered heavy-duty Diesel engine injector at a nominal fully-open needle valve lift of 350 µm. To account for the effect of extreme fuel pressurisation, two approaches have been followed: (i) a barotropic evolution of density as function of pressure, where thermal effects are not considered and (ii) the inclusion of wall friction-induced and pressurisation thermal effects by solving the energy conservation equation. The PC-SAFT equation of state is utilised to derive thermodynamic property tables for an eight-component surrogate based on a grade no.2 Diesel emissions-certification fuel as function of pressure, temperature, and fuel vapor volume fraction. Moreover, the preferential cavitation of the fuel components within the injector's hole is predicted by Vapor-Liquid Equilibrium calculations; lighter fuel components are found to cavitate to a greater extent than heavier ones. Results indicate a significant increase of temperature with increasing pressures due to friction-induced heating, leading to a significant increase in the mean vapor pressure of the fuel and an increase of the mass of fuel cavitating, but at the same time to an unprecedented decrease of cavitation volume inside the fuel injector with increasing injection pressure. This has been attributed to the shift of the pressure drop from the feed to the back pressure inside the injection hole orifice as fuel discharges; as injection pressure increases, so

does the pressure inside the orifice, confining the location of cavitation formation to a smaller volume attached to the upper part of orifice, thus restricting cavitation growth.

5.1 Introduction

The United Nations Environment Programme (UNEP) reported in November 2018 mentions that “pathways reflecting current nationally determined contributions imply global warming of about 3°C by 2100, with warming continuing afterwards” in its assessment of the Paris Agreement [207]. As the transport sector accounts for ~23% of the total Greenhouse Global Emissions [3], attempts have been made to study and find a means to reduce them, including utilisation of Diesel surrogates [208], additives in Diesel and bio-Diesel blends [214], multiple injections per power cycle [213] and in- crease in injection pressure [216]. Modern Diesel engines operate with upstream pressures of around 200MPa at full load, although the current trend is to increase them up to 300MPa, in accordance with the latest emission regulations. Experimental studies have been done regarding sprays at extreme injection pressures, up to 500MPa [130], reporting an increase in the spray tip penetration, better mixing, and flame stability, potentially driving towards a better combustion and less emissions. However, due to the micrometre scales of injectors, high injection pressures will irremediably cause very high fuel velocities which, combined with the sharp geometric changes in the injector passages, lead to local depressurisation with significant pressure gradients. If the pressure decreases be- yond the fuel’s saturation point, the fuel cavitates, which in turn, results to injector underperformance [218] while it is related to mass flux choke due to blocking of the free flow [219] and possible cavitation erosion. Despite this, cavitation can be beneficial when man- aged effectively, as it promotes liquid jet atomisation [138,224–227] in- creases the spray cone angle [228] and thus, mixing and combustion [229] is enhanced. As cavitation measurements with real size injectors operating pressures beyond 200 MPa [199,230] is not possible up to now, simulation models can offer further insight into the nozzle flow. Both the Volume of Fluid method (VOF) [231,232] and the Homogeneous Equilibrium Model (HEM) [233] have been used to simulate the presence of the second phase due to cavitation and validated against relevant experiments at lower pressures [234]. Such models can be used to study the formation and transport of the vapor phase, the turbulent fluctuations in velocity and pressure and the effect of non- condensable gases [34]. It has been also possible to look into the effect of liquid and vapor compressibility on supercavitation formation [235]. An additional complexity related to the increase of injection pressure in modern fuel injection systems is related to the strong velocity gradients that induce wall friction, generating an important source of heating [4,10]. Nonetheless, thermal effects are typically neglected in relevant simulation studies and the flow within the fuel injector is considered isothermal, while the thermodynamic properties of the fuel are assumed constant. However, as the pressure increases within the injector, significant changes to fuel physical properties are realised, which are critical in the formation of cavitation [167] and affect combustion and emissions [236]. With regards to liquid density variation, a barotropic evolution of the liquid density as function of pressure is frequently utilised [122]. A barotropic equation has been derived in past studies following Kolev's Diesel properties collection [237] or single component surrogates using the NIST Refprop [238] database. Such simplifications may lead to deviations in the discharge coefficient and fuel heating predictions with respect to the real fuel, particularly in cases of high-pressure injections [4]. For the vapor phase, the usual assumption adopted is the ideal gas law behaviour. Real Diesel fuels are typically composed of hundreds of com- ponents, which cannot be addressed using constant properties or a simplified equation of state (EoS). Composition effects in Diesel fuel are related to changes in the spray atomisation [239] and spray tip penetration [240], but the cavitation of each component in the multicomponent fluid during injection has not been addressed. There is only one related study in which the effect of non-condensable gas on cavitation of a single component fuel during injection is analysed [93], modelled with a cubic EoS. Experiments of Diesel and biodiesel fuel mixtures have shown that the biodiesel content slows down cavitation due to its higher molar weight [241], which was also seen numerically at extreme temperatures [242]. Still, most studies regarding preferential cavitation and transport based on the solution of the full Navier-Stokes equations are based on models for fuel droplets in a gaseous environment [243–245]. In an effort to simulate in a more accurate way the effect of fuel property variation at different conditions for multi-component fuels, the PC-SAFT equation of state [189] can be used. This is a theoretically derived model, based on the perturbation theory [246–249], that requires only three molecular-based parameters per component for fluid property calculations. There are several advantages in using the PC-SAFT compared to a cubic equation of state for calculating fluid properties. The PC-SAFT predicts derivative properties (such as the speed of sound) with satisfactory accuracy, reducing errors by a factor of up to eight [250,251], as compared to predictions with a cubic equation of state (such as the Peng-Robinson [252] or Soave-Redlich-Kwong [253]). Density predictions with the PC-SAFT exhibit six times lower error for a widely used surrogate such as dodecane [254] and half the error of those made with improved cubic equations, such as volume-translated versions [255]. The PC- SAFT provides satisfactory agreement between calculated and experimental properties of reservoir fluids [256] and natural gas [257] . The aim of the current work is to investigate the in-nozzle flow and cavitation forming in heavy-duty Diesel injector at injection pressures up to 450MPa, using a realistic multicomponent Diesel surrogate. This surrogate is a mixture of eight components based on the composition of a grade no. 2-D S15 Diesel emissions certification fuel from Chevron-Phillips Chemical Co. [195], already modelled by the authors using the PC-SAFT [181]. The surrogate mass composition is listed in Table 5. 1. Two different methodologies have been utilised: one neglecting the thermal effects and one where the energy equation is solved considering thermal effects due to wall-induced friction and fuel depressurisation. To the best of the author's knowledge, this is the first study in the literature where the PC-SAFT is utilised in nozzle flow simulations addressing the preferential cavitation of the fuel components and their evolution at extreme injection pressures. Following the above brief introduction, the next section gives the outline of the case set-up, the geometry and CFD model used for the simulations. The results are shown including the internal flow, the effects on temperature due to friction and the preferential vaporisation of the components within the multicomponent mixture. Lastly, the final section gives a summary and critique of the findings.

Compound Name	$M_w\ [g/mol]$	$T_b[K]$	$z_i[\%\ mass]$	$m_i[-]$	$\sigma[\text{Å}]$	$\epsilon/k_B[K]$
n-octadecane	254.5	590.0	27.3082	7.438	3.948	254.90
n-hexadecane	226.4	560.0	3.2477	6.669	3.944	253.59
heptamethylnonane	226.4	520.0	35.1237	5.603	4.164	266.46
1-methylnaphthalene	142.2	518.0	10.8772	3.422	3.901	337.14
n-butylcyclohexane	140.3	456.2	10.8149	3.682	4.036	282.41
trans-decalin	138.2	460.5	4.0392	3.291	4.067	307.98
tetralin	132.2	480.9	3.8009	3.088	3.996	337.46
1,2,4-trimethylbenzene	120.2	442.6	4.7883	3.610	3.749	284.25

Table 5. 1. Mass composition for the Diesel surrogate modelled on this work. Boiling points at 0.1 MPa taken from the literature.

5.2 Numerical Method

5.2.1 CFD model

The in-house density-based CFD codes used in this work solves the compressible Navier-Stokes equations utilizing the open-access OpenFOAM [258] platform. The two-phase flow is assumed to be a homogeneous mixture of vapor and liquid in mechanical equilibrium, i.e. both phases share the same pressure and velocity fields. This implies that as there is only one fluid in the entire domain, the discharge is on liquid; this configuration resembles that of injector test benches, where fuel is squirted for thousands of hours into a liquid-filled collector. The barotropic behaviour of the fluid does not consider the energy conservation equation. The second thermodynamic closure solves for both the Navier-Stokes system and the energy conservation equation. Both solvers share a system which consists of the continuity equation:

$$\frac{\partial}{\partial t}\int_V \rho dV + \int_A (\rho u) \cdot ndA = 0 \tag{1}$$

Where ρ is the mixture density and $\boldsymbol{u}$ the velocity vector field, and the momentum equations:

$$\frac{\partial}{\partial t}\int_V \rho u dV + \int_A (\rho u \otimes u) \cdot ndA = -\int_A pndA + \int_A \tau \cdot ndA \tag{2}$$

where p is the pressure and $\boldsymbol{\tau}$ is the stress tensor defined as $\boldsymbol{\tau} = \mu_{eff}[\nabla \boldsymbol{u} + (\nabla \boldsymbol{u})^T]$, with μ_{eff} defined as the sum of laminar, μ given by the thermodynamic table, and turbulent, μ_T, dynamic viscosities. Regarding the turbulence model, a Large Eddy Simulation (LES) model is used [162,259]. In particular, the turbulent viscosity is modelled using the Wall Adaptive Large Eddy (WALE) model [260], by the equation:

$$\mu_t = \rho {L_s}^2 \frac{\left({S_{ij}}^d {S_{ij}}^d\right)^{3/2}}{\left(S_{ij} S_{ij}\right)^{5/4} + \left({S_{ij}}^d {S_{ij}}^d\right)^{5/4}} \tag{3}$$

where S_{ij} is the rate of strain tensor and S_{ij}^d is the traceless symmetric part of the square of the strain of the velocity gradient tensor, i.e.:

$$S_{ij}{}^{d} = \frac{1}{2}\left(g_{ij}{}^{2} + g_{ji}{}^{2}\right) - \frac{1}{3}\delta_{ij}g_{kk}{}^{2} \tag{4}$$

With, = $\partial u_i / \partial x_j$ and δ_{ij} the Kronecker delta. The length scale, L_s , is based on the filter size and the cell to wall distance, d_{wall} , as follows:

$$\mathrm{L} = min\{\kappa\, d_{wall}, C_w\, V^{1/3}) \tag{5}$$

where the used model constants are: κ the von Karman constant, 0.41, and C_w = 0.325. The energy conservation equation is also solved:

$$\frac{\partial}{\partial t}\int_V \rho E dV + \int_A (u\rho E)\cdot ndA = -\int_A pu\cdot ndA + \int_A (k_T \nabla T)\cdot ndA + \int_A (\tau\cdot\nabla u)\cdot ndA \tag{6}$$

where E is the specific total energy of the system, defined as internal energy plus the kinetic energy, i.e. $E = h - p/\rho + |\,\boldsymbol{u}\,|^2/2$ where h is the enthalpy, and k_T the thermal conductivity of the fluid given by the thermodynamic tables.

5.2.1.1 Hybrid flux model

Two-phase flows are characterised, among others, by large variations in the speed of sound. While the speed of sound in the liquid phase is of the order of O (10^3) m/s and that of gas is O (10^2) m/s, in the liquid-vapor mixture it drops down to O(1)m/s. Therefore, for a typical velocity at the orifice of O (10^2) m/s, it can be expected a range in the Mach number from O (10^{-1}) to O (10^2) m/s. For density-based solvers, low Mach numbers are causing convergence problems and dispersion, so a hybrid flux is used for accounting for both low and high Mach numbers. That, in terms of the inter- face pressure within the approximated Riemann solver scheme is:

$$p = [1-\beta(M)]p^{inc} + \beta(M)p^{comp} \tag{7}$$

Where

$$p^{inc} = \frac{C^L p^R + C^R p^L}{C^L + C^R} \tag{8}$$

$$p^{comp} = \frac{C^L p^R + C^R p^L + C^R C^L (u^L - u^R)}{C^L + C^R} \tag{9}$$

where $C = \rho c$ is the acoustic impedance, u is the interface velocity, L and R refer to the left and right side of the interface and:

$$\beta(M) = 1 - e^{-aM} \tag{10}$$

where a is a blending coefficient, set to 1.5. Thus $\beta(M) \to 0$ when $M \to 0$, and therefore $p = p^{inc}$. On the other hand, $\beta(M) \to 1$ when $M \to \infty$, and therefore $p = p^{comp}$.

5.2.2 Injector geometry and operating conditions

The examined injector geometry was based on a common rail 5-hole tip injector with tapered holes. The most important dimensions for this injector are shown in Table 5. 2 . The nominal mass flow rate at a reference condition of P_{inj} = 180MPa has been also included. Although the simulation is transient, the needle valve was assumed to be still at its full lift of 350μm during the main injection stage. The simulated geometry considers only one fifth of the full injector geometry, as shown in Figure 5. 1, imposing symmetric boundary conditions on the symmetry planes. A hemispherical volume is attached to the nozzle exit; this volume is added in order to be able to capture the cavitation cloud inside the nozzle and avoid interference with the outlet boundary. Characteristic volumes of the injector geometry are also pointed out by colour in Figure 5. 1 (a); the walls are assumed to be adiabatic. Constant pressure boundary conditions of 60, 120, 180, 250, 350 and 450MPa at the inlet and 5MPa at the outlet have been considered. The temperature at the inlet boundary is fixed and corresponds to that of an isentropic expansion from the reference point set at 5MPa and 324K, shown in Table 5. 3. This reference temperature is chosen based on the theoretical outlet temperature for operation at a reference injection pressure of 180MPa and a discharge coefficient of unity, i.e. the ideal case without pressure losses, as calculated in [111] using the same geometry. The temperature at the outlet of the domain is calculated by the solver. Also, in Table 5. 3 the calculated mean exit velocity, speed of sound on the liquid, Mach number and discharge coefficient for each injection pressure are indicated. Regarding the computational mesh, two topologies have been used.

1

Geometrical characteristics		
Needle radius at inlet (mm)		1.711
Inlet orifice rounding (mm)		0.05
Orifice length (mm)		1.262
Orifice diameter (mm)	Entrance D_{in}	0.37
	Exit D_{out}	0.359
Sac volume (mm^3)		1.19
k-factor = (D_{in} - D_{out}), D in µm		1.1
Nominal mass flow rate at P_{inj} =180MPa (g/s)		41.32

Table 5.2**.** Dimension of the injector used for the simulations on this work and nominal flow rate at the reference condition of P_{inj} =180MPa.

2

$\boldsymbol{P_{inj}[MPa]}$	$\boldsymbol{T_{inlet}}$ **[K]**	$\boldsymbol{U_{exit}}$ **[m/s]**	$\boldsymbol{c_{liquid}[m/s]}$	$\boldsymbol{M_{liquid}[-]}$	$\boldsymbol{C_d}$
60	332	332.39	1128	0.2946	0.842
120	340	461.02	1066	0.4324	0.819
180	345	564.69	1057	0.5342	0.813
250	350	664.77	1045	0.6361	0.812
350	359	781.67	1012	0.7724	0.807
450	365	881.74	1001	0.8808	0.804

Table 5.3**.** For each injection pressure, inlet temperatures, mean exit velocity, speed of sound on the liquid, Mach number and discharge coefficient. Results come from simulations with thermal effects being considered.

3

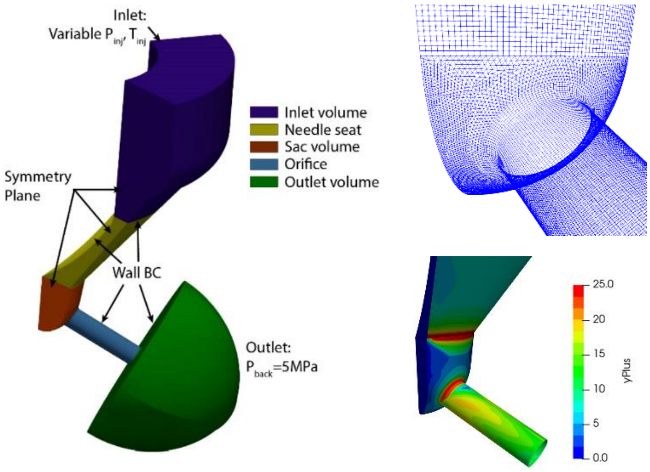

Figure 5. 1 Simulated geometry (one fifth of the complete injector nozzle). Characteristic volumes are colourised and the boundary conditions are indicated. The transition between the two distinct topologies at the orifice and the contour plot at P_{inj}=450MPa for the estimated y+ values are also added.

As shown in Figure 5. 1 (b), upstream of the orifice entrance, i.e. inside the nozzle's sac volume, an unstructured tetrahedral mesh is utilised. For the rest of the computational domain, a hexahedral block-structured mesh is used. Given the flow conditions inside the injector nozzles, the Reynolds number at the orifice, where cavitation develops, varies significantly between the cases. For 60MPa, it is ~35000, for 180MPa is ~60000 and ~90000 for 450MPa. This corresponds to Taylor length scales, λ_g :

$$\lambda_g = \sqrt{10}Re^{-0.5}D \in (4\mu m, 6.5\mu m) \quad (11)$$

Where D is an indicative length of the geometry; in this case the nozzle hole exit diameter. The resolution in the core of the orifice is ~5 μm , with refinement near the walls down to a minimum cell size of ~2 μm . As also shown in Figure 5. 1 (c), for the most re- strictive case of 450MPa, the maximum y+ was 25. Due to the unfeasible computational effort a domain with a smaller cell size would entail, the near wall flow was treated with two wall functions: (i) kqRWallFunction [261] for the turbulent kinetic energy and (ii) nutkwallfunction for the turbulent viscosity. The timestep was adapted to a fixed acoustic Courant number of 0.5, thus the timestep varied from 8ps for the 450MPa case to 100ps for the 60MPa case. Table 5. 4 shows integral quantities of engineering interest, such as the overall mass and energy balance for each injection pressure, with thermal effects being considered. The last column in Table 5. 4 shows the difference found in the mass flow rate at the exit for the most refined mesh, decreasing the smallest cell size to 1.06μm and, therefore, increasing the number of cells to 11M. No significant differences were found and therefore the 1.5M cells mesh was used for all following simulations.

	Mass flow rate $[g/s]$		**Energy flow rate** $[kJ/s]$		**%change in** $\dot{m}_{out}$ **after refinement**
$P_{inj}[MPa]$	$\boldsymbol{Inlet}$	$\boldsymbol{Outlet}$	$\boldsymbol{Inlet}$	$\boldsymbol{Outlet}$	
60	24.37	24.53	31.97	32.19	-
120	33.89	34.16	42.08	42.43	-
180	41.32	41.72	48.19	48.67	0.0528
250	49.06	49.38	53.91	54.28	0.0785
350	58.09	58.38	57.74	58.11	0.1169
450	66.31	66.59	59.17	59.44	0.1542

Table 5. 4**.** Time-averaged mass and energy flow rates at the inlet and outlet for all cases, with thermal effects being considered. The last column shows the percentage change in mass flow rate at the outlet after a refinement from 1.5M to 11M cells for cases 180MPa to 450MPa, decreasing thus minimum cell size from 2.12μm to 1.06μm.

5.2.3 Thermodynamic properties

As already mentioned, the thermodynamic properties of the Diesel surrogate are modelled using the PC-SAFT EoS [189] for a density range of 0.001-1100kg/m3 and an internal energy range of -1.40779-4.7529MJ/kg in a tabulated format. The pure-component and ideal gas parameters can be found in the Tables A.1 and A.2 of the Appendix 3. The range in internal energy corresponds to temperatures in range of 280-2000K. These limits allow the correct characterisation of the vaporised and compressed fuel alike while also capturing the increased temperatures due to friction-induced heating. The structure of the table consists of 1000×1000 elements separated by constant intervals of the decimal logarithm (log10) of the density and internal energy. The properties are calculated every 0.006047 log10(kg/m^3) and 6.16696kJ/kg. For the barotropic approach, the properties were calculated maintaining the entropy of the fluid constant to that obtained at 324K and the imposed outlet pressure of 5MPa. Figure 5. 2 shows the properties that govern the behaviour of the Diesel surrogate with respect to pressure following different isentropic curves, depending on the assumed reference temperature. While the black line refers to the one used in the barotropic approach, the other two refer to reference temperatures of: (i) 384K that is the maximum temperature reached in the liquid-vapor equilibrium phase for P_{inj} = 180MPa considering thermal effects, and (ii) 484K that is the maximum temperature reached in the liquid-vapor equilibrium regime for P_{inj} = 450MPa when thermal effects were considered. As shown in Figure 5. 2, at higher temperatures the values for density, viscosity and thermal conductivity decrease, while increasing the heat conductivity. Regarding density, an exponential-like increase can be seen in the liquid phase converging at very high pressures for the distinct reference temperatures. It can also be seen a sudden increase in density at the saturation pressure, as the phase change is almost isobaric. Moreover, this saturation pressure changes significantly for the different cases, increasing with the reference temperature. This increase can be explained by the temperatures observed in Figure 5. 2 (b). For a higher temperature, the easier it is for the substance to evaporate and therefore its vapor pressure is enhanced. The change in temperature from vapor to liquid is seen smoother than for density. The vapor volume fraction shown in Figure 5. 2 (c) highlights that the phase change is al- most isobaric at bubble point, i.e. at low vapor volume fraction, while needing an additional pressure drop to complete the vaporisation. The dynamic viscosity, shown in Figure 5. 2 (d), shows how dependent it is on pressure, while it is inversely proportional with temperature. Figure 5. 2 (e) shows how significantly smaller the thermal conductivity is in the vapor phase compared to that of the liquid phase (of the order of O(100)), which will contribute to the vapor heating up more rapidly than the liquid. Similarly, another factor that will contribute to a faster heating up of the vapor is the heat capacity, shown in Figure 5. 2 (f), due to its lower values compared to those of the liquid phase. The calculation of the vapor volume fraction αv is determined by minimizing the Helmholtz Free Energy, according to the algorithm recently presented by the authors in [262], consisting on a stability analysis followed by a phase equilibrium calculation in case the mixture is found unstable. For the conditions studied in these isentropic simulations, the vapor pressure for the isentropic Diesel fuel is predicted to be 230Pa. For the case where the complete thermodynamic range is resolved, the saturation pressure is not fixed and will depend as well on the internal energy. The speed of sound c is calculated for a single phase directly from its definition:

$$c = \sqrt{\left(\frac{\partial p}{\partial \rho}\right)_s} \tag{12}$$

Where the subscript *s* indicates that the derivative is computed at constant entropy. When the fluid is in the two-phase region, the speed of sound follows the Wallis' rule [263] :

$$\frac{1}{\rho c^2} = \frac{\alpha_v}{\rho_v c_v^2} + \frac{1-\alpha_v}{\rho_l c_l^2} \tag{13}$$

where the subscripts *v* and stand for vapor and liquid phase. The dynamic viscosity, μ, is calculated by using an entropy scaling method [191], while the mixing rule is taken from the author's previous work [262]. The parameters used for the calculation of viscosity are found in Table A.3 of the Appendix 3. In the case of the two-phase region, the homogeneous viscosity is calculated with

$$\mu = (1-\alpha_v)\left(1+\frac{5}{2}\right)\mu_l + \alpha_v \mu_v \tag{14}$$

Regarding the thermal conductivity, it is also calculated using the entropy scaling method [264]. The parameters used for its calculation can be also found in the Appendix 3, on Table A.4. A simple weighted mixing rule with the vapor volume fraction is used:

$$k_T = (1-\alpha_v)\, k_{T,l} + \alpha_v\, k_{T,v} \tag{15}$$

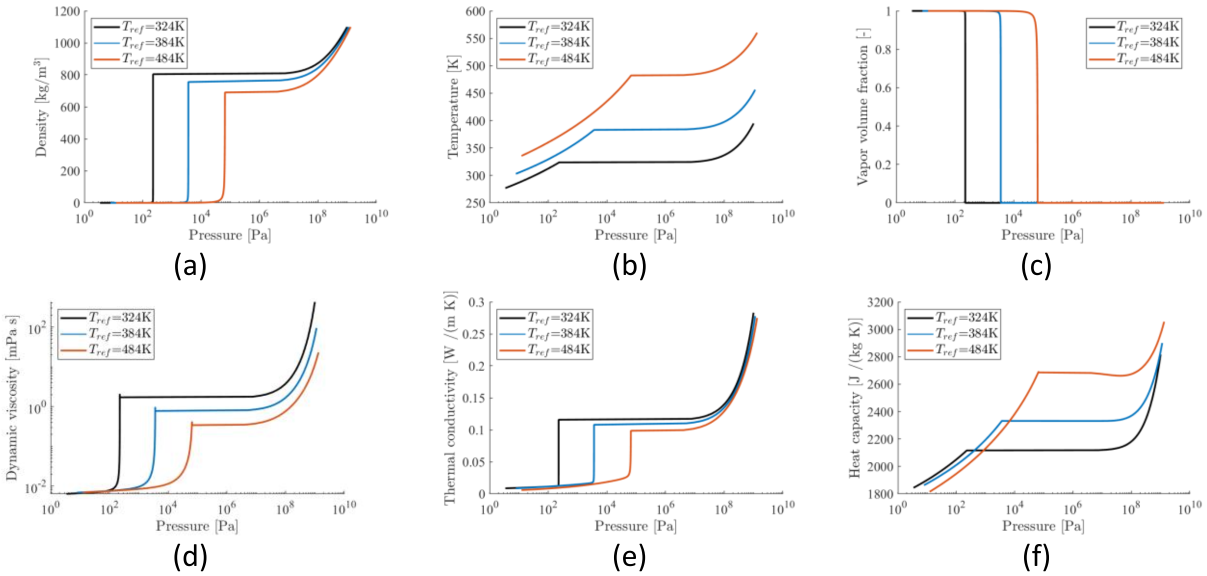

Figure 5. 2**.** Thermodynamic data following an isentropic expansion of the Diesel surrogate. Three cases are shown depending on the reference temperature at 5MPa: (i) 324K for the

barotropic method used in this work, (ii) 384K as the maximum temperature reached in the liquid-vapor equilibrium phase for P_{inj}=180MPa considering thermal effects, and (iii) 484K as the maximum temperature reached in the liquid-vapor equilibrium phase for P_{inj}=450MPa considering thermal effects.

5.2.4 Limitations, link to previous works and present contribution

Limitations arising from both the validity of the models them- selves utilised and the selection of the specific conditions investigated, include: (1) the lack of detailed validation against experimental data for the extreme pressure values tests; (2) the dependency/accuracy of the simulations on the equations describing the fuel properties as function of pressure and temperature; (3) the assumption of local mechanical and thermal equilibrium, i.e. vapor and liquid have, locally, the same velocity (no slip) and same temperature, utilised in order to predict the amount of fuel that cavitates; and (4) the omission of transient effects ought to the movement of the injector's needle valve as well as the dependency of the obtained results on the specific geometry investigated here. A short evaluation of those factors is provided below before the presentation of the results obtained.

(1) With regards to the lack of experimental validation for the conditions tested, several comments and reference to prior studies can be made. For injection pressures up to 500MPa only spray formation results have been reported [130], but without information about the in-nozzle flow. As stated in the introduction, cavitation measurements in real-size injectors operating pressures beyond 200MPa [199] has not been possible up to now, due to transparent material constrains. Even for lower pressure conditions, only qualitative images have been obtained but not quantitative data for the cavitation volume fraction or the velocity field. Nevertheless, validation works have been thoroughly reported at lower injection pressures utilising similar models to those reported here. More specifically, homogeneous mixture models (either barotropic or mass transfer) have been found to have very similar performance [162,259] in the limit of large mass transfer rates of the former. Also, such models have been validated for predicting the 3D distribution of vapor fraction within the validation uncertainty (±7%, including both numerical and experimental uncertainties). Further validation has been obtained for the

flow field distribution, cavitation shedding frequency and turbulent velocities in the same single-hole injector against high energy X-ray phase contrast imaging (XPCI) measurements for conditions covering a range of cavitation regimes (incipient, fully developed and vortex/string cavitation) [159,198]. Additionally, validation against Laser Doppler Velocimetry (LDV) measurements have been also reported in [162,163] utilising the WALE LES model for turbulence, suggest that it can reproduce the turbulent structures found in Diesel nozzles. These studies suggest that the model can capture both incipient and developed cavitation features. In the present study, the Reynolds number is ~ [35000 - 90000] and thus, it is within the range of applicability of the selected model. As the vaporous core of cavitating vortices has been found to be in the order of 20 μm [265], the smallest cell size of ~2 μm used suggests that there are no under resolved vortical structures that may cavitate and significantly in- fluence the obtained results. For injection pressures in the range of 180MPa, the same simulated injector geometry was previously validated for predicting cavitation erosion damage [111] utilising the barotropic model. Cavitation erosion predictions have been also validated recently against measurements in a fuel pump [142]. These studies give confidence that the barotropic model is performing relatively well for similar cases as those studied here. Turning to thermal effects, there are no experiments available that can be used for validation. The earlier studies [169,170,172,266] from the authors performed also under both fixed needle valve conditions and including the movement of the injector's needle valve [267] have been compared results against 0-D predictions of the mean fuel heating up as it discharges through the fuel injector up to 300MPa, with very good accuracy [4,10].

(2) A critical question relative to this study is related to the dependency/accuracy of the simulations on the

equations describing the fuel properties as function of pressure and temperature. As mentioned, the simulations carried out have utilised properties derived by the PC-SAFT EoS. This EoS has been previously used with the Diesel surrogate of this work and compared with experimental results up to 500MPa and 600K for density, viscosity and volatility [181] with an accuracy of 1.7% for density, 2.9% in volatility and 8.3% in viscosity. Diesel fuels with different compositions have been also modelled at pressures up to 300MPa and temperatures up to 532K [179] and the obtained accuracy against those measurements was ~2% for density and ~10% for viscosity.

Other Diesel properties, such as thermal conductivity, at extreme conditions up to 450MPa and 360K can also be found accurately predicted by PC- SAFT [175,176] with an accuracy of 3%. It can thus be claimed that the selected EoS is a good compromise for studying such effects in high pressure injectors.

(3) One of the main assumptions in the described methodology is the mechanical and thermodynamic equilibrium between the liquid and the vapor phases. With regards to the mechanical equilibrium assumption, the recent study from the authors using a two-fluid model has confirmed that differences between liquid and vapor velocities are less than 10% and only in localised locations of the flow [168,268]; they have been found not to affect the overall growth rate and production of vapor. The assumption of thermodynamic equilibrium is more significant. A metastable, i.e. non-thermodynamic equilibrium, state occurs when the pressure of the liquid drops below the saturation pressure and no vapor is formed due to the rapid expansion of the liquid [196,197]. In the literature, non-thermodynamic equilibrium models, such as the well-known mass transfer models of Schnerr and Sauer [33] , Singhal et al. [34] and Zwart et al. [77] are used. Predictions utilising such mass transfer models tend towards equilibrium by increasing the evaporation/condensation coefficients [97,269]. Apart from mass transfer models, in the literature there are models relying on the solution of the full Rayleigh-Plesset equation, commonly done in a Lagrangian reference frame, thus incorporating second order effects and the influence of surface tension. However, such models inherently assume a spherical bubble shape, the interaction be- tween bubbles (break-up, coalescence) is not easy to describe and the coupling with the continuous phase (liquid) is difficult in areas of large void fractions [36,109,150,270,271]. The relaxation time of the tensile stresses, i.e. those acting in the metastable state, was numerically estimated to be of the order of 10ns in a flow configuration where a vertical tube filled with liquid was impacted vertically, leading to an expansion wave of 30MPa [272]. However, the nuclei concentration used in this study was infinitesimally small, which is not applicable to real systems and thus its result is a significant over- prediction. Nevertheless, it is possible to use this time-scale to estimate that, as the residence time of the fluid in the injection hole has a minimum value of the order of 1μs, that for the 450MPa case, the time to reach equilibrium would be, at least, 100 times faster.

(4) Finally, the present work omits transient effects related to the motion of the needle valve [273], while it refers to only one injector geometry utilised with heavy-duty diesel engines featuring hole tapering. It has been reported in the literature that cavitation reduces the mixing uniformity within circular, sharp-edged orifices [274] while tapered nozzles reduce its appearance [14]. Thus, although the studied geometry is representative for such application, it can be expected that different cavitation volume fraction will be developing for other nozzle geometries. With regards to the needle valve motion, it is well documented in the literature that depending on the nozzle geometry and needle valve position, cavitation may appear to the bottom part of the injection hole as well as the needle seat area and inside the nozzle's sac volume at low needle lifts [44,158,275]. More recent studies have shown that the initial air/liquid distribution inside the nozzle volume prior to the start of injection are also complex, with large air bubbles been present [155,156,158,275]; these are formed during the needle valve closure that induces back flow to the injector. However, such effects and flow regimes are not realised when the needle valve is at its nominal full lift position. At the same time, the needle remains still for a relatively large duration, typically more than 10times longer compared to the opening/closing time. Transient effects although important for cavitation erosion [140], nozzle wall wetting and formation of non-well atomised liquid fragments that can affect emissions are out of scope of the present work.

Despite those limitations, the present work aims to make the following contributions: To the best of the author's knowledge, this is the first study in the literature where the PC-SAFT is utilised in nozzle flow simulations addressing the preferential cavitation of the fuel components and their evolution at injection pressures up to 450MPa. For this, an 8-component Diesel surrogate [195] is modelled using the PC-SAFT EoS, considering the effects of variable thermal conductivity, heat capacity and viscosity due to extreme pressurisation. The authors also take advantage of PC-SAFT to calculate the individual vaporisation of each component within the vapor cloud during cavitation, as each component vaporises at a distinct rhythm, different to that of the mixture and to that of the other components.

5.3 Results

In this section, the results obtained for the range of injection pressures from 60MPa and up to 450MPa are presented. If not stated otherwise, all results consider thermal effects. Firstly, the in- ternal flow through the injector is inspected. Secondly, the changes in temperature and vapor pressure are investigated and compared with the case where thermal effects are neglected. Thirdly, the formation of cavitation inside the nozzle orifice is analysed. Lastly, due to the multicomponent nature of the fuel, the preferential cavitation of its components is examined.

5.3.1 Flow field

Figures 5.3 through 5.5 show predictions of three time-averaged (i) magnitude of the vorticity on a logarithmic scale, (ii) density and (ii) viscosity at three injection pressures; results are presented in two sets of slices: one longitudinal to the injector geometry and four transversals to the nozzle hole. Thin solid black lines are added for clarity; all plots on each Figure 5. share the same colour scale. On Figure 5. 3, vorticity indicates locations where thermal effects become significant due to shearing. Lower values, of the order of 10^5/s or smaller, are seen in the core of the flow as it travels through the sac volume as well as into the orifice. Close to the walls, vorticity is generated reaching values up to 10^8/s, due to the large shear induced from the no-slip wall velocity boundary condition. High values of ~10^7/s are also found on a relatively wide region located on the top half of the orifice volume, where separation of the flow occurs, and cavitation is forming. Density and viscosity show similar behaviour throughout the injector. In- side the nozzle's sac volume, as seen on Figure 5. 4, densities take values from 845 kg/m^3 for injection pressure of 60MPa, 900.342 kg/m ^{3} for 180MPa and up to 982.345 kg/m ^{3} for 450MPa. This density decreases as the fuel expands through the orifice down to ~720kg/m^3 at the exit of the orifice where the pressure is set to 50MPa. As the flow separates at the entrance of the injector orifice and the fuel cavitates, densities decrease locally 3 orders of magnitude, to ~10^{-3} kg/m^3, inducing strong density gradients. It can be also clearly seen that as injection pressure increases, the extend of low-density values for the valour-liquid mixture is significantly reduced, due to the gradual condensation of vapor caused by the increased pressures present inside the injection hole. The iso-surface of 50% vapor volume fraction is also depicted, showing for the 180 and 450MPa cases two coherent structures separated at the symmetry midplane; thorough discussion of the cavitation formation and development will be given in the following subsections. Regarding viscosity, on Figure 5. 5, the increase with injection pressure in the nozzle's sac volume is significantly higher than that for density. At 60MPa, the viscosity of the fuel is 2.66mPa •s, doubling to 5.2mPa •s at 180MPa and then quadrupling up to 19.64mPa •s at 450MPa. Average values at the nozzle exit are ~1.3mPa •s. Minimum values of 7 •10^{-3} mPa •s are found again at the entrance of the orifice where the flow separates. Figure 5. 6 shows the mass flow rate as function of the pressure drop for all cases, comparing the barotropic approach with that considering thermal effects.

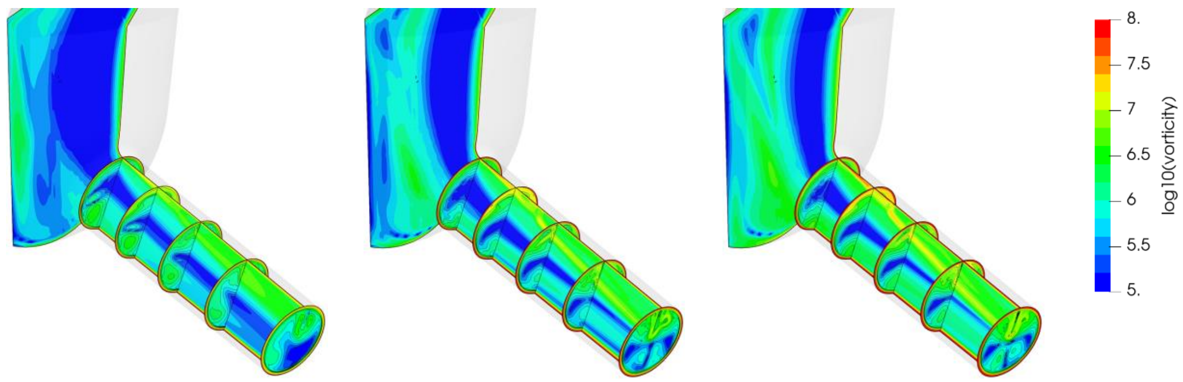

(a) 60MPa (b) 180MPa (c) 450MPa

Figure 5. 3**.** Predicted time-averaged vorticity, in logarithmic scale, on different slices at the sac volume and orifice for three injection pressures. Thermal effects are considered.

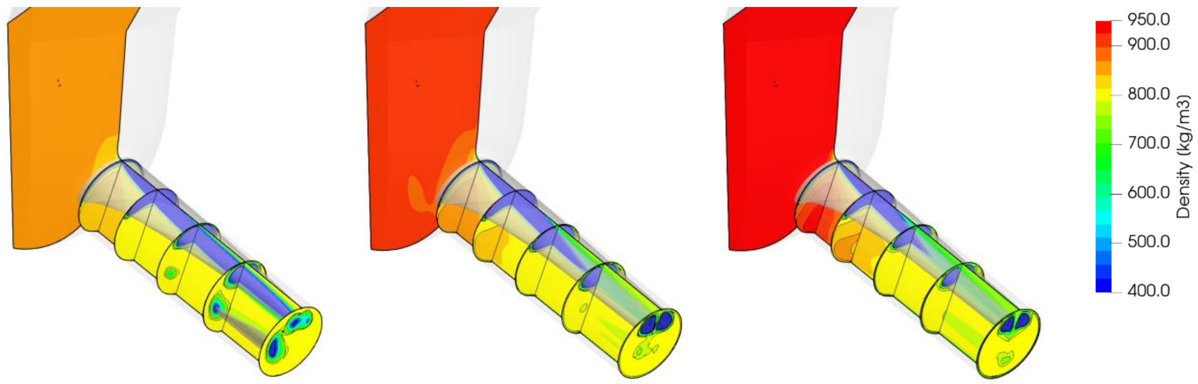

(a) 60MPa (b) 180MPa (c) 450MPa

Figure 5. 4**.** Predicted time-averaged density on different slices at the sac volume and orifice for three injection pressures. Thermal effects are considered. The iso-surface for vapor volume fraction of 50% is included, which shows two coherent structures separated at the midplane for (b) and (c).

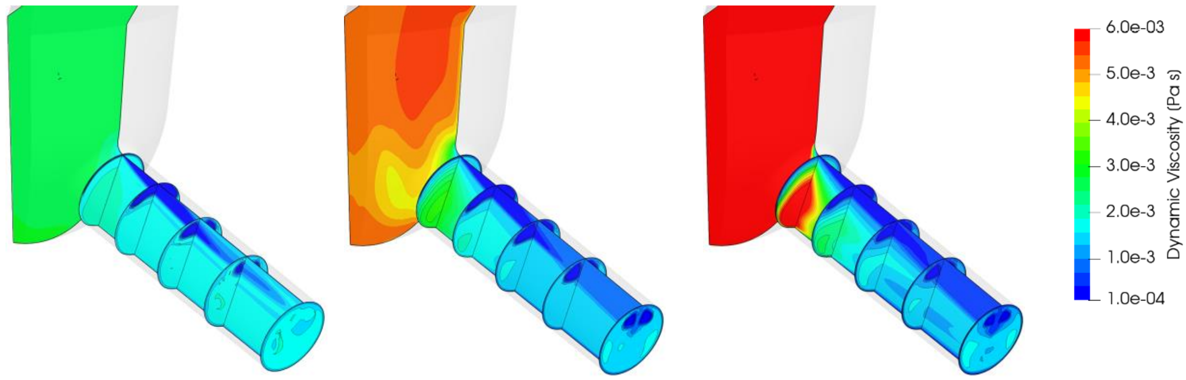

(a) 60MPa (b) 180MPa (c) 450MPa

Figure 5. 5. Predicted time-averaged dynamic viscosity on different slices at the sac volume and orifice for three injection pressures. Thermal effects are considered.

As expected, the mass flow rate increases linearly with the square root of the difference between the injection and back pressure. This shows that in neither of the two approaches the flow gets chocked with increasing injection pressure. Moreover, the values for the thermal and the barotropic cases are found to be very close. Due to the temperature increase, the density of the fluid drops for the thermal case, but so does the viscosity, enhancing the velocity of the flow. For instance, at 180MPa the density of the thermal case is 2.9% smaller than that for the barotropic case, while the velocities are 2.1% greater, while at 450MPa these differences are 2.1% and 1.63%, respectively. As a result, these two effects offset each other, and the predicted mass flow rate does not vary significantly between the two cases considered.

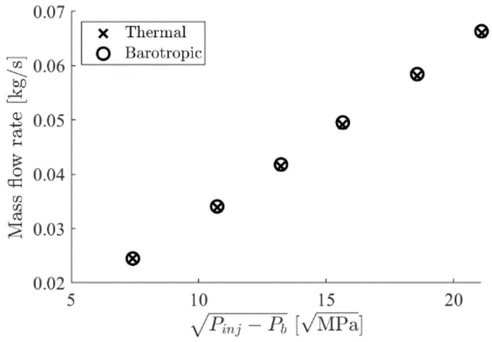

Figure 5. 6**.** Mass flow rate at the orifice exit for both the barotropic and thermal cases.

5.3.2 Changes in temperature and vapor pressure due to thermal effects induced by wall friction and depressurisation

Figure 5. 7 shows the relative temperature change with respect to the injection temperature, defined as:

$$\frac{T - T_{inj}}{T_{inj}} * 100 \qquad (16)$$

Results are shown for the 60MPa, 180MPa and 450MPa cases, for which the injection temperature is indicated in Table 5. 3. A solid line in the longitudinal slice shows where $T = T_{inj}$; thus, all points inside this iso-line show cooling and those outside show heating. Several observations can be made. First, as the injection pressure increases, temperature gradients increase accordingly, i.e. both lower and higher relative temperatures are found. Liquid fuel is heated up due to friction with the walls, but its temperature gradually drops towards the centre of the orifice. However, in the locations of cavitation formation inside the orifice, heating dissipation is not observed due to the vapor's significantly lower thermal conductivity and heat capacity, in addition to the significantly lower velocities observed in this region. The highest temperatures are found close to the entrance to the injection hole where the fuel fully cavitates. With respect to the injection temperature, values in this region are found to be ~5% overall higher with a local peak of 50% higher for 60MPa case; at 180MPa, the fuels heats up ~10% with a local maximum of 70%; lastly, for the 450MPa case, the highest heating of 25% is estimated, reaching a 80% local maximum. On the other hand, cooling is also enhanced with injection pressure due to liquid expansion, as seen in the core of the flow. The cooling observed is 5%, 7.5% and 10% for 60MPa, 180MPa and 450MPa, respectively.

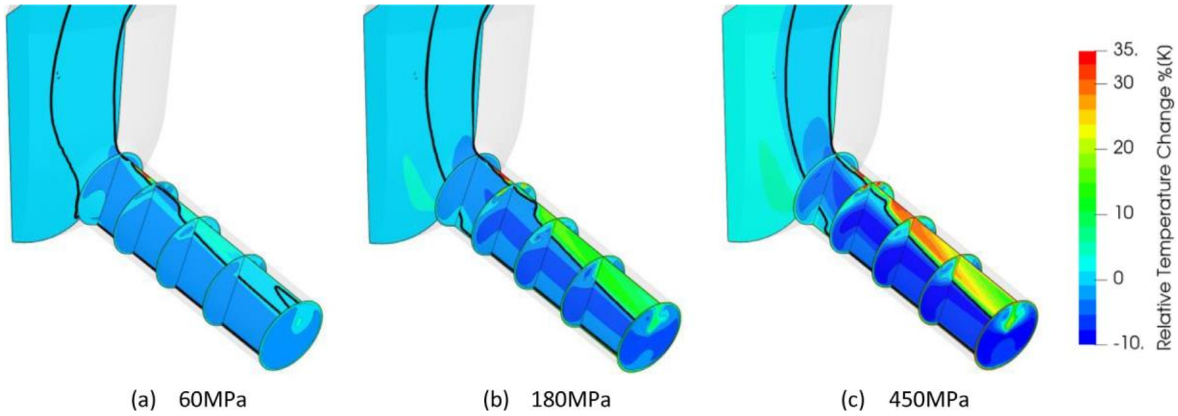

Figure 5.7. Predicted time-averaged temperature change with respect to the injection temperature, defined as $(T - T_{in\ j})/T_{in\ j} * 100$, when thermal effects are considered. The injection temperature for each case is shown in Table 3. A solid thick black line is plotted in the longitudinal slice where $T = T_{in\ j}$, thus all points inside this iso-line show cooling and those outside show heating. Results are shown on different slices at the sac volume and orifice for three injection pressures.

Figure 5. 8 (a) shows the temperature range for the liquid, vapor and vapor-liquid equilibrium (VLE) phases; the boiling and injection temperatures are added as a reference. The range on the vapor phase is significantly higher than that for the liquid phase. Maximum vapor temperatures take values of 510K, 570K and up to 640K for the 60MPa, 180MPa and 450MPa pressures, respectively. For the liquid phase, heating effects are more contained: at 60MPa the liquid fuel gets heated up to 360K, while for 180MPa it is 410K and 504K for 450MPa; the slope of temperature increase is around 28K per 100MPa. Regarding cooling, a rough correlation of a 7K of temperature decrease per 100MPa is calculated. Where the liquid and vapor coexist, the temperature range is lower than for the liquid phase. The temperatures found are 325-350K for 60 MPa, 335-400K for 180MPa and 355-485K for 450MPa, thus reaching a maximum temperature range of up to 130K. Figure 5. 8 (b) shows the average temperature at the orifice inlet and outlet slices. As observed, the temperature at both extremes of the orifice increase with the injection pressure, due to the enhancing of the friction- induced heating. The difference in temperature between these two zones also increase with the injection pressure. While the difference is of 2.3K at 60MPa, it is found to be 5.6K at 180MPa and 8.8K at 450MPa. Figure 5. 9 shows on the density-temperature thermodynamic diagram the distribution of predicted values in the whole computational domain; the saturation curve of the Diesel surrogate and the isentropic evolution used in the barotropic approach are also indicated. The colour of the plotted points helps

identifying their location within the computational domain, i.e. in the injector inlet upstream the needle seat passage, along the needle seat passage, sac volume and inside the injector hole. For all injection pressure cases investigated, it can be clearly seen that the process is not isothermal; as shown before, the range in temperatures increases with increasing injection pressure. The flow upstream of the nozzle hole (on the right of the saturation curve) shows a smaller range in temperatures than that through the orifice, mostly following the isentropic curve with the corresponding cooling effect due to the expansion of the liquid. There are points that diverge from this isentropic curve both in the needle seat and more clearly in the sac volume, due to thermal effects. This can be clearly seen in the plot for 450MPa: the flow in the sac volume splits into two legs, one corresponding to the core of the flow cooling down due to the liquid expansion and following the isentropic curve, while the other one its heated up because of wall friction. Another interesting result from the comparison between the barotropic approach and the consideration of thermal effects is shown in Figure 5. 10. This figure shows, for a single-time instance, both the isentropic curve, and the results corresponding to thermal effects being considered. The symbols are coloured according to the value of vapor volume fraction. In all cases, the liquid phase follows the isentropic curve reasonably well at high pressures (corresponding to zones before the orifice) while diverging from it as the pressure falls during the discharge of fuel through the nozzle hole. This divergence is significantly enhanced as the injection pressure increases and therefore thermal effects become more pronounced. The distribution of points become progressively wider and shifted to higher pressures, potentially driving towards greater pressure gradients where vapor is found. As the vapor phase distribution is shifted towards greater pressures, so does the vapor pressure, shown in Figure 5. 11 for all cases investigated; it increases with injection pressure to a substantial degree, diverging significantly from the barotropic assumption due to thermal effects. The minimum vapor pressure increases from 290Pa for 60MPa, to 523.5Pa at 180MPa and up to 1259Pa at 450MPa.

1

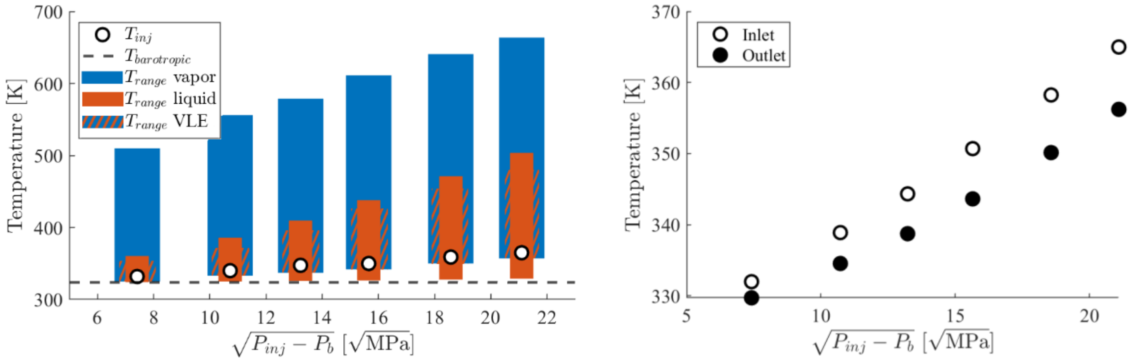

(a) (b)

Figure 5. 7**.** (a) Variation in temperature for the liquid, vapor and vapor-liquid equilibrium (VLE) phases versus the square root of pressure drop. As a reference, both the injection temperature and the reference temperature used in the barotropic approach are included. (b) Average temperatures at the orifice inlet and outlet slices.

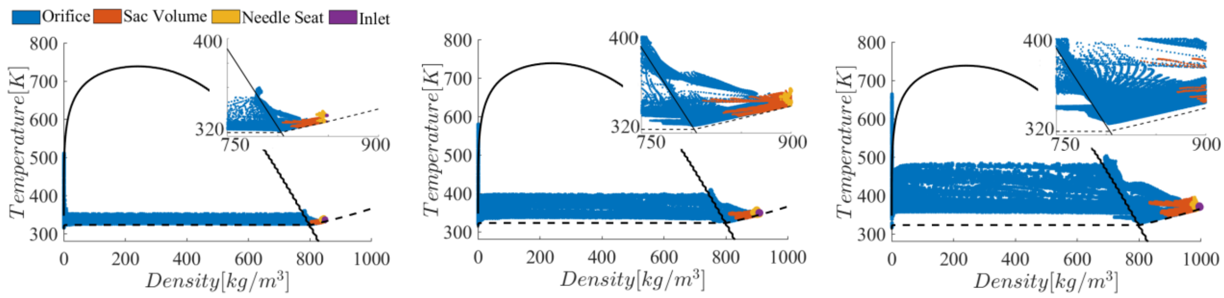

(a) 60MPa (b) 180MPa (c) 450MPa

Figure 5. 8. Predicted time-averaged density-temperature values over the whole computational domain for three injection pressures. The saturation curve for the multicomponent Diesel surrogate (solid line) and the isentropic approach (dashed line) are indicated. The colour of the symbols distinguishes the zone in the injector they correspond to. As an inset, the distribution of point close to the saturation curve is added.

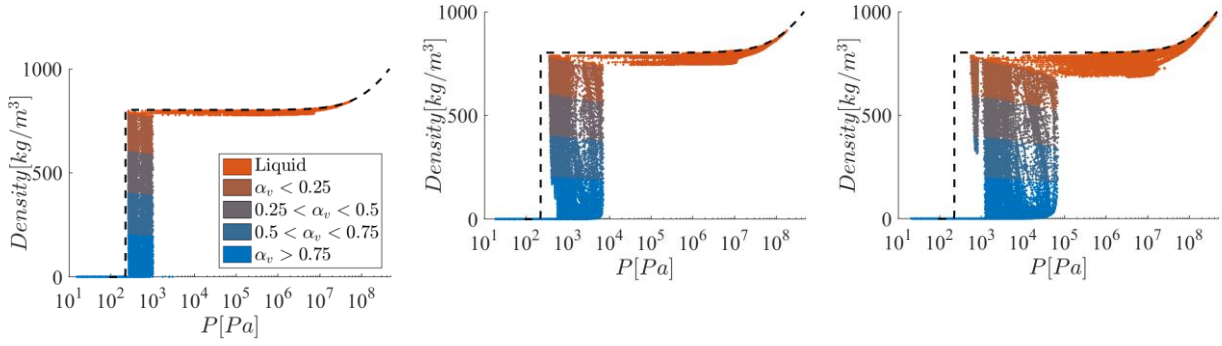

(a) 60MPa (b) 180MPa (c) 450MPa

Figure 5. 9**.** Predicted single-time instance of logarithm of pressure versus density values over the whole computational domain for three injection pressures; the curve for the barotropic evolution (dashed line) is indicated. The colour of the symbols shows their value of the vapor volume fraction within different ranges.

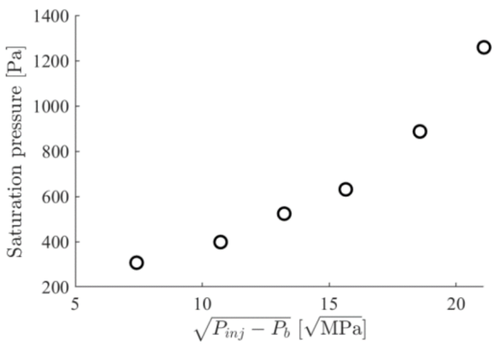

Figure 5. 10. Predicted saturation pressure versus the square root of the pressure difference when thermal effects are considered.

5.3.3 Changes in temperature and vapor pressure due to thermal effects induced by wall friction and depressurisation

Figure 5. 12 shows the time-averaged pressure distribution, in logarithmic scale, for three injection pressures on a longitudinal slice of the injector. The 50% vapor volume fraction iso-surface and the 5MPa iso-line, i.e. the back pressure value, are illustrated. As shown, the main difference between the cases is found inside the sac volume, where pressures take values of 55MPa, 162MPa and 405MPA for the 60MPa, 180MPa and 450MPa injection pressure cases, respectively. As the injection pressure increases, so does the pressure distribution inside the orifice, as indicated by the increased extent of the 5MPa iso-line within the orifice. Regarding

cavitation, the iso-surface of the vaporised fuel appears to reach just slightly the orifice exit for 60MPa and vortex cavitation is produced as a detached cloud. For 180MPa and 450MPa, cavitation completely reaches the orifice exit and no vortex cavitation is observed. Moreover, the cavitation cloud for 450MPa appears to be thinner than that the 180MPa case. These observations of the cavitating cloud are quantified in Figure 5. 13 (a), which shows the time-averaged vapor volume fraction inside the injector orifice versus the square root of the pressure drop. Results correspond to both the barotropic and thermal cases. As shown, the barotropic and complete formulation approaches follow similar trends. Due to the higher average temperatures and consequently higher vapor pressures found when considering thermal effects, cavitation growth is enhanced and thus found to be greater than in the barotropic approach. For both cases the volume of vapor formed inside the orifice first increases up to 120MPa and then decreases as the injection pressure increases. This is an unexpected result, as it is commonly believed that in- creasing the injection pressure results to higher velocities, which induce a greater boundary layer separation inside the orifice. In turn, flow separation would lead to an enhanced contraction of the flow and thus, a greater reduction in the static pressure; if this is below the local vapor pressure, more cavitation would be expected.

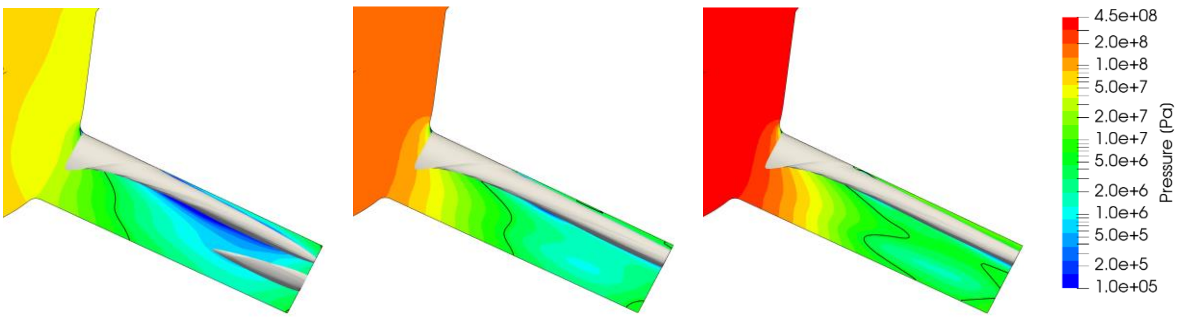

(a) 60MPa (b) 180MPa (c) 450MPa

Figure 5. 11**.** Predicted time-averaged pressure on a longitudinal slice of the injector. A solid black iso-line at 5MPa, the back pressure, and the iso-surface for 50% vapor volume fraction have been included. The colour map is in logarithmic scale and thermal effects are considered.

However, the trend observed does not follow this reasoning. Figure 5. 13 (b) quantifies the % distribution of the orifice volume having pressure in three intervals: the first one for pressures above the 5MPa value of the back pressure, the second in the range [5MPa, P v] and the last one for pressure below P_v, where cavitation is present. As seen, pressures greater than the back pressure occupy ~20% of the volume orifice at 60MPa while this percentage increases to ~55% for 450MPa. The opposite trend is observed for the other two pressure ranges; the volume with pressures below 5MPa but above the vapor pressure decreases from 65% at 60MPa down to 35% for 450MPa, while the volume occupied by pressures lower than the vapor pressure exhibits the same trend.

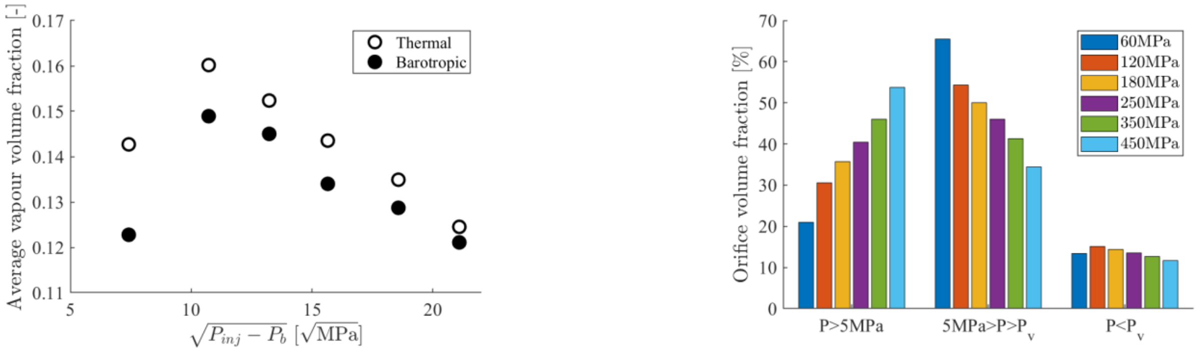

(a) (b)

Figure 5. 12**.** (a) Time-averaged vapor volume fraction inside the injector orifice versus the square root of the pressure drop estimated utilising both the barotropic and thermal models. (b) Orifice volume fraction histogram for different pressure ranges inside the orifice volume when thermal effects are considered.

Various parametric studies have been performed to disprove these results as a numerical artefact; the relevant results are summarised in Figure 5. 14 and have included injection into gas, constant fuel viscosity, non-tapering of the nozzle hole and different turbulence models such as the k-omega SST RANS model with the Reboud correction [276]. Although the absolute values of cavitation volume fraction are not the same, as cavitation is significantly de- pendant on the model and properties used, a similar reduction trend of cavitation volume fraction with the pressure drop is observed for all cases.

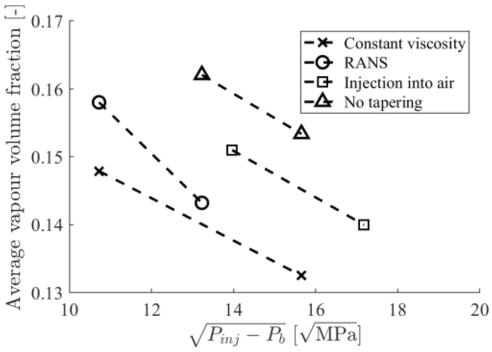

Figure 5. 13**.** Effect of boundary conditions and simulation parameters on calculated vapor volume fraction as function of pressure drop.

The increased pressures found overall also affect the amount of vapor mass within the orifice, as shown in Figure 5. 15, along the orifice length for all injection pressures; results from both the barotropic and the thermal cases are indicated. Two insets of the temperature distribution are added to the thermal case, corresponding to locations of high vapor mass flow rate at 450MPa. On the slices, an iso-line showing the location of vapor is also included. The density of the vapor fuel ρ*v* is calculated by the PC-SAFT EoS during the VLE calculations. As seen, as the injection pressure increases so does the flow rate of vapor mass along the orifice. For instance, at 20% of the orifice length and for the thermal case, the vapor mass flow rate is 0.06mg/s for 60MPa, 0.22mg/s for 180MPa and 1.02mg/s for 450MPa. However, the results for the barotropic case are significantly lower.

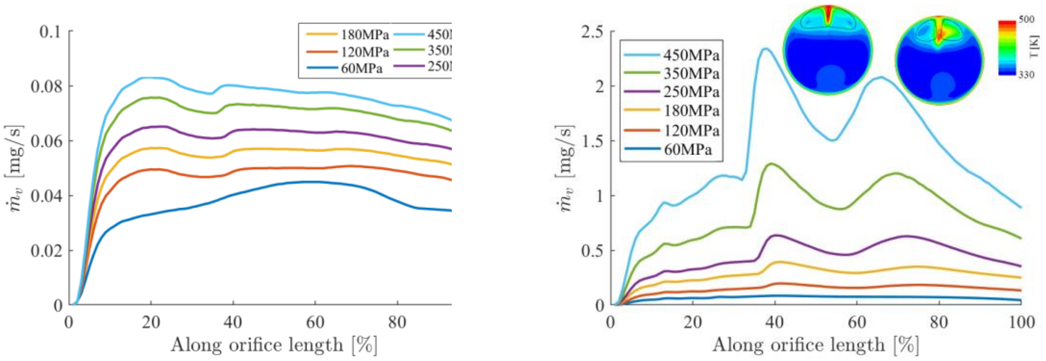

(a) Barotropic (b) Thermal

Figure 5. 14**.** Time-averaged vapor mass flow rate along the orifice length for both (a) barotropic and (b) thermal cases, for all injection pressures simulated. Two insets of the temperature distribution are added to the thermal case, corresponding to locations of high

vapor mass flow rate at 450MPa. On the slices, an iso-line showing the location of vapor is also depicted.

This difference can be explained because, when in vapor-liquid equilibrium, the vapor density increases with temperature. For instance, at 350K the saturated vapor density is $2.5 * 10^{-3}$ kg/m^3, at 360K it increases to $5.03 * 10^{-3}$ kg/m^3 , i.e. a 200% difference, and at 370K it doubles again to $9.9 * 10^{-3}$ kg/m^3 . This can be also observed on the two peaks found at approximately 40 and 75% of the orifice length, for the thermal case. In these locations, as shown by the insets, a significant increase in temperature is found, which produce also an increase in the vapor density. Figure 5. 16 shows the slope of the vapor mass flow rate along the orifice length, thus presenting the locations of net evaporation (positive values) and condensation (negative values) per meter of the orifice length as the fuel cavitates within the nozzle hole. As already seen in Figure 5. 15, overall values are higher in the thermal case due to the dependence of the vapor density on temperature, particularly at 40% and 75% of the orifice length. Nevertheless, both values for evaporation and condensation are seen to increase with injection pressure for both the barotropic and the thermal cases. This is clearly shown in the thermal case by the amplitude of the observed positive and negative peaks. For instance, at the hole entrance the value for evaporation rate is 0.6g/s •m for 60MPa, 2.7g/s •m for 180MPa and 13g/s •m for 450MPa, while at 45% of the orifice length the corresponding values for condensation are 0.07g/s •m for 60MPa, 0.62g/s •m for 180MPa and 6g/s •m for 450MPa. Moreover, while for the barotropic case most of the evaporation (values for the 450MPa case) is observed at the be- ginning of the orifice, with a value of 1.2g/s •m, followed by small positive values at 40% of 0.1g/s •m and of 0.01g/s •m at 60%, for the thermal case the peak in evaporation occurs at 40% of the orifice length, with a significantly higher value of 32g/s •m, followed by a smaller value of 13g/s •m at the entrance and of 7g/s •m at 60% of the orifice length.

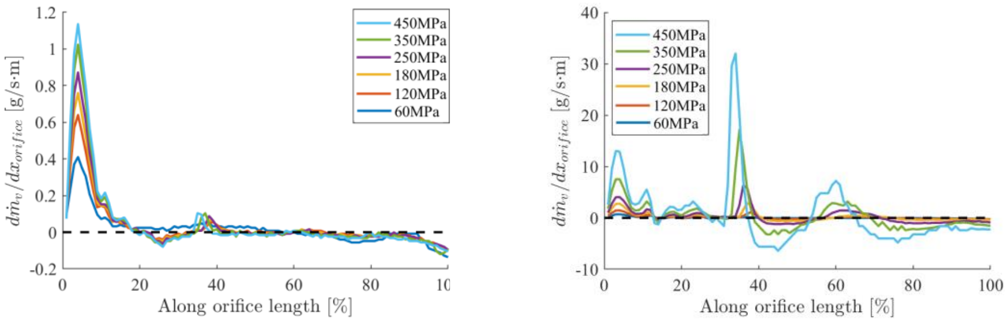

(a) Barotropic (b) Thermal

Figure 5. 15**.** Slope of the vapor mass flow rate along the orifice length, showing locations of net evaporation (positive) and condensation (negative), for both the barotropic and the thermal cases. A dashed horizontal line is added at value 0, for reference.

An additional interesting finding is related to the influence of varying simultaneously the injection and back pressures on cavitation vapor volume fraction [277] but keeping the cavitation number fixed; this is defined as:

$$CN = \frac{P_{inj} - P_b}{P_b - P_{sat}} \tag{17}$$

The cavitation number chosen is 35, which corresponds to the boundary conditions of the 180MPa case. For keeping constant cavitation number, increasing the injection pressure results to increasing the back pressure and, on the other hand, decreasing the injection pressure results to decreasing back pressure. Figure 5. 17 shows that the vapor volume fraction still decreases inside the orifice as the injection pressure increases, even by keeping constant the cavitation number. Thus, for the same injector and fluid, these results show that a constant cavitation number does not indicate a simi- lar cavity size, but it strongly depends on the absolute value of the injection and back pressure values used.

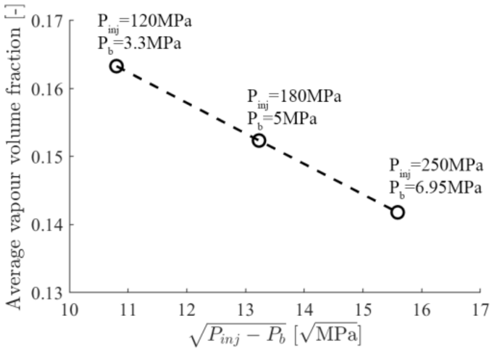

Figure 5. 16**.** Time-averaged vapor volume fraction inside the injector orifice versus the square root of the pressure drop, considering thermal effects. All cases have the same cavitation number, CN=35.

5.3.4 Preferential cavitation

One of the benefits of using the PC-SAFT EoS coupled with a VLE algorithm is that it allows the calculation of the vaporised amount of each individual fuel component. As an example, Figure 5. 18 shows the vapor mass fraction at 350K of the Diesel surrogate (dashed line) and of four representative components (the heaviest, lightest and two intermediates, in solid lines), as a function of the specific volume. As shown, the mixture vaporises at a variable rate as it expands, while each component vaporises as well at their distinct rhythm. The lightest component, i.e. 1,2,4- trimethylbenzene, is seen to vaporise at a higher rate than the mixture and vaporises completely considerably sooner. The heaviest one, i.e. n-octadecane, vaporises much slower than the mixture, but reaches the complete vaporisation at the same time.

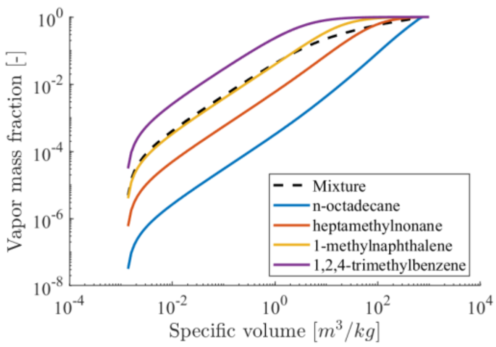

Figure 5. 17**.** Vapor mass fraction of representative components of the fuel surrogate (the heaviest, lightest and two intermediate) as a function of specific volume for a 0D expansion of the fuel at 350K.

The intermediate components vaporise at rates in between the previous ones. As the volume fraction per component cannot be retrieved from the equation of state, mass fractions are presented. The vaporised mass fraction of every component v_i, is calculated using the mass vapor fraction of the mixture θ, the composition of the vapor phase ***x*** and the composition of the total mixture ***z*** by:

$$v_i = \theta * x_i / z_i \tag{18}$$

Figure 5. 19 shows iso-surfaces of the mass vapor fraction for selected components. The plotted vapor mass fraction is selected so that the iso-surface for trimethylbenzene coincides to that of the mixture 50% vapor volume fraction.

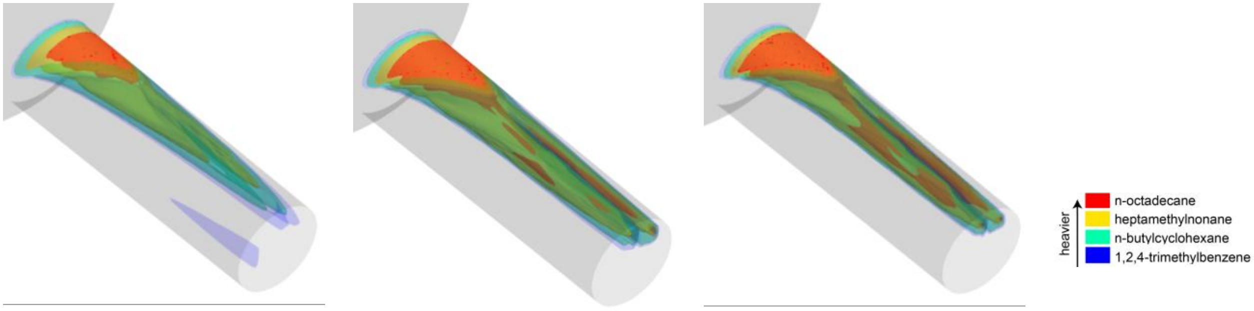

(a) 60MPa (b) 180MPa (c) 450MPa

Figure 5. 18**.** Effect of the injection pressure on partial vaporisation of selected components of the Diesel surrogate simulated. Results are time-averaged and thermal effects are considered.

As shown, trimethylbenzene is the maximum cavitating component and the heaviest one, i.e. octadecane, cavitates significantly less and mostly at the entrance of the orifice, where the flow separates, and cavitation is stronger. No significant amount of the 5 heavier components are found in the vortex cavitation cloud found at 60MPa. Moreover, as the injection pressure increases, every component is seen to cavitate further in- side the cavitating cloud, observable on the iso-surface for octadecane, due to both the higher pressures and temperatures occurring in the orifice. Figure 5. 20 shows the mass composition of the cavitating cloud inside the orifice for all injection pressures studied while Table 5 shows the actual values. The lighter components are the ones found to be in greater amount due to their higher volatility. As seen, in all cases the 4 lightest components compose more than 75% of the vapor mass. The compound most present in the total mass of the Diesel surrogate, heptamethylnonane with 35% in mass fraction, is not the one having the highest amount of vapor phase, as it is less volatile; it's relative percentage in the vapor composition is just 3.44% at 60MPa and up to 12.5% at 450MPa. Similar observations can be drawn from octadecane, which con- sists 27% of the total mass of the fuel surrogate, but in the vapor cloud it is just above 1%. On the other hand, the lighter butylcyclohexane with a 11% of the total fuel mass, provides 23% and ~24% of the mass of vapor at 60MPa and 450MPa, respectively. The lightest component in the surrogate, 1,2,4-trimethylbenzene, which 5% of the initial fuel mass, when vaporises provides 23% of the total mass of vapor at 450MPa. As seen previously in Figure 5. 16, the total mass of vapor, and as a result the mass of vapor of all components, increases with injection pressure.

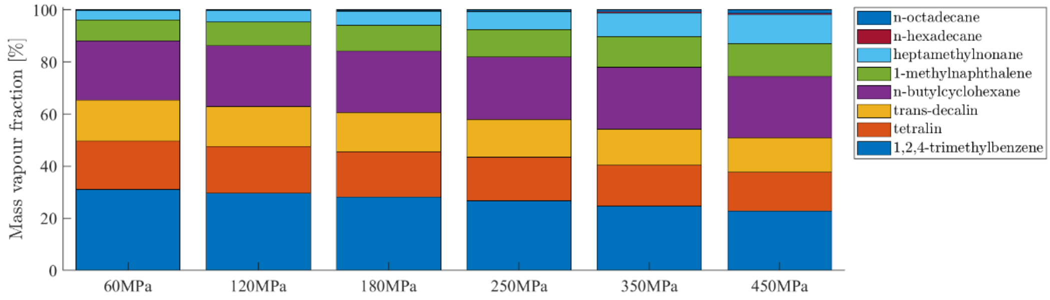

Figure 5. 19**.** Time-averaged predictions for the vaporised mass composition of the vapor cloud, in a stacked fashion, for all injection pressures.

		P_inj [MPa]					
Component	**z [% mass]**	**60**	**120**	**180**	**250**	**350**	**450**
n-octadecane	27.308	0.2416	0.2575	0.3487	0.5068	0.8566	1.3300
n-hexadecane	3.2477	0.1050	0.1338	0.1822	0.2517	0.3784	0.5209
heptamethylnonane	35.124	3.4426	4.2924	5.3811	6.7659	8.9891	11.152
1-methylnaphthalene	10.877	8.1457	9.0432	9.8387	10.675	11.723	12.463
n-butylcyclohexane	10.815	22.619	23.278	23.589	23.805	23.807	23.550
trans-decalin	4.0392	15.721	15.431	15.051	14.601	13.894	13.232
tetralin	3.8009	18.597	18.028	17.437	16.743	15.733	14.834
1,2,4-trimethylbenzene	4.7883	31.128	29.537	28.174	26.652	24.619	22.918

Table 5. 5**.** Time-averaged predictions for the vaporised mass composition of the vapor cloud, for all injection pressures. The initial surrogate mass composition is also indicated.

5.3.5 Summary and Conclusions

The present study is the first work reporting simulations of cavitation in a Diesel fuel injection at extreme injection pressures up to 450MPa. Additionally, it is the first work to report results using the molecular-based PC-SAFT equation of state for the modelling of the Diesel fuel properties, while has allowed for predictions of the preferential cavitation of the components in a Diesel injector to be reported for the first time. To assess the method against the common assumption of isothermal flow typically considered up to now in nozzle flow simulations, simulations considering an isentropic expansion of the fuel, and thus neglecting friction-induced thermal effects, have been also presented. Two major findings emerge from this study: (i) in-nozzle vapour volume fraction decreases with injection pressure, although the mass of fuel cavitating increases, and (ii) each component in the surrogate cavitates at a distinct rhythm, different to that of the mixture and to that of the other components. The trend in cavitation has been explained by observing the pressure distribution within the nozzle orifice, which increase significantly with injection pressure and effectively decrease the growth of cavitation. The composition of the fuel vapor shows that the lighter components cavitate at a significantly greater amount than the heavy ones. With increasing injection pressure, all fuel components cavitate in higher mass quantities due to the higher densities of the fuel at the pressures and temperatures developing in the nozzle orifice. As a result, the mass of the total vapor fuel also increases.

5.4 Critical Analysis

A critical question relative to this study is related to the dependency/accuracy of the simulations on the equations describing the fuel properties as function of pressure and temperature. As mentioned, the simulations carried out have utilised properties derived by the PC-SAFT EoS. This EoS has been previously used with the Diesel surrogate of this work and compared with experimental results up to 500MPa and 600K for density, viscosity and volatility with an accuracy of 1.7% for density, 2.9% in volatility and 8.3% in viscosity. Diesel fuels with different compositions have been also modelled at pressures up to 300MPa and temperatures up to 532K and the obtained accuracy against those measurements was ~2% for density and ~10% for viscosity. Other Diesel properties, such as thermal conductivity, at extreme conditions up to

450MPa and 360K can also be found accurately predicted by PC-SAFT with an accuracy of 3%. It can thus be claimed that the selected EoS is a good compromise for studying such effects in high pressure injectors.

- One of the main assumptions in the described methodology is the mechanical and thermodynamic equilibrium between the liquid and the vapor phases. With regards to the mechanical equilibrium assumption, the recent study from the authors using a two-fluid model has confirmed that differences between liquid and vapor velocities are less than 10% and only in localised locations of the flow they have been found not to affect the overall growth rate and production of vapor. The assumption of thermodynamic equilibrium is more significant. A metastable, i.e. non-thermodynamic equilibrium, state occurs when the pressure of the liquid drops below the saturation pressure and no vapor is formed due to the rapid expansion of the liquid. In the literature, non-thermodynamic equilibrium models, such as the well-known mass transfer models are used. Predictions utilising such mass transfer models tend towards equilibrium by increasing the evaporation/condensation coefficients. Apart from mass transfer models, in the literature there are models relying on the solution of the full Rayleigh-Plesset equation, commonly done in a Lagrangian reference frame, thus incorporating second order effects and the influence of surface tension. Nevertheless, it is possible to use this time-scale to estimate that, as the residence time of the fluid in the injection hole has a minimum value of the order of 1μs, that for the 450MPa case, the time to reach equilibrium would be, at least, 100 times faster.

Chapter 6 Large-eddy simulation of turbulent cavitating flow in a Diesel injector including needle movement, two phase cavitation model for Diesel Fuel B0 2015, in OpenFOAM®

6.1 Two phase cavitation model for Diesel Fuel B0 2015

Since Diesel properties vary significantly with the pressure levels in the injection systems, both liquid phase viscosity and density are assumed to vary with pressure only. A two-step barotropic equation of state is used by Koukouvinis et al. [111]. The modified Tait equation of state is used for the liquid phase. For the vapor mixture the isentropic approximation proposed by Egerer et al.[82]is used. The piece -wise EoS is provided by the following expression for the pressure as a function of density:

$$\boldsymbol{p}(\boldsymbol{\rho}) = \begin{cases} (\boldsymbol{B} + \boldsymbol{p_{sat}})\left[\left(\dfrac{\boldsymbol{\rho}}{\boldsymbol{\rho_{sat,L}}}\right)^{\boldsymbol{n}}\right] - \boldsymbol{B}, & \boldsymbol{\rho} \geq \boldsymbol{\rho_{sat,L}} \\ \boldsymbol{p_{sat}} + \boldsymbol{C_1}\left[\dfrac{\mathbf{1}}{\boldsymbol{\rho_{sat,L}}} - \dfrac{\mathbf{1}}{\boldsymbol{\rho}}\right], & \boldsymbol{\rho} < \boldsymbol{\rho_{sat,L}}\,, \end{cases} \tag{1}$$

with C1 and n liquid dependent constants and ρsat.L is the density at saturation pressure psat. This equation of state has the advantage that can handle both large and negative absolute pressures. For all materials the exponent n is set to 7.15, since such values correspond to weakly compressible materials such as liquids. For the injector flow the properties of the liquid are considered on an average temperature level of 396 K. B is fluid-specific parameter, c is speed of sound and the vapor fraction is a function of density, as shown in (2). A specific reference state, following Safarov et al. [278], is chosen. In Table 6. 1 and 6. 2, the numerical values for the reference state for computing the Tait parameters are provided. The saturation point properties for the liquid and the vapor phase are provided in Table 6. 3. Also, the liquid and vapor phase in the cavitating liquid is assumed to be in thermal and mechanical equilibrium and we apply the homogenous-mixture cavitation model.

$$\boldsymbol{B} = \frac{\rho {C_1}^2}{n}, \qquad \boldsymbol{c} = \sqrt{\left(\frac{\partial p}{\partial \rho}\right)_S}, \tag{2}$$

Property	unit	value
Inlet pressure	[10^6 Pa]	180
Density	[kg/m^3]	851
Speed of sound	[m/s]	1700

Table 6. 1. Thermophysical properties at 180 MPa, 396K.

Property	unit	value
Outlet pressure	[10^6 Pa]	5
Density	[kg/m^3]	750
Speed of sound	[m/s]	1070

Table 6. 2. Thermophysical properties at 5 MPa, 396K.

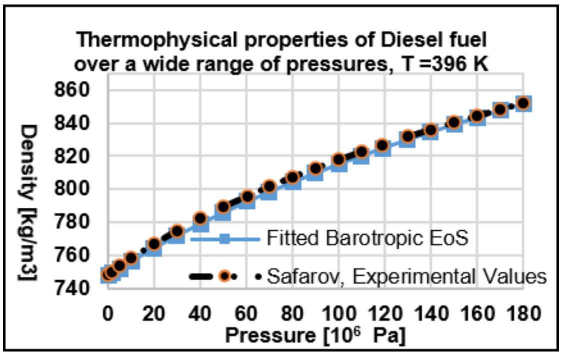

Figure 6. 1. EoS with reference data of Safarov et al. [278]

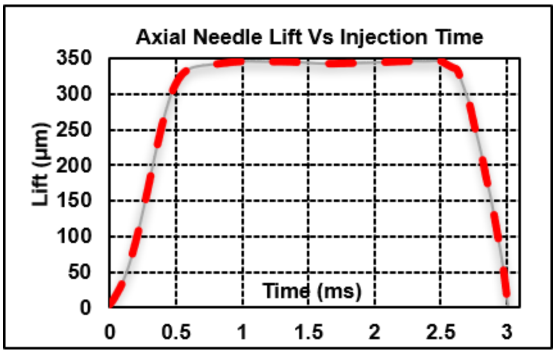

Figure 6. 2. Needle motion of the injector.

Property	unit	value
Saturation pressure	[KPa]	8
Saturation density,L	[kg/m^3]	747
Speed of sound	[m/s]	1060
Saturation density,V	[kg/m^3]	0.1
Viscosity, L	[KPa s]	0.6
Viscosity, V	[KPa s]	7.49* 10^{-3}

Table 6.3.Fluid parameters for isothermal Diesel B0 2015.

	unit	value
Needle radius	mm	1.711
Orifice length	mm	1.262
Orifice diameter Entrance Din	mm	0.37
Orifice diameter Exit Dout	mm	0.359
Sac volume	mm^3	1.19
K-factor Din -Dout	-	1.1

Table 6.4. Geometric dimensions of the examined injector.

6.2 Description of the examined injector and testing conditions

The validation of the new solver is presented for the case of an unsteady simulation for Diesel fuel within a moving injector needle with dynamic mesh deformation. The geometry is represented in Figure 6. 3 and the details of the injector geometry are presented in Table 6. 4. The simulation was carried out using the WALE model that is designed to return the correct wall-asymptotic behaviour for bounded flows. This efficient SGS model is proposed by Nicoud and Ducros (1999) [184], which is based on the square of the gradient tensor and is characterised by a realistic near wall behaviour. The spatial operator consists of a mixing of both the local strain, rotation rates and the eddy viscosity goes naturally to zero in the vicinity of a wall. As shown in Figure 6. 4 the injector consists of five orifices, but only the 1/5th of the domain was simulated. Symmetry boundary conditions have been applied at the side of the computational domain. The needle motion is assumed to be in the axial – z direction only and no eccentricity effects were considered. The total injection duration is 3 ms as shown in Figure 6. 2. Pressure boundary conditions are set according to the upstream pressure profile and downstream pressure, while needle motion is set according to the needle lift profile, shown in Figure 6. 2.

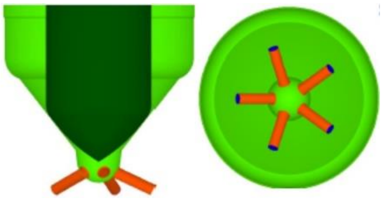

Figure 6. 3**.** Different views of the Diesel injector.

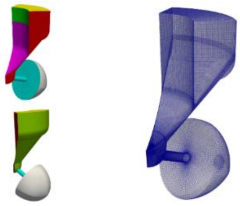

Figure 6. 4**.** Computational Volume of the 1/5th of injector.

The computational mesh used consists of a hexahedral block structured zone, with the exception of an unstructured tetrahedral zone in the sac volume before the orifice entrance. Mesh motion is performed with a cell-based deformation algorithm which moves the computational points and cells and it stretches the cells in a uniform way. The needle lift was initially set at 0.6 μm with 5 cells in the gap between needle and needle seat. The initial field was obtained from a steady state run. Significant turbulence is expected to be generated, as will be shown later, during the lift of the needle between the needle seat passage, inside the sac volume and in the orifice. The total cell count of the computational mesh is initially almost 1.0 million computational cells and finally reaches a peak of 1.8 million cells. A pure linear second order scheme was used for the interpolation of the flow field variables, while a hybrid scheme between central and second order upwind was used for the reconstruction of the conservative variables. The erosion patterns from the endurance tests are shown in Figure 6. 5. The Figure shows the X-ray CT scans of the sac/orifice and needle of two prototype Diesel injectors with the same endurance test hours.

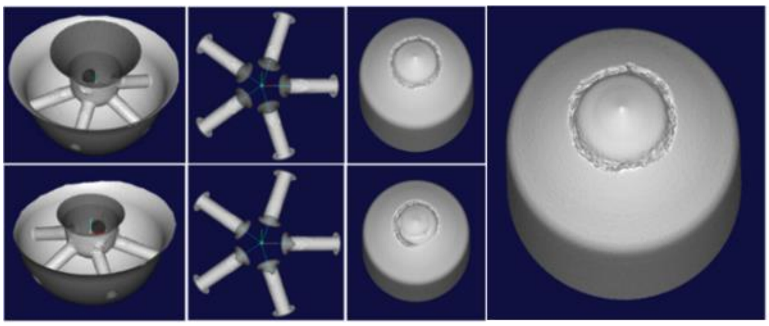

Figure 6. 5**.** From left to right. Erosion details at various locations. Analysis of the needle surface erosion pattern using image processing tool.

In Figure 6. 5, the analysis of the erosion pattern of the needle surface is presented. By using two different methods the inner and the outer radii of the erosion ring pattern is identified. These radii were found to be 0.6 mm and 0.8 mm. The experimental results obtained from all the endurance tests suggest that the erosion patterns are consistent, that is a similar erosion trend develops for injectors tested, at the same time intervals. This injector has signs of erosion damage inside the sac volume that become apparent rather later, after thousands of hours of continuous operation. The sac volume seems to be much less affected by erosion damage than the needle while the injector holes are barely affected by erosion. In the nozzle holes, the injector is generally less prone to erosion damage, where the damage is minor, in the form of a minor pit near the orifice entrance.

6.3 Analysis of the flow field

The analysis of the turbulent flow field reveals that the opening phase consists of four different stages. During the stage 1, (see Figure 6. 6), between 0.06 µs and 6 µs, a negative mass flow rate is observed. As seen in Figure 6. 7(Right), at injection time 5.05 µs the shear layer instabilities in the needle seat passage triggers the formation of dense attached cavitation. The external front part of the cavitation formation is separated and it collapses before the entrance in the sac volume, as illustrated in Figure 6. 7(Right), (c). As shown in Figure 6. 7 (Center), at injection time 5.05 µs strong collapse events of vapor structures in the needle seat cause the formation of shock waves. During the stage 2 of the opening phase, (see Figure 6. 6 from 6 µs up to 150 µs), complex cavitation appears both at the needle seat, at the sac and in the orifice, as shown in Figure 6. 7(Right), (a-c), at injection time 38.58 µs. The attached cavitation at the needle is more extended and protrudes into the sac. This vapor distribution interacts with the flow in the sac inducing vortices that result in further cavitation in the orifice.

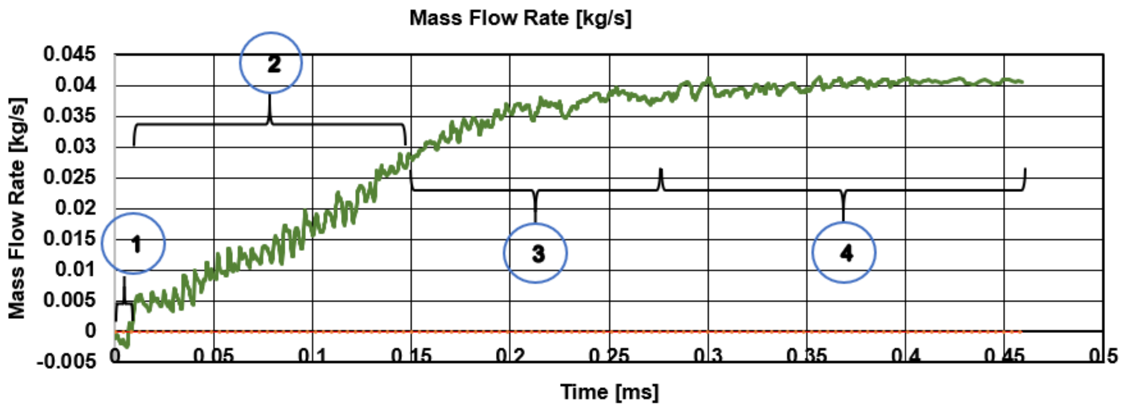

Figure 6. 6**.** Temporal evolution of the mass flow rate. During the opening phase, the flow field inside the injector characterized by four different stages which influence significantly the erosion pattern and the cavitation vortex and cavitation string structures in the injector.

As observed from the three consecutive realisations around the instance 38.58 μs a vortex cavitation formation appears within the sac (a) and (b) collapses at time (c) resulting in a shock apparent in the pressure distribution, as shown in Figure 6. 7(Center). A sheet cavity formation is observed at the perimeter of the orifice and limits the mass flow rate. During the stage 1, (see Figure 6. 6), between 0.06 μs and 6 μs, a negative mass flow rate is observed. As seen in Figure 6. 7(Right), at injection time 5.05 μs the shear layer instabilities in the needle seat passage triggers the formation of dense attached cavitation. The external front part of the cavitation formation is separated and it collapses before the entrance in the sac volume, as illustrated in Figure 6. 7(Right), (c). As shown in Figure 6. 7 (Center), at injection time 5.05 μs strong collapse events of vapor structures in the needle seat cause the formation of shock waves.

During the stage 2 of the opening phase, (see Figure 6. 6 from 6 μs up to 150 μs), complex cavitation appears both at the needle seat, at the sac and in the orifice, as shown in Figure 6. 7(Right), (a-c), at injection time 38.58 μs the attached cavitation at the needle is more extended and protrudes into the sac. This vapor distribution interacts with the flow in the sac inducing vortices that result in further cavitation in the orifice.

1 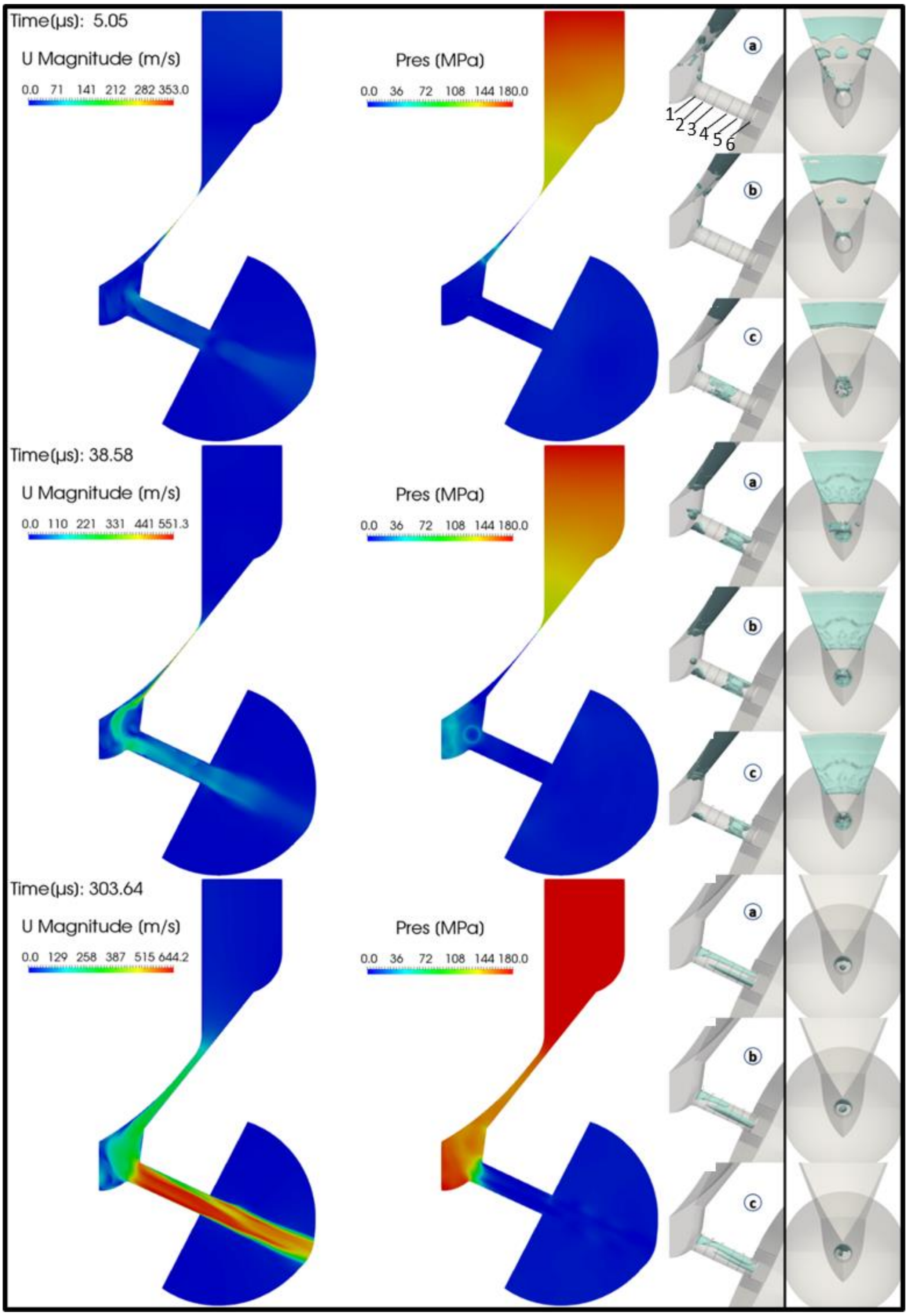

Figure 6. 7**.** Top to bottom: Realisation of the flow field inside the Diesel injector for three instances (T=1 T=2 T=3). Left column: Velocity magnitude distribution at the midplane. Center column: Pressure distribution. Right: Vapor distribution at three different instances (a-c). A series of images (a-c) illustrating the growth, developed and the collapse of the developed cavitation formation. Slices (1-6) are located from at 1: 1215µm, 2: 1078µm, 3: 901µm, 4:

601μm, 5: 350μm and 6: 10μm from orifices exit, and depict the location of vapor into the orifice volume.

During the stage 3 of the opening phase, (see Figure 6. 6 from 150 μs up to 270 μs), a transition of the cavitation from the lower to upper orifice surface is predicted. Unstable vortex string formations initiates from the orifice inlet and significantly influence the formation the velocity field even after the orifices exit. As shown in Figure 6. 6 the stage 4 of the opening phase, (see Figure 6. 6 from 270 μs up to 470 μs), cavitation occurs only in the orifice volume, as shown in Figure 6. 7(Right), (a-c), at injection time 303.64 μs. The flow is attached at the vertical wall of sac volume, as seen in Figure 6. 7(Left). As illustrated in Figure 6. 7(Right), (a-c), sheet cavitation formation is observed at the upper orifice surface and large stable vortical and vapor structures in the axial direction now dominate the flow. Due to the tapered shape of the nozzle holes, these vortices are further stretched and cause vortex cavitation at the nozzle outlet plane. The visualizations of the vapor shedding cycle shown in Figure 6. 7(Right), (a-c).

6.4 Comparison with experimental data: Cavitation Erosion

From the experiments a clear pattern is identified with erosion formation on the needle surface in the form of a deeply engraved ring shape, more specifically a ring with inner and outer radii of 0.6 mm and 0.8 mm (Figure 6.. 5). Considering the sac damage, the injector needle is less affected by erosion very close to orifice inlet.

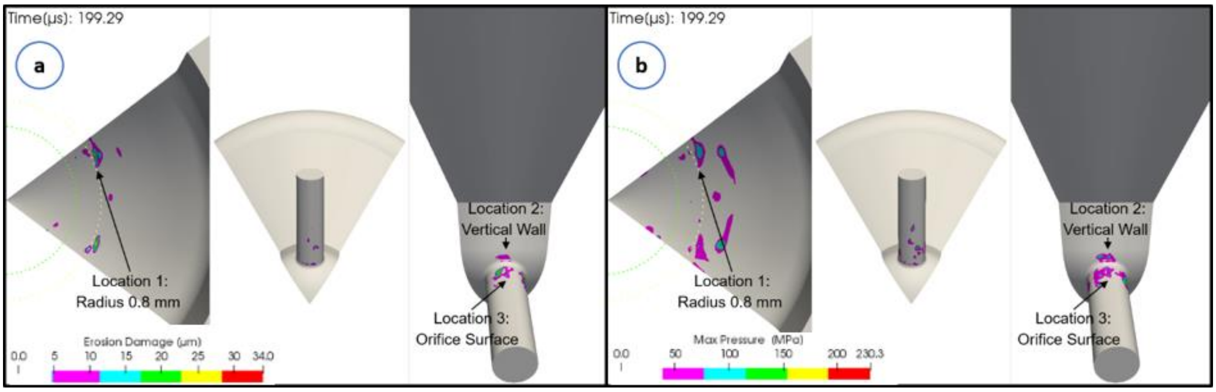

Figure 6. 8**.** Spatial distribution of potential cavitation damage. (a) Erosion damage prediction [μm]. (b) Maximum wall collapse pressures recorded at the walls [MPa].

A pit-count method proposed by Dular et al. [279] equation 7, was applied to evaluate the potential damage. The erosion model is based on the physical description of phenomena from cavitation cloud implosion, pressure wave emission and its attenuation, micro-jet formation and finally to the pit formation. As shown in Figure 6. 8, the three locations with potential erosion are predicted very well from the simulation results. These locations are at the orifice inlet, at the sac vertical wall and on the needle surface. The identification of erosion sensitive areas during the design process of fuel injectors is a key factor for performance optimization and durability. The erosion prediction from pressure peaks, in Figure 6. 8(b), significantly exceeding and shows a very good agreement with the experimental data, at all the investigated regions, including needle, vertical sac wall and orifice inlet. All of these methods-indexes could potentially correlate to the erosion patterns. In order to detects isolated vapor-structure collapses (collapse detector) a collapse detector algorithm is used for all the mentioned indexes. In order to compare the numerical results with the experimental data two circles are used positioned at radius 0.6 mm and 0.8 mm. In the Figure 6. 8(a) the potential erosion damage until injection time 199.29 μs is presented. In Figure. 8(a) the potential damage is predicted at almost at the same locations of the injector geometry. After injection time 150 μs no more cavitation formation is predicted in the needle seat passage region. The predicted results from the erosion damage model are in very good agreement with the experimental data. Moreover, the maximum collapse pressure field and the erosion damage model have a good correlation with the erosion pattern from the experimental data, specifically at the needle surface, at the upper orifice surface and on the vertical wall of the sac volume, but both of these indexes predict a small pit formation at the lower orifice surface.

6.5 Interaction between vortical structures and cavitation mechanisms

Figure 6. 9 shows the prevalent streamwise vortical structures, in different cross-sections. At needle lift 63.7 μm and injection time 154.31 μs, a small separation which is visible on the lower side of the orifice near the inlet edge disappears before the second cross section, as shown in Figure 6. 9, (cross-sections 1 and 2). This vortical structure originates from the boundary-layer separation of the flow in the sac region. Its size increases significantly to 95% of the orifice length, see Figure 6. 9 (cross-sections 1-6, and image c, at injection time 155.73 μs). Due to the acceleration of the flow, the resulting streamwise velocity gradient stretches this cavity forming string cavitation.

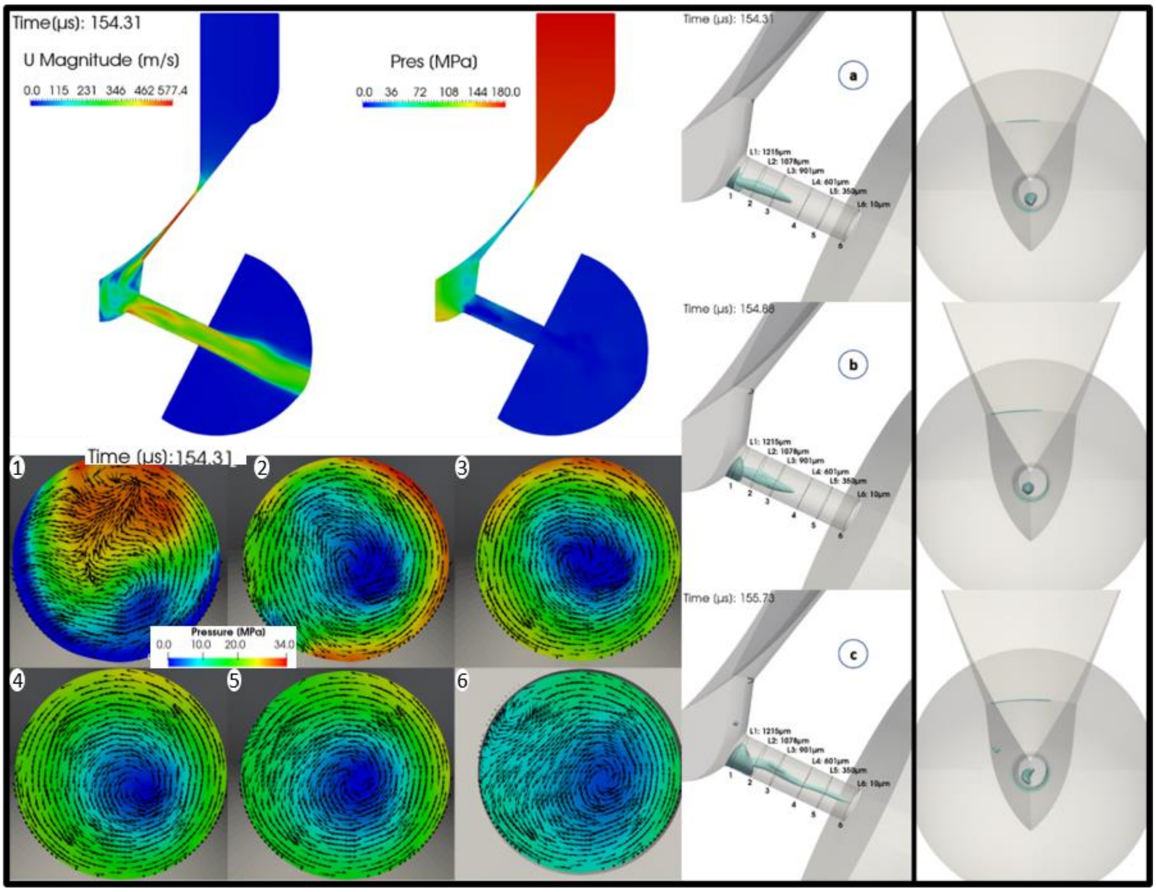

Figure 6. 9. Left column: Velocity magnitude distribution at the midplane and Pressure distribution. Instantaneous pressure field and tangential vectors of velocity distribution on six cross-sections normal to the orifice of the injector. Right: Vapor distribution at three different instances (a-c). A series of images (a-c) illustrating the growth and the developed of the developed cavitation formation.

6.6 Conclusions

This paper assesses the potential of 2-phase cavitation model, coupled with the developed fully compressible density-based solver incorporating the transient effects of the injector geometry, in the prediction of erosion effects. A reliable prediction of erosion-sensitive areas due to collapse events during the opening of the needle could only be predicted accurately by including the unsteady needle motion with a fully compressible treatment of the liquid and the liquid-vapor mixture, resolving dynamics of shock waves. This numerical approach plays an essential role for the prediction of cavitation erosion and allows for the detection of erosion-relevant events. A high-frequency vortex cavitation, associated with boundary-layer separation and shear-layer instabilities at orifice and the needle seat passage, is the predominant cavitation mechanism. Moreover, there is very good correlation of the predicted potential erosion damage locations with the observed erosion patterns. Four different stages of the opening injection cycle have been defined, during which the flow characteristics differ significantly and determine the erosion pattern.

Chapter 7 Conclusions and Future work

An explicit density-based solver of the compressible Navier-Stokes (NS) on ALE framework suitable for industrial multiphase flows with complex moving geometries has been developed in OpenFOAM. The flow solver is combined with two thermodynamic closure models for the liquid, vapor and vapor liquid equilibrium (VLE) property variation as function of pressure and temperature. The first is based on tabulated data for a 4-component Diesel fuel surrogate, derived from the Perturbed-Chain, Statistical Associating Fluid Theory (PC-SAFT) Equation of State (EoS), allowing for thermal effects to be quantified. The second thermodynamic closure is based on the widely used barotropic Equation of State (EoS) approximation between density and pressure and neglects viscous heating. The Wall Adapting Local Eddy viscosity (WALE) LES model was used to resolve sub-grid scale turbulence while a cell-based mesh deformation Arbitrary Lagrangian–Eulerian (ALE) formulation is used for modelling the injector's needle valve movement.

The comparison between the two thermodynamic models reveals that overall, the comparison between those two thermodynamic closure models discloses that there are minor differences in the predicted nozzle discharge coefficient but significant differences in the temperature distribution inside the fuel injector, the mean injection temperature and the vapor volume fraction inside the injector's volume. Model predictions were found in perfect agreement against 0-D estimates of the temporal variation of the mean fuel temperature difference between the injector's inlet and outlet during the injection period. On one hand, the strong mechanism of viscous heating produced by wall friction, leading to significant increase of the fuel temperature at the upper orifice surface where local temperatures can exceed the fuel's boiling temperature and superheated vapor is forming.

Moreover, a significant increase of temperature in the needle seat passage takes place during the early stages of the needle valve opening, due to the very high velocity magnitude, of the order of 1000m/s and speed of sound around 750 m/s for the case of 450MPa. On the other hand, liquid expansion due to depressurisation results to liquid cooling relative to the fuel's feed temperature; this is observed at the central part of the injection orifice and into the needle-needle seat passage. The sub-cooled region into the injector is more evident during the closing phase of the needle valve, the heated region is more pronounced during the opening phase; it is evident that the needle motion affects the thermal boundary layer and possibly the inception and cavity sheet growth and transition, especially at low lifts. The origin of vortex cavitation structures was traced into the sac volume and on needle tip surface. Predictions from the full thermodynamic closure model for the peak pressures on the walls of the nozzle were also compared against corresponding X-ray derived surface erosion images obtained from durability tests. Locations of erosion on the surfaces of the needle valve, sac volume and injection holes were in good agreement with the relevant observations.

Overall, the comparison between different injection pressures discloses significant differences in the temperature distribution and vapor volume inside the sac, needle and orifice injector regions from 0 to 60 μm. As the injection pressure increased the size and growth of strong vortices inside the sac volume influence the locations expected to be more vulnerable to cavitation erosion. Results indicate that with increasing injection pressures, an unprecedented decrease of cavitation volume inside the fuel injector occurs. Has been observed that the pressure distribution within the nozzle orifice increase significantly with injection pressure and effectively decrease the growth of cavitation. The composition of the fuel vapor shows that the lighter components cavitate at a significantly greater amount than the heavy ones. With increasing injection pressure, all fuel components cavitate in higher mass quantities due to the higher densities of the fuel at the pressures and temperatures developing in the nozzle orifice.

As future work, the effect of non-condensable gas [122] which is necessary to understand how the flow phenomena inside a high-pressure injection system (450MPa), like fuel temperature distribution, turbulence, vortex cavitation and vapor, influence jet and spray formation and atomization characteristics for a more efficient mixing and combustion process, has not been considered. Also, the developed methodology can be expanded towards two different directions, either for moving boundary or for Fluid Structure Interaction (FSI) problems incorporating IBM [63] or layer additional and removal algorithms [117], [118]. In industrial cases, like in Diesel injectors the extension of the mentioned CFD solver with the coupling with the layer additional and removal and attach/detach of boundaries algorithms [280] would be a great advantage. Also in fluid-structure interaction methods for bypass pumps, artificial hearts, and mechanical heart valves and in applications of cavitation in the context of bioengineering [281–284].

Emphasis should be placed on the complete closing of the needle seat passage. Even though the flow has been simulated at low needle lifts during opening and closing phase the transient effects during opening from zero needle lift and closing at zero needle lift could influence significant the flow pattern. The simulation of the dribbling effect is significant to illuminate nozzle geometry, injection and cylinder boundary condition influences on the dribble event [126,153].

Another significant assumption which may influence the results is the assumption to simulate only the 1/5th of the Injector volume. This assumption adds limitations to the possible vortex and vortex cavitation interaction between the orifices. After the examination of the results some step could be followed in order to reduce the erosion and the cavitation into the injector volume. As depicted in Figure 4. 5 and Figure 4. 8 the amount of vapour and the temperature of the fuel are the same for all the cases after the 70 µm. A linear increase of pressure from 180 MPa to 450 MPa could reduce the amount of vapour into the injector under 450 MPa injection pressure case. Also, the closing profile of the needle should be slower in order to avoid high collapse pressures which could lead to erosion.

Appendix 1. Simulation of transient effects in a fuel injector nozzle using real-fluid thermodynamic closure.

Critical Analysis

- Moving/deformable grid approach and the ALE framework:

The accuracy of modelling the transient effects of the needle during the injection cycle depends largely on the accuracy of the moving/deformable grid approach and the ALE framework. This might be though as trivial as other research on Diesel injectors showed possible ways to do so. However, the numerical accuracy of ALE especially close to the boundary walls is crucial for the accurate prediction of heating of the fuel due to viscous heating and the prediction for the film like cavitation on the needle seat surface.

- Also, the needle motion is assumed to be in the axial – z direction without eccentricity effects:

Although, from the literature, it has been found that the physical dimensions of the needle valve assembly and the injection pressure have a significant impact on the radial displacement of the needle during the injection cycle and as a result to the erosion pattern, the results of this study have revealed an accurate agreement with the experimental data. This injector has signs of erosion damage inside the sac volume, to the hole inlet, that become apparent rather later, after thousands of hours of continuous operation. The sac volume seems to be much less affected by erosion damage than the needle while the injector holes are barely affected by erosion. Model predictions are compared against corresponding X-ray surface erosion images obtained from injector durability tests, showing good agreement especially on the moving needle surface.

- The Wall Adapting Local Eddy viscosity (WALE) LES:

LES model was used to predict incipient and developed cavitation, while also capturing the shear layer instability, vortex shedding and cavitating vortex formation. It is evident that the LES turbulence model combined with the appropriate computational mesh it is capable to reveal the complex coherent vortical structures and the cavitation vortex interaction. Also, revealed with accuracy the erosion pattern dependence on coherent vortex structures in the sac volume.

- Differences between the thermodynamic closure 1 and 2

Even though the Cd coefficient is slightly different the temperature and viscosity fields reveal different patterns. In Figure 3. 18, the comparison between the different thermodynamic closure models reveals that the velocity, dynamic viscosity and temperature profiles exhibit significant differences; the density field shows more similarities. In Figure 3. 18(b) the absence of temperature variations leads to a homogeneous density and viscosity field into the orifice volume and as a result this leads to the suppression of the inlet or sac volume swirl [285] and development of the vortex structures inside the injection hole. Comparison between the tangential velocity fields between the Figure 3. 18(b) and Figure 3. 18(a) reveals that the tangential velocity is higher using full thermodynamic model. On cross section 3, two counter-rotating primary vortices are found, indicated as V_1 and V_2. The larger and stronger V_1 occupies the upper part of the orifice while V_2 is found at its lower part. It is clear that the gradients on the depicted variables take place at the same location where V_1 is developing. The temperature of the fuel is lower compared to the inlet temperature at the centre of V_1; this causes an increase of the dynamic viscosity at this location. In Figure 3. 18(a), it is evident that the fluctuations of the temperature cause significant fluctuation on the viscosity field.

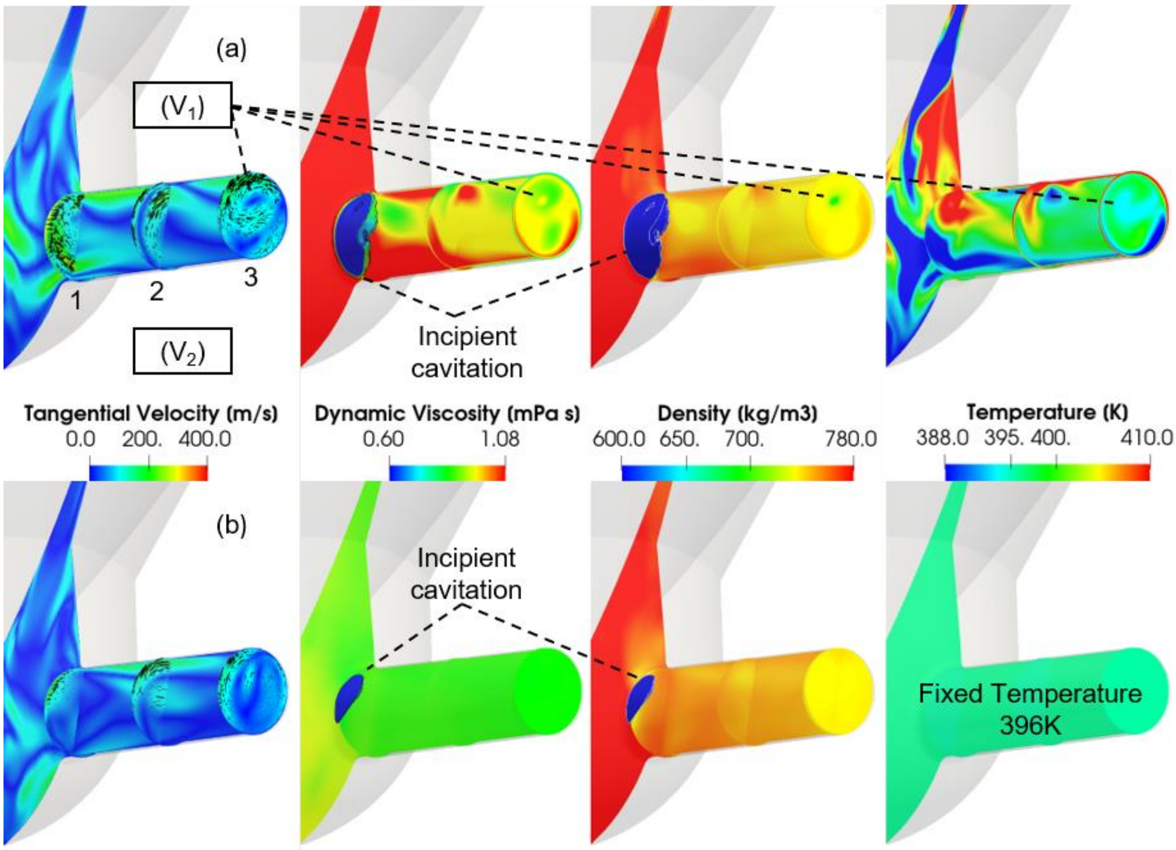

Figure 3. 19. Instantaneous tangential velocity, dynamic viscosity, density and temperature distribution on slices normal to the orifice and at the midplane of the injector, at time

instants147μs (60 μm needle lift). using (a) full thermodynamic model and (b) barotropic model. The vapor volume fraction α = 0.01-1.0 is coloured by the dynamic viscosity and by the density.

After that time, two opposing processes take place in the needle seat passage: viscous heating increasing fuel temperature while fuel cooling due to de-pressurisation. During stage 2 of the opening phase, from 150 μs (60 μm) up to 500 μs (315 μm)) for both examined cases the simulation reveals similar turbulent and vapor patterns. Specifically, a transition of the cavitation from the lower to upper orifice surface is predicted. Unstable vortex string formations initiate from the needle tip, travel into the orifice inlet and significantly influence the formation the velocity and vapor field, reducing the mass flow rate through the nozzle. During this opening phase, cavitation occurs only in the orifice; sheet cavitation formation is observed at the upper orifice surface and large stable vortical and vapor structures aligned with the flow direction dominate. Due to the tapered shape of the nozzle holes, these cavitating vortices are further stretched towards the exit of the orifice.

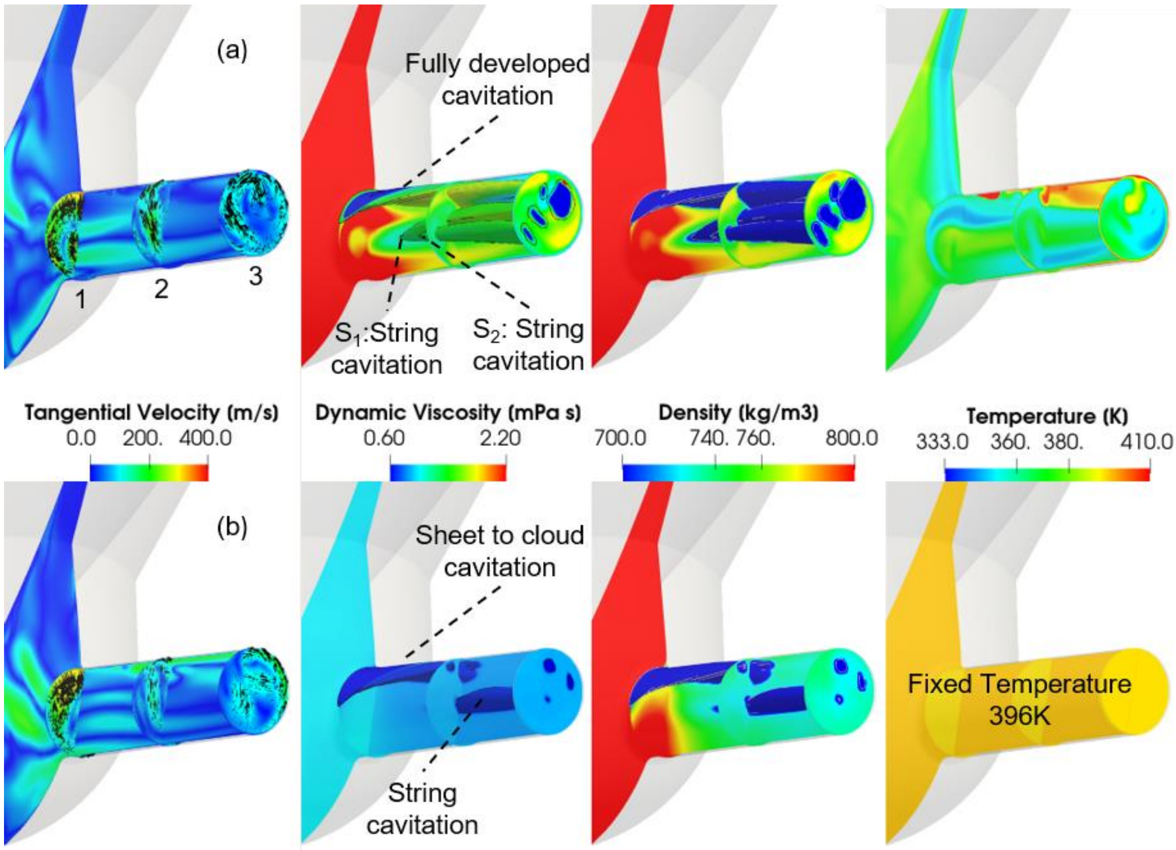

Figure 3. 20**.** Instantaneous tangential velocity, dynamic viscosity, density and temperature distribution on slices normal to the orifice and at the midplane of the injector, at time instant 248μs (132 μm needle lift) using (a) full thermodynamic model and (b) barotropic model. Instantaneous tangential velocity, dynamic viscosity, density and temperature distribution on slices normal to the orifice and at the midplane of the injector, at time instant 248μs (132 μm needle lift). The vapor volume fraction α = 0.01-1.0 is coloured by the dynamic viscosity and by the density.

A closer examination, reveals that the Cd values may different even by 18% at 248 μs due to significant differences at the temperature field and its effect on the viscosity of the fuel. Progressively, as the needle lifts the fuel is heated less and the sac volume is filled with the cooler feed liquid. The average fuel temperature at 248 μs is predicted to be 368K, which is significantly different in comparison to the 396K assumed in isentropic. Moreover, during this second opening stage the amount of the vapor shows noticeable increase with fluctuations for the full thermodynamic closure case when compared to the isothermal thermodynamic model. That leads to different secondary flow pattern into the sac volume, vortical and vapor structures in direction of the flow. As shown in Figure 3. 19, the comparison between the different thermodynamic models reveals that the velocity, dynamic viscosity and temperature profiles show different trends, and this explains the difference of the Cd in Figure 3. 6 and at the percentage of vapor volume fraction in Figure 3. 9.

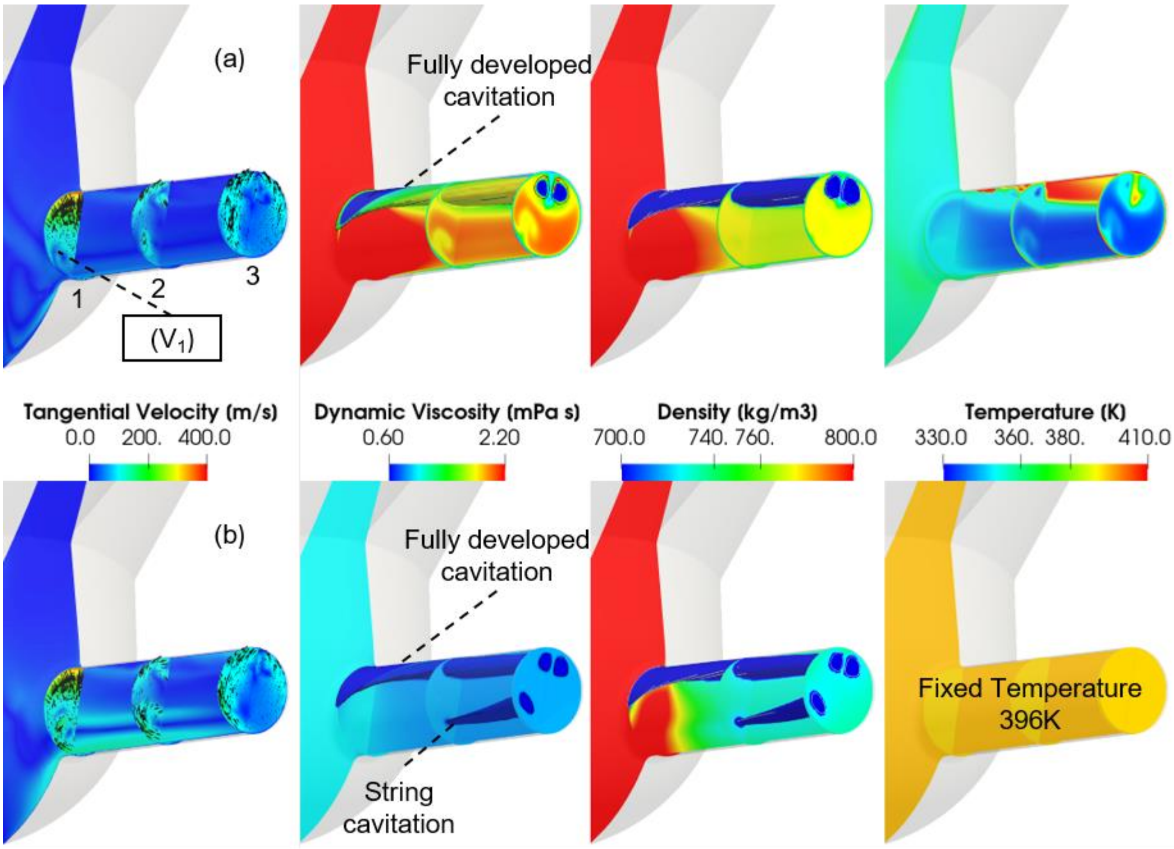

Figure 3. 21**.** Instantaneous tangential velocity, dynamic viscosity, density and temperature distribution on slices normal to the orifice and at the midplane of the injector, at 989μs (350 μm needle lift) after start of injection, (SOI) using (a) full thermodynamic model and (b) barotropic model. The vapor volume fraction α = 0.01-1.0 is coloured by the dynamic viscosity and density.

As shown in Figure 3. 19(a), the injector's sac and orifice are at different temperatures. Some regions are at inlet temperature (350K) or even lower, while others have temperature higher than 390K, due to viscous heating on the needle surface and on the orifice upper wall. As a result, the viscosity field is not uniform and that gives rise to the vortex formation, that in turn leads to formation of cavitation. These strong coherent large-scale vortices underlie on the needle tip surface or sac volume causing strong string cavitation extending into the orifice volume. Furthermore, in Figure 3. 19(a), three different cavitation structures are evident, which have complex shapes. The first one is the fully developed cavitation at the upper surface of the orifice wall, which detached from the wall after slice 2. The other two cavitation structures are the two counter rotating vortices indicated as string cavitation S_1 and S_2 in Figure 3. 19(a). S_1 and S_2 are long and narrow extending to the exit of the injection hole. The S_1 and S_2 are results of the strong swirl of the flow into the sac volume and due to acceleration of the flow as the cross-sectional area of the orifice decreasing.

During the opening phase from 500 μs (315 μm) up to 989 μs (350 μm)), both examined cases reveal similar flow and vapor patterns; the differences in the Cd coefficient and the vapor volume percentage are between 1%-3%. The flow is attached at the vertical wall of sac volume while fully developed cavitation formation is observed at the upper orifice surface. At this region superheated vapor **(**higher than 600K) forms but the central part of the orifice temperatures can be up to 20 degrees lower that the inlet temperature. At the same time, the strong wall friction which causes high temperatures around the orifice surface does not heat significant amount of the fuel. The average fuel temperature at 985 μs after SOI is ~349K. Still, the integral amount of the vapor shows a slight difference between the full thermodynamic closure and the case with isothermal thermodynamic model (see Figure 9). Even though there are small differences at the Cd the dynamic viscosity and temperature profiles show noticeable differences. As shown in Figure 3. 20(a), on cross section 1, only the stronger vortex V_1 still exists but with reduced strength compared to earlier times. Along its path and observing the viscosity, density and temperature fields on cross sections 1, 2 and 3, it is evident that their variation coincides with the V_1. Comparison between the different thermodynamic models reveals that even the tangential velocity shows higher values for the barotropic model case which cause vortex cavitation. It is obvious that viscosity plays significant role of how much strong the secondary flow is (V_1 swirl) close to the sac bottom and with which rate is diffused and is transmitted to the nozzle volume through the backflow.

Appendix 2. Transient cavitation and friction-induced heating effects of diesel fuel during the needle valve early opening stages for discharge pressures up to 450MPa.

- Comparison against corresponding X-ray surface erosion images obtained from injector durability tests, showing good agreement:

Using the available erosion data for the 180MPa test case some potential results could be produced for the cases with 350 MPa and 450MPa injection pressure. The extreme injection pressures induce fuel jet velocities in the order of 1100 m/s, which in turn, affect the formation of coherent vortical flow structures into the nozzle's sac volume. It is found, in particular, that the fuel jet velocity variations with increasing discharge pressure, affect the locations of cavitation formation and collapse, which in turn, lead to different potential locations of erosion of the surface of the needle valve.

- Moving/deformable grid approach, LES and ALE framework:

The accuracy of modelling of the transient thermal effects of the needle during the early injection close to the small needle gap boundary walls reveals that the numerical model is capable for demanding and challenging prediction of heating fuel due to strong viscous heating in the order of 600 K and of fuel jet velocities in the order of 1100 m/s. However, a combination with a Layer addition/removal approach could made the solver free of change of the computational mesh if the computational cells are stretched enough during the deformation. As shown in Figure 4. 13, the temporal evolution of fuel temperature at the needle passage shows that the higher fuel temperatures take place between 5 and 10 μm for.

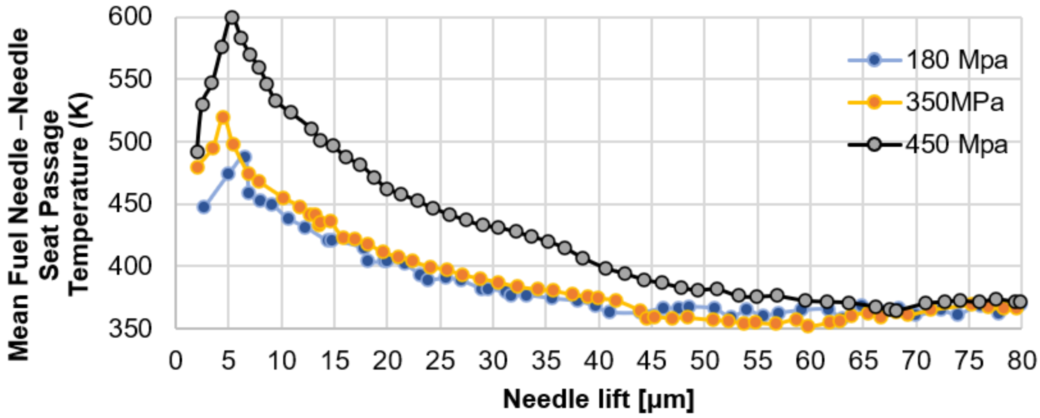

Figure 4. 13. Temporal evolution of fuel temperature at the needle- needle seat passage; lift increase from 0 μm to 80 μm during the plotted time.

- Fuel cooling process due to the "Joule-Thomson effect":

The comparison between the temporal evolution of fuel temperature at the exit of the injector's orifice and at the sac volume entrance reveals that the temperature profiles show different trends even for the same injection pressure. An increase in temperature is observed, particularly during the needle early opening, 0 – 15 μm, where an increase up to ~80, ~110 and ~180 degrees is estimated for the 180, 350 and 450 injection pressures, respectively. This pattern after the needle seat passage may be caused by the presence of the cooling effect for all the cases after that 60 μm lift.

Appendix 3. PC-SAFT parameters for thermodynamic & thermophysical properties.

-SAFT parameters

	m (-)	*σ* (Å)	*ε*/*k*$_B$ (K)
n-octadecane	7.438	3.948	254.90
n-hexadecane	6.669	3.944	253.59
heptamethylnonane	5.603	4.164	266.46
1-methylnaphthalene	3.422	3.901	337.14
1,2,3,4-tetrahydronaphthalene	3.088	3.996	337.46
trans-decalin	3.291	4.067	307.98
n-butylcyclohexane	3.682	4.036	282.41
1,2,4-trimethylbenzene	3.610	3.749	284.25

Table A.1. PC-SAFT parameters used in this study

Ideal gas coefficients

	A	*B*	*C*	*D*	*ΔH$_{ref}$* *[kJ/kg]*

n-octadecane	-13.474	1.71384	$-9.554*10^{-4}$	$2.03*10^{-7}$	-414.83
n-hexadecane	-11.656	1.52384	$-8.466*10^{-4}$	$1.792*10^{-7}$	-373.59
heptamethylnonane	-86.757	1.90728	$-1.3652*10^{-3}$	$3.944*10^{-7}$	-405.10
1-methylnaphthalene	-58.16	0.90672	$-6.7548*10^{-4}$	$2.014*10^{-7}$	116.94
1,2,3,4-tetrahydronaphthalene	-87.11	0.9832	$-7.1356*10^{-4}$	$2.06*10^{-7}$	27.63
trans-decalin	-127.17	1.2172	$-7.75*10^{-4}$	$1.868*10^{-7}$	-182.42
n-butylcyclohexane	-71.807	1.07592	$-6.012*10^{-4}$	$1.174*10^{-7}$	-213.32
1,2,4-trimethylbenzene	-10.6	0.66096	$-3.6292*10^{-4}$	$7.16*10^{-8}$	-13.94

Table A.2. Ideal gas parameters used during the calculation of properties

Entropy scaling parameters for viscosity

	A^{μ}	B^{μ}	C^{μ}	D^{μ}
n-octadecane	-0.94240	-4.2086	-0.92723	-0.2241
n-hexadecane	-0.89303	-3.9704	-0.84192	-0.1992
heptamethylnonane	-0.57516	-3.2643	-0.75823	-0.1992
1-methylnaphthalene	-0.59115	-2.7895	-0.58370	-0.1370
1,2,3,4-tetrahydronaphthalene	-0.50055	-2.6232	-0.44389	-0.1245
trans-decalin	-0.29640	-2.5604	-0.24863	-0.1245
n-butylcyclohexane	-0.58564	-2.8879	-0.41966	-0.1245
1,2,4-trimethylbenzene	-0.72078	-2.6213	-0.56599	-0.1121

Table A.3. Entropy Scaling parameters used for the calculation of viscosity.

Entropy scaling parameters for thermal conductivity

	A^{λ}	B^{λ}	C^{λ}	D^{λ}
n-octadecane	0	-0.40156	1.98005	0
n-hexadecane	0.36701	-0.52738	1.15300	0
heptamethylnonane	0.36701	-0.52738	1.15300	0
1-methylnaphthalene	0.51308	-0.57468	0.67839	-0.06761
1,2,3,4-tetrahydronaphthalene	0.51308	-0.57468	0.67839	-0.06761
trans-decalin	0.51308	-0.57468	0.67839	-0.06761
n-butylcyclohexane	0.51308	-0.57468	0.67839	-0.06761
1,2,4-trimethylbenzene	0	-0.45935	1.44014	0

Table A.4. Entropy Scaling parameters used for the calculation of thermal conductivity.

Bibliography

[1] E. Dons, L. Int Panis, M. Van Poppel, J. Theunis, H. Willems, R. Torfs, G. Wets, Impact of time-activity patterns on personal exposure to black carbon, Atmos. Environ. 45 (2011) 3594–3602. https://doi.org/10.1016/j.atmosenv.2011.03.064.

[2] J. Hansen, P. Kharecha, M. Sato, V. Masson-Delmotte, F. Ackerman, D.J. Beerling, P.J. Hearty, O. Hoegh-Guldberg, S.-L. Hsu, C. Parmesan, J. Rockstrom, E.J. Rohling, J. Sachs, P. Smith, K. Steffen, L.V. Susteren, K. von Schuckmann, J.C. Zachos, Assessing “Dangerous Climate Change”: Required Reduction of Carbon Emissions to Protect Young People, Future Generations and Nature, PLOS ONE. 8 (2013) e81648. https://doi.org/10.1371/journal.pone.0081648.

[3] 2019-Outlook-for-Energy_v4.pdf, (n.d.). https://corporate.exxonmobil.com/-/media/Global/Files/outlook-for-energy/2019-Outlook-for-Energy_v4.pdf (accessed January 13, 2021).

[4] G. Strotos, P. Koukouvinis, A. Theodorakakos, M. Gavaises, G. Bergeles, Transient heating effects in high pressure Diesel injector nozzles, Int. J. Heat Fluid Flow. 51 (2015) 257–267. https://doi.org/10.1016/j.ijheatfluidflow.2014.10.010.

[5] R. Lin, L.L. Tavlarides, Thermophysical properties needed for the development of the supercritical diesel combustion technology: Evaluation of diesel fuel surrogate models, J. Supercrit. Fluids. 71 (2012) 136–146. https://doi.org/10.1016/j.supflu.2012.08.003.

[6] G. Anitescu, T.J. Bruno, L.L. Tavlarides, Dieseline for Supercritical Injection and Combustion in Compression-Ignition Engines: Volatility, Phase Transitions, Spray/Jet Structure, and Thermal Stability, Energy Fuels. 26 (2012) 6247–6258. https://doi.org/10.1021/ef301060g.

[7] G. Anitescu, T.J. Bruno, Biodiesel Fuels from Supercritical Fluid Processing: Quality Evaluation with the Advanced Distillation Curve Method and Cetane Numbers, Energy Fuels. 26 (2012) 5256–5264. https://doi.org/10.1021/ef300615r.

[8] G. Anitescu, A. Deshpande, L.L. Tavlarides, Integrated Technology for Supercritical Biodiesel Production and Power Cogeneration, Energy Fuels. 22 (2008) 1391–1399. https://doi.org/10.1021/ef700727p.

[9] X. Wang, Z. Huang, O.A. Kuti, W. Zhang, K. Nishida, Experimental and analytical study on biodiesel and diesel spray characteristics under ultra-high injection pressure, Int. J. Heat Fluid Flow. 31 (2010) 659–666. https://doi.org/10.1016/j.ijheatfluidflow.2010.03.006.

[10] A. Theodorakakos, G. Strotos, N. Mitroglou, C. Atkin, M. Gavaises, Friction-induced heating in nozzle hole micro-channels under extreme fuel pressurisation, Fuel. 123 (2014) 143–150. https://doi.org/10.1016/j.fuel.2014.01.050.

[11] N. Mitroglou, M. Lorenzi, M. Santini, M. Gavaises, Application of X-ray micro-computed tomography on high-speed cavitating diesel fuel flows, Exp. Fluids. 57 (2016) 175. https://doi.org/10.1007/s00348-016-2256-z.

[12] A. Andriotis, M. Gavaises, C. Arcoumanis, Vortex flow and cavitation in diesel injector nozzles, J. Fluid Mech. 610 (2008) 195–215. https://doi.org/10.1017/S0022112008002668.

[13] M. Lorenzi, N. Mitroglou, M. Santini, M. Gavaises, Novel experimental technique for 3D investigation of high-speed cavitating diesel fuel flows by X-ray micro computed tomography, Rev. Sci. Instrum. 88 (2017) 033–706. https://doi.org/10.1063/1.4978795.

[14] M. Gavaises, A. Andriotis, D. Papoulias, N. Mitroglou, A. Theodorakakos, Characterization of string cavitation in large-scale Diesel nozzles with tapered holes, Phys. Fluids. 21 (2009) 052–107. https://doi.org/10.1063/1.3140940.

[15] H. Roth, E. Giannadakis, M. Gavaises, C. Arcoumanis, K. Omae, I. Sakata, M. Nakamura, H. Yanagihara, Effect of Multi-Injection Strategy on Cavitation Development in Diesel Injector Nozzle Holes, SAE International, 2005. https://doi.org/10.4271/2005-01-1237.

[16] D. Bauer, H. Chaves, C. Arcoumanis, Measurements of void fraction distribution in cavitating pipe flow using x-ray CT, Meas. Sci. Technol. 23 (2012) 055–302. https://doi.org/10.1088/0957-0233/23/5/055302.

[17] T. Sun, Z. Jiang, J. Strzalka, L. Ocola, J. Wang, Three-dimensional coherent X-ray surface scattering imaging near total external reflection, Nat. Photonics. 6 (2012) 586–590. https://doi.org/10.1038/nphoton.2012.178.

[18] A. Cooper, A. Stodart, D. Hancock, S. Duke, J. Miller, S. Reader, Development of Two New High Specific Output 3 Cylinder Engines for the Global Market with Capacities of 1.2l and 1.5l, SAE International, 2019. https://doi.org/10.4271/2019-01-1193.

[19] A. Kastengren, F. Tilocco, D. Duke, C. Powell, S. Moon, X. Zhang, Time-Resolved X-Ray Radiography of Sprays from Engine Combustion Network Spray A Diesel Injectors, At. Sprays. 24 (2013) 251–272. https://doi.org/10.1615/AtomizSpr.2013008642.

[20] H. Watanabe, M. Nishikori, T. Hayashi, M. Suzuki, N. Kakehashi, M. Ikemoto, Visualization analysis of relationship between vortex flow and cavitation behavior in diesel nozzle, Int. J. Engine Res. 16 (2015) 5–12. https://doi.org/10.1177/1468087414562459.

[21] N. Mitroglou, M. Gavaises, J. Nouri, C. Arcoumanis, Cavitation inside enlarged and real-size fully transparent injector nozzles and its effect on near nozzle spray formation, (2011).

[22] H. Chaves, M. Knapp, A. Kubitzek, F. Obermeier, T. Schneider, Experimental Study of Cavitation in the Nozzle Hole of Diesel Injectors Using Transparent Nozzles, SAE International, 1995. https://doi.org/10.4271/950290.

[23] C. Arcoumanis, M. Gavaises, H. Flora, H. Roth, Visualisation of cavitation in diesel engine injectors, Mécanique Ind. 2 (2001) 375–381. https://www.sciencedirect.com/science/article/pii/S1296213901011198.

[24] C. Badock, R. Wirth, A. Fath, A. Leipertz, Investigation of cavitation in real size diesel injection nozzles, Int. J. Heat Fluid Flow. 20 (1999) 538–544. https://doi.org/10.1016/S0142-727X(99)00043-0.

[25] B. Chehroudi, D. Talley, E. Coy, Visual characteristics and initial growth rates of round cryogenic jets at subcritical and supercritical pressures, Phys. Fluids - PHYS FLUIDS. 14 (2002) 850–861. https://doi.org/10.1063/1.1430735.

[26] A. Prosperetti, Y. Hao, Modelling of spherical gas bubble oscillations and sonoluminescence, Philos. Trans. R. Soc. Lond. Ser. Math. Phys. Eng. Sci. 357 (1999) 203–223. https://doi.org/10.1098/rsta.1999.0324.

[27] G.J. Ball, B.P. Howell, T.G. Leighton, M.J. Schofield, Shock-induced collapse of a cylindrical air cavity in water: a Free-Lagrange simulation, Shock Waves. 10 (2000) 265–276. https://doi.org/10.1007/s001930000060.

[28] R.R. Nourgaliev, N. Dinh, T. Theofanous, Adaptive Characteristics -Based Matching for Compressible Multifluid Dynamics, J. Comput. Phys. 213 (2006) 500–529. https://doi.org/10.1016/j.jcp.2005.08.028.

[29] C.-H. Chang, M. Liou, A robust and accurate approach to computing compressible multiphase flow: Stratified flow model and AUSM+-up scheme, J. Comput. Phys. 225 (2007) 840–873. https://doi.org/10.1016/j.jcp.2007.01.007.

[30] C.K. Turangan, A.R. Jamaluddin, G.J. Ball, T.G. Leighton, Free-Lagrange simulations of the expansion and jetting collapse of air bubbles in water, J. Fluid Mech. 598 (2008) 1–25. https://doi.org/10.1017/S0022112007009317.

[31] R.F. Kunz, D.A. Boger, D.R. Stinebring, T.S. Chyczewski, J.W. Lindau, H.J. Gibeling, S. Venkateswaran, T.R. Govindan, A preconditioned Navier-Stokes method for two-phase flows with application to cavitation prediction, Comput. Fluids. 29 (2000) 849–875. https://doi.org/10.1016/S0045-7930(99)00039-0.

[32] I. Senocak, W. Shyy, A Pressure-Based Method for Turbulent Cavitating Flow Computations, J. Comput. Phys. 176 (2002) 363–383. https://doi.org/10.1006/jcph.2002.6992.

[33] G. Schnerr Professor Dr.-Ing.habil, Physical and Numerical Modeling of Unsteady Cavitation Dynamics, in: 4th International Conference on Multiphase Flow, 2001. https://www.researchgate.net/publication/296196752_Physical_and_Numerical_Modeling_of_Unsteady_Cavitation_Dynamics.

[34] A.K. Singhal, M.M. Athavale, H. Li, Y. Jiang, Mathematical Basis and Validation of the Full Cavitation Model, J. Fluids Eng. 124 (2002) 617–624. https://doi.org/10.1115/1.1486223.

[35] A. Kubota, H. Kato, H. Yamaguchi, A new modelling of cavitating flows: a numerical study of unsteady cavitation on a hydrofoil section, J. Fluid Mech. 240 (1992) 59–96. https://doi.org/10.1017/S002211209200003X.

[36] E. Giannadakis, M. Gavaises, C. Arcoumanis, Modelling of cavitation in diesel injector nozzles, J. Fluid Mech. 616 (2008) 153–193. https://doi.org/10.1017/S0022112008003777.

[37] B. Huang, G. Wang, H. Yuan, A cavitation model for cavtating flow simulations, J. Hydrodyn. 22 (2010) 756–762. https://doi.org/10.1016/S1001-6058(10)60033-9.

[38] Y. Tamura, Y. Matsumoto, A New Algorithm for Cavitating Flow Simulations Based on the Bubble Dynamics, in: S.W. Armfield, P. Morgan, K. Srinivas (Eds.), Comput. Fluid Dyn. 2002, Springer, Berlin, Heidelberg, 2003: pp. 535–540. https://doi.org/10.1007/978-3-642-59334-5_80.

[39] N.A. Adams, S.J. Schmidt, Shocks in Cavitating Flows, in: C.F. Delale (Ed.), Bubble Dyn. Shock Waves, Springer, 2013: pp. 235–256. https://doi.org/10.1007/978-3-642-34297-4_8.

[40] D. van der Heul, C. Vuik, P. Wesseling, Efficient computation of flow with cavitation by compressible pressure correction, (2000) 1–6. https://research.tudelft.nl/en/publications/efficient-computation-of-flow-with-cavitation-by-compressible-pre.

[41] H. Guillard, C. Viozat, On the behaviour of upwind schemes in the low Mach number limit, Comput. Fluids. 28 (1999) 63–86. https://doi.org/10.1016/S0045-7930(98)00017-6.

[42] A. Meister, Asymptotic Single and Multiple Scale Expansions in the Low Mach Number Limit, Siam J Appl Math. 60 (1998) 256–271. https://www.jstor.org/stable/118479.

[43] C.-D. Munz, S. Roller, R. Klein, K.J. Geratz, The extension of incompressible flow solvers to the weakly compressible regime, Comput. Fluids. 32 (2003) 173–196. https://doi.org/10.1016/S0045-7930(02)00010-5.

[44] N. Mitroglou, M. Gavaises, Mapping of cavitating flow regimes in injectors for medium-/heavy-duty diesel engines, Int. J. Engine Res. 14 (2013) 590–605. https://doi.org/10.1177/1468087413500491.

[45] Multiphase Lattice Boltzmann Methods: Theory and Application | Wiley, Wiley.Com. (n.d.). https://www.wiley.com/en-us/Multiphase+Lattice+Boltzmann+Methods%3A+Theory+and+Application-p-9781118971338 (accessed March 17, 2021).

[46] G.R. Liu, M.B. Liu, Smoothed Particle Hydrodynamics: A Meshfree Particle Method, 2003. https://doi.org/10.1142/5340.

[47] L.B. Lucy, A numerical approach to the testing of the fission hypothesis, Astron. J. 82 (1977) 1013–1024. https://doi.org/10.1086/112164.

[48] R.A. Gingold, J.J. Monaghan, Smoothed particle hydrodynamics - Theory and application to non-spherical stars, Mon. Not. R. Astron. Soc. 181 (1977) 375–389. https://doi.org/10.1093/mnras/181.3.375.

[49] J.J. Monaghan, Simulating Free Surface Flows with SPH, J. Comput. Phys. 110 (1994) 399–406. https://doi.org/10.1006/jcph.1994.1034.

[50] A. Colagrossi, M. Landrini, Numerical Simulation of Interfacial Flows by Smoothed Particle Hydrodynamics, J. Comput. Phys. 191 (2003) 448–475. https://doi.org/10.1016/S0021-9991(03)00324-3.

[51] N. Grenier, M. Antuono, A. Colagrossi, D. Le Touzé, B. Alessandrini, An Hamiltonian interface SPH formulation for multi-fluid and free surface flows, J. Comput. Phys. 228 (2009) 8380–8393. https://doi.org/10.1016/j.jcp.2009.08.009.

[52] J.P. Vila, On particle weighted methods and SPH, Math. Models Methods Appl. Sci. - M3AS. 09 (1999) 161–209. https://doi.org/10.1142/S0218202599000117.

[53] J.-C. Marongiu, F. Leboeuf, J. Caro, E. Parkinson, Free surface flows simulations in Pelton turbines using an hybrid SPH-ALE method, J. Hydraul. Res. 48 (2010) 40–49. https://doi.org/10.1080/00221686.2010.9641244.

[54] G.B. Wallis, Critical two-phase flow, Int. J. Multiph. Flow. 6 (1980) 97–112. https://doi.org/10.1016/0301-9322(80)90041-5.

[55] M.R. Baer, J.W. Nunziato, A two-phase mixture theory for the deflagration-to-detonation transition (ddt) in reactive granular materials, Int. J. Multiph. Flow. 12 (1986) 861–889. https://doi.org/10.1016/0301-9322(86)90033-9.

[56] R. Saurel, R. Abgrall, A Multiphase Godunov Method for Compressible Multifluid and Multiphase Flows, J. Comput. Phys. 150 (1999) 425–467. https://doi.org/10.1006/jcph.1999.6187.

[57] F.H. Harlow, The particle-in-cell method for numerical solution of problems in fluid dynamics, Los Alamos National Lab, 1962. https://doi.org/10.2172/4769185.

[58] F.H. Harlow, J.E. Welch, Numerical Calculation of Time-Dependent Viscous Incompressible Flow of Fluid with Free Surface, Phys. Fluids. 8 (1965) 2182–2189. https://doi.org/10.1063/1.1761178.

[59] M.S. Plesset, R.B. Chapman, Collapse of an initially spherical vapour cavity in the neighbourhood of a solid boundary, J. Fluid Mech. 47 (1971) 283–290. https://doi.org/10.1017/S0022112071001058.

[60] S.O. Unverdi, G. Tryggvason, A front-tracking method for viscous, incompressible, multi-fluid flows, J. Comput. Phys. 100 (1992) 25–37. https://doi.org/10.1016/0021-9991(92)90307-K.

[61] P. Koukouvinis, N. Kyriazis, M. Gavaises, Smoothed particle hydrodynamics simulation of a laser pulse impact onto a liquid metal droplet, PLOS ONE. 13 (2018) e0204125. https://doi.org/10.1371/journal.pone.0204125.

[62] C.S. Peskin, The immersed boundary method, Acta Numer. 11 (2002) 479–517. https://doi.org/10.1017/S0962492902000077.

[63] F. Örley, V. Pasquariello, S. Hickel, N.A. Adams, Cut-element based immersed boundary method for moving geometries in compressible liquid flows with cavitation, J. Comput. Phys. C (2015) 1–22. https://doi.org/10.1016/j.jcp.2014.11.028.

[64] C.W. Hirt, B.D. Nichols, Volume of fluid (VOF) method for the dynamics of free boundaries, J Comput Phys U. S. 39:1 (1981) 587–612. https://doi.org/10.1016/0021-9991(81)90145-5.

[65] S. Osher, J.A. Sethian, Fronts propagating with curvature-dependent speed: Algorithms based on Hamilton-Jacobi formulations, J. Comput. Phys. 79 (1988) 12–49. https://doi.org/10.1016/0021-9991(88)90002-2.

[66] S. Osher, R. Fedkiw, Level Set Methods and Dynamic Implicit Surfaces, Springer-Verlag, New York, 2003. https://doi.org/10.1007/b98879.

[67] D. Youngs, An interface tracking method for a 3D Eulerian hydrodynamics code, AWRE. Technical Report 44/92/ 35 (1984).

[68] M. Rudman, Volume-Tracking Methods for Interfacial Flow Calculations, Int. J. Numer. Methods Fluids. 24 (1997) 671–691. https://doi.org/10.1002/(SICI)1097-0363(19970415)24:7<671::AID-FLD508>3.0.CO;2-9.

[69] M.L. Norman, K.H.A. Winkler, 2-D Eulerian hydrodynamics with fluid interfaces, self-gravity and rotation, (1982). https://digital.library.unt.edu/ark:/67531/metadc1208876/.

[70] E.G. Puckett, J.S. Saltzman, A 3D adaptive mesh refinement algorithm for multimaterial gas dynamics, Phys. Nonlinear Phenom. 60 (1992) 84–93. https://doi.org/10.1016/0167-2789(92)90228-F.

[71] G.H. Miller, E.G. Puckett, A High-Order Godunov Method for Multiple Condensed Phases, J. Comput. Phys. 128 (1996) 134–164. https://doi.org/10.1006/jcph.1996.0200.

[72] R. Saurel, R. Abgrall, A Simple Method for Compressible Multifluid Flows, SIAM J. Sci. Comput. 21 (1999) 1115–1145. https://doi.org/10.1137/S1064827597323749.

[73] R.K. Shukla, C. Pantano, J.B. Freund, An interface capturing method for the simulation of multi-phase compressible flows, J. Comput. Phys. 229 (2010) 7411–7439. https://doi.org/10.1016/j.jcp.2010.06.025.

[74] D.P. Garrick, W.A. Hagen, J.D. Regele, An interface capturing scheme for modeling atomization in compressible flows, J. Comput. Phys. 344 (2017) 260–280. https://doi.org/10.1016/j.jcp.2017.04.079.

[75] J. Roenby, H. Bredmose, H. Jasak, A computational method for sharp interface advection, R. Soc. Open Sci. 3 (2016) 25. https://doi.org/10.1098/rsos.160405.

[76] S. Popinet, Gerris: a tree-based adaptive solver for the incompressible Euler equations in complex geometries, J. Comput. Phys. 190 (2003) 572–600. https://doi.org/10.1016/S0021-9991(03)00298-5.

[77] P. Zwart, A.G. Gerber, T. Belamri, A two-phase flow model for predicting cavitation dynamics, Fifth Int. Conf. Multiph. Flow. (2004).

[78] C. Merkle, J. Feng, P.E.O. Buelow, Computational modeling of the dynamics of sheet cavitation, Undefined. (1998). /paper/Computational-modeling-of-the-dynamics-of-sheet-Merkle-Feng/b831c2eacef7ed689509fcafb86372699778e986.

[79] Y. Dellanoy, J. Kueny, Two phase flow approach in unsteady cavitation modeling, Undefined. (1990). https://www.semanticscholar.org/author/Yves-Dellanoy/102094289.

[80] B. Stutz, Two-phase flow structure of cavitation: Experiment and modeling of unsteady effects, (n.d.). https://www.academia.edu/20331444/Two_phase_flow_structure_of_cavitation_Experiment_and_modeling_of_unsteady_effects?auto=download.

[81] H.W.M. Hoeijmakers, M.E. Janssens, W.H. Kwan, Numerical Simulation of Sheet Cavitation, in: Proc. 3rd Int. Symp. Cavitation April 7-10 1998 Grenoble Fr., 1998: pp. 257–262. https://research.utwente.nl/en/publications/numerical-simulation-of-sheet-cavitation (accessed March 20, 2021).

[82] C.P. Egerer, S. Hickel, S.J. Schmidt, N.A. Adams, Large-eddy simulation of turbulent cavitating flow in a micro channel, Phys. Fluids. 26 (2014) 085102. https://doi.org/10.1063/1.4891325.

[83] P. Koukouvinis, M. Gavaises, A. Georgoulas, M. Marengo, Compressible simulations of bubble dynamics with central-upwind schemes, 30 (2016) 129–140. https://doi.org/10.1080/10618562.2016.1166216.

[84] F. Örley, T. Trummler, S. Hickel, M.S. Mihatsch, S.J. Schmidt, N.A. Adams, Large-eddy simulation of cavitating nozzle flow and primary jet break-up, Phys. Fluids. 27 (2015) 086–101. https://doi.org/10.1063/1.4928701.

[85] R. Saurel, P. Cocchi, P.B. Butler, Numerical Study of Cavitation in the Wake of a Hypervelocity Underwater Projectile, J. Propuls. Power. 15 (1999) 513–522. https://doi.org/10.2514/2.5473.

[86] G.H. Schnerr, I.H. Sezal, S.J. Schmidt, Numerical investigation of three-dimensional cloud cavitation with special emphasis on collapse induced shock dynamics, Phys. Fluids. 20 (2008) 040–703. https://doi.org/10.1063/1.2911039.

[87] S. Schmidt, I. Sezal, G. Schnerr, M. Talhamer, Riemann Techniques for the Simulation of Compressible Liquid Flows with Phase-Transistion at all Mach Numbers - Shock and Wave Dynamics in Cavitating 3-D Micro and Macro Systems, in: 46th AIAA Aerosp. Sci. Meet. Exhib., American Institute of Aeronautics and Astronautics, n.d. https://doi.org/10.2514/6.2008-1238.

[88] I.H. Sezal, S.J. Schmidt, G.H. Schnerr, M. Thalhamer, M. Förster, Shock and wave dynamics in cavitating compressible liquid flows in injection nozzles, Shock Waves. 19 (2009) 49–58. https://doi.org/10.1007/s00193-008-0185-3.

[89] M. Dumbser, U. Iben, C.-D. Munz, Efficient implementation of high order unstructured WENO schemes for cavitating flows, Comput. Fluids. (2013) 141–168. https://doi.org/10.1016/j.compfluid.2013.07.011.

[90] N. Kyriazis, P. Koukouvinis, M. Gavaises, Numerical investigation of bubble dynamics using tabulated data, Int. J. Multiph. Flow. 93 (2017) 158–177. https://doi.org/10.1016/j.ijmultiphaseflow.2017.04.004.

[91] R. Skoda, U. Iben, R. Bosch, A. Morozov, H.-L. Platz, M. Mihatsch, S. Schmidt, N. Adams, Numerical simulation of collapse induced shock dynamics for the prediction of the geometry, pressure and temperature impact on the cavitation erosion in micro channels, Undefined. (2011). https://doi.org/DOI: 10.13140/2.1.2676.9287.

[92] M.S. Mihatsch, S.J. Schmidt, N.A. Adams, Cavitation erosion prediction based on analysis of flow dynamics and impact load spectra, Phys. Fluids. 27 (2015) 103–302. https://doi.org/Https://doi.org/10.1063/1.4932175.

[93] S. Yang, P. Yi, C. Habchi, Real-fluid injection modeling and LES simulation of the ECN Spray A injector using a fully compressible two-phase flow approach, Int. J. Multiph. Flow. 122 (2020) 103–145. https://doi.org/10.1016/j.ijmultiphaseflow.2019.103145.

[94] S. Yang, C. Habchi, P. Yi, R. Lugo, Cavitation Modelling Using Real-Fluid Equation of State, ASME Press. (2018) 6. https://doi.org/10.1115/1.861851_ch44.

[95] M. Dular, O. Coutier-Delgosha, Numerical Modelling of Cavitation Erosion, Int. J. Numer. Methods Fluids. 61 (2009) 1388–1410. https://doi.org/10.1002/fld.2003.

[96] J. Decaix, E. Goncalvès Da Silva, Compressible effects modelling in turbulent cavitating flows, Eur. J. Mech. - BFluids. 39 (2013) 11–31. https://doi.org/10.1016/j.euromechflu.2012.12.001.

[97] P. Koukouvinis, M. Gavaises, Simulation of throttle flow with two phase and single phase homogenous equilibrium model, J. Phys. Conf. Ser. 656 (2015) 012–086. https://doi.org/10.1088/1742-6596/656/1/012086.

[98] G. Schnerr Professor Dr.-Ing.habil, S. Schmidt, I. Sezal, M. Thalhamer, Shock and wave dynamics in compressible liquid flows with emphasis on unsteady load on hydrofoils and on cavitation in injection nozzles, in: 2006. https://research.utwente.nl/en/publications/shock-and-wave-dynamics-in-compressible-liquid-flows-with-emphasi.

[99] F.J. Salvador, J.-V. Romero, M.-D. Roselló, J. Martínez-López, Validation of a code for modeling cavitation phenomena in Diesel injector nozzles, Math. Comput. Model. 52 (2010) 1123–1132. https://doi.org/10.1016/j.mcm.2010.02.027.

[100] S. Molina, F.J. Salvador Rubio, M. Carreres Talens, D. Jaramillo, A computational investigation on the influence of the use of elliptical orifices on the inner nozzle flow and cavitation development in diesel injector nozzles, in: Energy Convers. Manag., Elsevier, 2014: pp. 114–127. https://doi.org/10.1016/j.enconman.2013.12.015.

[101] F.J. Salvador, J. Martínez-López, J.-V. Romero, M.-D. Roselló, Computational study of the cavitation phenomenon and its interaction with the turbulence developed in diesel injector nozzles by Large Eddy Simulation (LES), Math. Comput. Model. 57 (2013) 1656–1662. https://doi.org/10.1016/j.mcm.2011.10.050.

[102] K. Neroorkar, B. Shields, J. Ronald O. Grover, A.P. Torres, D. Schmidt, Application of the Homogeneous Relaxation Model to Simulating Cavitating Flow of a Diesel Fuel, SAE International, Warrendale, PA, 2012. https://doi.org/10.4271/2012-01-1269.

[103] M. Battistoni, S. Som, C.F. Powell, Highly resolved Eulerian simulations of fuel spray transients in single and multi-hole injectors: Nozzle flow and near-exit dynamics, Fuel. 251 (2019) 709–729. https://doi.org/10.1016/j.fuel.2019.04.076.

[104] R. Balz, I.G. Nagy, G. Weisser, D. Sedarsky, Experimental and numerical investigation of cavitation in marine Diesel injectors, Int. J. Heat Mass Transf. 169 (2021) 120933. https://doi.org/10.1016/j.ijheatmasstransfer.2021.120933.

[105] G.M. Magnotti, M. Battistoni, K. Saha, S. Som, Development and validation of the cavitation-induced erosion risk assessment tool, Transp. Eng. 2 (2020) 100034. https://doi.org/10.1016/j.treng.2020.100034.

[106] Q. Xue, M. Battistoni, C.F. Powell, D.E. Longman, S.P. Quan, E. Pomraning, P.K. Senecal, D.P. Schmidt, S. Som, An Eulerian CFD model and X-ray radiography for coupled nozzle flow and spray in internal combustion engines, Int. J. Multiph. Flow. 70 (2015) 77–88. https://doi.org/10.1016/j.ijmultiphaseflow.2014.11.012.

[107] S. Yang, C. Habchi, Real-fluid phase transition in cavitation modeling considering dissolved non-condensable gas, Phys. Fluids. 32 (2020) 032102. https://doi.org/10.1063/1.5140981.

[108] C. Habchi, A Gibbs free Energy Relaxation Model for Cavitation Simulation in Diesel injectors, ILASS – Europe 2013, 25th European Conference on Liquid Atomization and Spray Systems, Chania, Greece, 1-4 September, 2013.

[109] E. Ghahramani, M.H. Arabnejad, R.E. Bensow, A comparative study between numerical methods in simulation of cavitating bubbles, Int. J. Multiph. Flow. 111 (2019) 339–359. https://doi.org/10.1016/j.ijmultiphaseflow.2018.10.010.

[110] P. Yi, S. Yang, C. Habchi, R. Lugo, A multicomponent real-fluid fully compressible four-equation model for two-phase flow with phase change, Phys. Fluids. 31 (2019) 026102. https://doi.org/10.1063/1.5065781.

[111] P. Koukouvinis, M. Gavaises, J. Li, L. Wang, Large Eddy Simulation of Diesel injector including cavitation effects and correlation to erosion damage, Fuel. 175 (2016) 026–039. https://doi.org/10.1016/j.fuel.2016.02.037.

[112] B. M Devassy, V. Caika, P. Sampl, W. Edelbauer, D. Greif, Numerical Investigation of Cavitating Injector Flow Accounting for 3D-Needle Movement and Liquid Compressibility Effects, in: 2015: p. 012092. https://doi.org/10.1088/1742-6596/656/1/012092.

[113] B. M Devassy, D. Greif, W. Edelbauer, Study of Cavitation and 3D Needle Movement due to Erosion in Fuel Injection Nozzles Using Coupled Simulation Tools, in: ILASS-Asia 2016 18th Annu. Conf. Liq. At. Spray Syst. - Asia Chennai India, 2016.

[114] M. Battistoni, C.N. Grimaldi, Numerical analysis of injector flow and spray characteristics from diesel injectors using fossil and biodiesel fuels, Appl. Energy. 97 (2012) 656–666. https://doi.org/10.1016/j.apenergy.2011.11.080.

[115] Z. He, W. Zhong, Q. Wang, Z. Jiang, Y. Fu, An investigation of transient nature of the cavitating flow in injector nozzles, Appl. Therm. Eng. 1 (2013) 56–64. https://doi.org/10.1016/j.applthermaleng.2013.01.024.

[116] X. Margot, S. Hoyas, P. Fajardo, S. Patouna, A moving mesh generation strategy for solving an injector internal flow problem, Math. Comput. Model. 52 (2010) 1143–1150. https://doi.org/10.1016/j.mcm.2010.03.018.

[117] J. Martínez Rubio, F. Piscaglia, A. Montorfano, A. Onorati, S.M. Aithal, Influence of spatial discretization schemes on accuracy of explicit LES: Canonical problems to engine-like geometries, Comput. Fluids. 117 (2015) 62–78. https://doi.org/10.1016/j.compfluid.2015.05.007.

[118] J. Martínez, F. Piscaglia, A. Montorfano, A. Onorati, S.M. Aithal, Influence of momentum interpolation methods on the accuracy and convergence of pressure-velocity coupling algorithms in OpenFOAM, J. Comput. Appl. Math. 309 (2017) 654–673. https://doi.org/10.1016/j.cam.2016.03.037.

[119] F. Giussani, A. Montorfano, F. Piscaglia, A. Onorati, J. Helie, VOF Simulation of The Cavitating Flow in High Pressure GDI Injectors, in: Proc. ILASS–Europe 2017 28th Conf. Liq. At. Spray Syst., Universitat Politècnica València, 2017. https://doi.org/10.4995/ILASS2017.2017.4989.

[120] F. Giussani, A. Montorfano, F. Piscaglia, A. Onorati, J. Helie, S.M. Aithal, Dynamic VOF Modelling of the Internal Flow in GDI Fuel Injectors, Energy Procedia. 101 (2016) 574–581. https://doi.org/10.1016/j.egypro.2016.11.073.

[121] Y. Wu, A. Montorfano, F. Piscaglia, A. Onorati, A Study of the Organized in-Cylinder Motion by a Dynamic Adaptive Scale-Resolving Turbulence Model, Flow Turbul. Combust. 100 (2018) 797–827. https://doi.org/10.1007/s10494-017-9881-3.

[122] F. Oerley, S. Hickel, S. Schmidt, N. Adams, Large-Eddy Simulation of turbulent, cavitating fuel flow inside a 9-hole Diesel injector including needle movement, Int. J. Engine Res. 18 (2016) 195–211. https://doi.org/10.1177/1468087416643901.

[123] E. Stavropoulos Vasilakis, N. Kyriazis, P. Koukouvinis, M. Farhat, M. Gavaises, Cavitation induction by projectile impacting on a water jet, Int. J. Multiph. Flow. 114 (2019) 128–139. https://doi.org/10.1016/j.ijmultiphaseflow.2019.03.001.

[124] H. Zhang, J.-J. Tan, D.-M. Cui, Study and application of overset unstructured grid method, 27 (2010) 162–168. https://www.researchgate.net/publication/292558457.

[125] A. Khaware, V. Gupta, K. Srikanth, M. Azhar, Numerical Simulation of Cavitating Flows using Overset Mesh, in: 4 th World Congress on Momentum, Heat and Mass Transfer, 2019: p. 9. https://doi.org/10.11159/icmfht19.108.

[126] C.P. Koci, R.P. Fitzgerald, V. Ikonomou, K. Sun, The effects of fuel–air mixing and injector dribble on diesel unburned hydrocarbon emissions, Int. J. Engine Res. 20 (2019) 105–127. https://doi.org/10.1177/1468087418821827.

[127] C. Guventurk, M. Sahin, An arbitrary Lagrangian-Eulerian framework with exact mass conservation for the numerical simulation of 2D rising bubble problem, Int. J. Numer. Methods Eng. 112 (2017) 2110–2134. https://doi.org/10.1002/nme.5598.

[128] R.D. Reitz, H. Ogawa, R. Payri, T. Fansler, S. Kokjohn, Y. Moriyoshi, A.K. Agarwal, D. Arcoumanis, D. Assanis, C. Bae, K. Boulouchos, M. Canakci, S. Curran, I. Denbratt, M. Gavaises, M. Guenthner, C. Hasse, Z. Huang, T. Ishiyama, B. Johansson, T.V. Johnson, G. Kalghatgi, M. Koike, S.C. Kong, A. Leipertz, P. Miles, R. Novella, A. Onorati, M. Richter, S. Shuai, D. Siebers, W. Su, M. Trujillo, N. Uchida, B.M. Vaglieco, R.M. Wagner, H. Zhao, IJER editorial: The future of the internal combustion engine:, Int. J. Engine Res. (2019) 3–10. https://doi.org/10.1177/1468087419877990.

[129] L. Duan, S. Yuan, L. Hu, W. Yang, J. Yu, X. Xia, Injection performance and cavitation analysis of an advanced 250MPa common rail diesel injector, Int. J. Heat Mass Transf. 93 (2016) 388–397. https://doi.org/10.1016/j.ijheatmasstransfer.2015.10.028.

[130] W. Vera-Tudela, R. Haefeli, C. Barro, B. Schneider, K. Boulouchos, An experimental study of a very high-pressure diesel injector (up to 5000 bar) by means of optical diagnostics, Fuel. 275 (2020) 117–933. https://doi.org/10.1016/j.fuel.2020.117933.

[131] C.-D. Ohl, M. Arora, R. Dijkink, V. Janve, D. Lohse, Surface cleaning from laser-induced cavitation bubbles, Appl. Phys. Lett. 89 (2006) 074–102. https://doi.org/10.1063/1.2337506.

[132] G.L. Chahine, A. Kapahi, J.-K. Choi, C.-T. Hsiao, Modeling of surface cleaning by cavitation bubble dynamics and collapse, Ultrason. Sonochem. 29 (2016) 528–549. https://doi.org/10.1016/j.ultsonch.2015.04.026.

[133] P. Koukouvinis, G. Strotos, Q. Zeng, S. Gonzalez-Avila, A. Theodorakakos, M. Gavaises, C.-D. Ohl, Parametric Investigations of the Induced Shear Stress by a Laser-Generated Bubble, Langmuir. 34 (2018) 6428–6442. https://doi.org/10.1021/acs.langmuir.8b01274.

[134] Q. Zeng, S.R. Gonzalez-Avila, R. Dijkink, P. Koukouvinis, M. Gavaises, C.-D. Ohl, Wall shear stress from jetting cavitation bubbles, J. Fluid Mech. 846 (2018) 341–355. https://doi.org/10.1017/jfm.2018.286.

[135] R.D. Reitz, F.V. Bracco, Mechanism of atomization of a liquid jet, Phys. Fluids. 25 (1982) 1730–1742. https://doi.org/10.1063/1.863650.

[136] S.P. Lin, R.D. Reitz, Drop and Spray Formation from a Liquid Jet, Annu. Rev. Fluid Mech. 30 (1998) 85–105. https://doi.org/10.1146/annurev.fluid.30.1.85.

[137] N. Tamaki, M. Shimizu, Enhancement of Atomization of High Viscous Liquid Jet by Pressure Atomized Type Nozzle, Proc. Conf. Chugoku-Shikoku Branch. 2002.40 (2002) 167–168. https://doi.org/10.1299/jsmecs.2002.40.167.

[138] A. Sou, S. Hosokawa, A. Tomiyama, Effects of cavitation in a nozzle on liquid jet atomization, Int. J. Heat Mass Transf. 50 (2007) 3575–3582. https://doi.org/10.1016/j.ijheatmasstransfer.2006.12.033.

[139] M. Dular, B. Bachert, B. Stoffel, B. Širok, Relationship between cavitation structures and cavitation damage, Wear. 257 (2004) 1176–1184. https://doi.org/10.1016/j.wear.2004.08.004.

[140] L. Zhang, Z. He, W. Guan, Q. Wang, S. Som, Simulations on the cavitating flow and corresponding risk of erosion in diesel injector nozzles with double array holes, Int. J. Heat Mass Transf. 124 (2018) 900–911. https://doi.org/10.1016/j.ijheatmasstransfer.2018.03.086.

[141] O. Asi, Failure of a diesel engine injector nozzle by cavitation damage, Eng. Fail. Anal. 13 (2006) 1126–1133. https://doi.org/10.1016/j.engfailanal.2005.07.021.

[142] M. Brunhart, C. Soteriou, C. Daveau, M. Gavaises, P. Koukouvinis, M. Winterbourn, Cavitation erosion risk indicators for a thin gap within a diesel fuel pump, Wear. 442–443 (2020) 203–240. https://doi.org/10.1016/j.wear.2019.203024.

[143] I.K. Karathanassis, F. Koukouvinis, M. Gavaises, Multiphase Phenomena in Diesel Fuel Injection Systems, in: A.P. Singh, P.C. Shukla, J. Hwang, A.K. Agarwal (Eds.), Simul. Opt. Diagn. Intern. Combust. Engines Curr. Status Way Forw., Springer, 2020: pp. 95–126. https://doi.org/10.1007/978-981-15-0335-1_8.

[144] P. Koukouvinis, N. Mitroglou, M. Gavaises, M. Lorenzi, M. Santini, Quantitative predictions of cavitation presence and erosion-prone locations in a high-pressure cavitation test rig, J. Fluid Mech. 819 (2017) 21–57. https://doi.org/10.1017/jfm.2017.156.

[145] W. Bergwerk, Flow Pattern in Diesel Nozzle Spray Holes, Proc. Inst. Mech. Eng. 173 (1959) 655–660. https://doi.org/10.1243/PIME_PROC_1959_173_054_02.

[146] G. Guo, Z. He, Y. Chen, Q. Wang, X. Leng, S. Sun, LES investigations on effects of the residual bubble on the single hole diesel injector jet, Int. J. Heat Mass Transf. 112 (2017) 18–27. https://doi.org/10.1016/j.ijheatmasstransfer.2017.04.080.

[147] U. Iben, A. Morozov, E. Winklhofer, F. Wolf, Laser-pulse interferometry applied to high-pressure fluid flow in micro channels, Exp. Fluids. 50 (2010) 597–611. https://doi.org/10.1007/s00348-010-0950-9.

[148] C. Mauger, L. Méès, M. Michard, A. Azouzi, S. Valette, Shadowgraph, Schlieren and interferometry in a 2D cavitating channel flow, Exp. Fluids. 53 (2012) 1895–1913. https://doi.org/10.1007/s00348-012-1404-3.

[149] R.E.A. Arndt, Cavitation in vortical flows, Annu. Rev. Fluid Mech. 34 (2002) 143–175. https://doi.org/10.1146/annurev.fluid.34.082301.114957.

[150] E. Giannadakis, D. Papoulias, A. Theodorakakos, M. Gavaises, Simulation of cavitation in outward-opening piezo-type pintle injector nozzles:, Proc. Inst. Mech. Eng. Part J. Automob. Eng. (2008) 1895–1910. https://doi.org/10.1243/09544070JAUTO728.

[151] C. Arcoumanis, M. Gavaises, B. Argueyrolles, F. Galzin, Modeling of Pressure-Swirl Atomizers for GDI Engines, in: 1999: pp. 01–050. https://doi.org/10.4271/1999-01-0500.

[152] M. Gavaises, C. Arcoumanis, H. Roth, Y.S. Choi, A. Theodorakakos, Nozzle Flow and Spray Characteristics from VCO Diesel Injector Nozzles, in: J.H. Whitelaw, F. Payri, C. Arcoumanis, J.M. Desantes (Eds.), Thermo- Fluid Dyn. Process. Diesel Engines 2, Springer, 2004: pp. 31–48. https://doi.org/10.1007/978-3-662-10502-3_3.

[153] Manolis Gavaises, Foivos Koukouvinis, Martin Gold, Richard Pearson, Mithun Girija Murali, Numerical simulation of fuel dribbling and nozzle wall wetting, Int J. Engine Res. (2021) 001–018. https://doi.org/10.1177/1468087420985189.

[154] C. Wang, M. Adams, T. Luo, T. Jin, F. Luo, M. Gavaises, Hole-to-hole variations in coupled flow and spray simulation of a double-layer multi-holes diesel nozzle:, Int. J. Engine Res. 20 (2020) 3233–3246. https://doi.org/10.1177/1468087420963986.

[155] E. Gomez Santos, J. Shi, M. Gavaises, C. Soteriou, M. Winterbourn, W. Bauer, Investigation of cavitation and air entrainment during pilot injection in real-size multi-hole diesel nozzles, Fuel. 263 (2020) 716–746. https://doi.org/10.1016/j.fuel.2019.116746.

[156] M. Gold, R. Pearson, J. Turner, D. Sykes, V. Stetsyuk, G. de Sercey, C. Crua, M. Murali-Girija, F. Koukouvinis, M. Gavaises, Simulation and Measurement of Transient Fluid Phenomena within Diesel Injection, SAE Int. J. Adv. Curr. Pract. Mobil. 1 (2019) 291–305. https://doi.org/10.4271/2019-01-0066.

[157] N. Mitroglou, V. Stamboliyski, I.K. Karathanassis, K.S. Nikas, M. Gavaises, Cloud cavitation vortex shedding inside an injector nozzle, Exp. Therm. Fluid Sci. 84 (2017) 179–189. https://doi.org/10.1016/j.expthermflusci.2017.02.011.

[158] N. Mitroglou, M. Gavaises, J. Nouri, C. Arcoumanis, Cavitation inside enlarged and real-size fully transparent injector nozzles and its effect on near nozzle spray formation, DIPSI Workshop Droplet Impact Phenom. Spray Investig. Univ. Bergamo Italy. 26 (2011) 33–45. https://openaccess.city.ac.uk/id/eprint/1507.

[159] I.K. Karathanassis, K. Trickett, P. Koukouvinis, J. Wang, R. Barbour, M. Gavaises, Illustrating the effect of viscoelastic additives on cavitation and turbulence with X-ray imaging, Sci. Rep. 8 (2018) 14968. https://doi.org/10.1038/s41598-018-32996-w.

[160] P. Koukouvinis, G. Bergeles, M. Gavaises, A cavitation aggressiveness index within the Reynolds averaged Navier Stokes methodology for cavitating flows, J. Hydrodyn. Ser B. 27 (2015) 579–586. https://doi.org/10.1016/S1001-6058(15)60519-4.

[161] P. Koukouvinis, I. Karathanassis, M. Gavaises, Prediction of cavitation and induced erosion inside a high-pressure fuel pump, Int. J. Engine Res. 19 (2017) 360–373. https://doi.org/10.1177/1468087417708137.

[162] P. Koukouvinis, H. Naseri, M. Gavaises, Performance of turbulence and cavitation models in prediction of incipient and developed cavitation, Int. J. Engine Res. 18 (2016) 333–350. https://doi.org/10.1177/1468087416658604.

[163] A. Papoutsakis, A. Theodorakakos, E. Giannadakis, D. Papoulias, M. Gavaises, LES Predictions of the Vortical Flow Structures in Diesel Injector Nozzles, 2009. https://doi.org/10.4271/2009-01-0833.

[164] G. Schnerr Professor Dr.-Ing.habil, I. Sezal, S. Schmidt, Numerical investigation of three-dimensional cloud cavitation with special emphasis on collapse induced shock dynamics, Phys. Fluids. 20 (2008). https://doi.org/10.1063/1.2911039.

[165] C. Egerer, S. Hickel, S. Schmidt, N. Adams, Large-eddy simulation of turbulent cavitating flow in a micro channel, Phys. Fluids. 26 (2014) 085–102. https://doi.org/10.1063/1.4891325.

[166] Y.B. Guo, C. Liu, Mechanical Properties of Hardened AISI 52100 Steel in Hard Machining Processes, J. Manuf. Sci. Eng.-Trans. Asme. 124 (2002) 1–9. https://doi.org/10.1115/1.1413775.

[167] M. Cristofaro, W. Edelbauer, P. Koukouvinis, M. Gavaises, Influence of Diesel Fuel Viscosity on Cavitating Throttle Flow Simulations under Erosive Operation Conditions, ACS Omega. 5 (2020) 7182–7192. https://doi.org/10.1021/acsomega.9b03623.

[168] M. Cristofaro, W. Edelbauer, P. Koukouvinis, M. Gavaises, A numerical study on the effect of cavitation erosion in a diesel injector, Appl. Math. Model. 78 (2020) 200–216. https://doi.org/10.1016/j.apm.2019.09.002.

[169] M. Gavaises, A. Theodorakakos, N. Mitroglou, Simulation of heating effects caused by fuel pressurisation at 3000bar in Diesel fuel injectors, 8 th International Symposium on Cavitation CAV2012 – 216, in: 2013: pp. 1–7. https://doi.org/10.3850/978-981-07-2826-7_216.

[170] George Strotos Phoevos Koukou Andreas Theodorakakos and Manolis Gavaises, Quantification of Friction-induced Heating in tapered Diesel orifices,SIA International Conference on Diesel Powertrains, Int. Congr. SIA Powertrain. (2014).

[171] R. Payri, J. Gimeno, P. Martí-Aldaraví, M. Alarcón, A new approach to compute temperature in a liquid-gas mixture. Application to study the effect of wall nozzle temperature on a Diesel injector, Int. J. Heat Fluid Flow. 68 (2017) 79–86. https://doi.org/10.1016/j.ijheatfluidflow.2016.12.008.

[172] R. Salemi, P. Koukouvinis, G. Strotos, R. McDavid, L. Wang, J. Li, M. Marengo, M. Gavaises, Evaluation of friction heating in cavitating high pressure Diesel injector nozzles, J. Phys. Conf. Ser. Vol. 656 (2015) 083–120. https://doi.org/10.1088/1742-6596/656/1/012083.

[173] N.I. Kolev, Thermodynamic and transport properties of diesel fuel, in: N.I. Kolev (Ed.), Multiph. Flow Dyn. 3 Turbul. Gas Absorpt. Release Diesel Fuel Prop., Springer, 2007: pp. 269–302. https://doi.org/10.1007/978-3-540-71443-9_13.

[174] H.B. Rokni, J.D. Moore, A. Gupta, M.A. MHugh, M. Gavaises, Entropy scaling based viscosity predictions for hydrocarbon mixtures and diesel fuels up to extreme conditions, Fuel. 241 (2019) 1203–1213. https://doi.org/10.1016/j.fuel.2018.12.043.

[175] H.B. Rokni, A. Gupta, J.D. Moore, M.A. MHugh, B.A. Bamgbade, M. Gavaises, Purely predictive method for density, compressibility, and expansivity for hydrocarbon mixtures and diesel and jet fuels up to high temperatures and pressures, Fuel. 236 (2019) 1377–1390. https://doi.org/10.1016/j.fuel.2018.09.041.

[176] H.B. Rokni, J.D. Moore, A. Gupta, M.A. MHugh, R.R. Mallepally, M. Gavaises, General method for prediction of thermal conductivity for well-characterized hydrocarbon mixtures and fuels up to extreme conditions using entropy scaling, Fuel. 245 (2019) 594–604. https://doi.org/10.1016/j.fuel.2019.02.044.

[177] C. Rodriguez, H.B. Rokni, P. Koukouvinis, A. Gupta, M. Gavaises, Complex multicomponent real-fluid thermodynamic model for high-pressure Diesel fuel injection, Fuel. 257 (2019) 3. https://doi.org/10.1016/j.fuel.2019.115888.

[178] P. Koukouvinis, A. Vidal-Roncero, C. Rodriguez, M. Gavaises, L. Pickett, High pressure/high temperature multiphase simulations of dodecane injection to nitrogen: Application on ECN Spray-A, Fuel. 275 (2020) 24. https://doi.org/10.1016/j.fuel.2020.117871.

[179] A.J. Rowane, V. Mahesh Babu, H.B. Rokni, J.D. Moore, M. Gavaises, M. Wensing, A. Gupta, M.A. McHugh, Effect of Composition, Temperature, and Pressure on the Viscosities and Densities of Three Diesel Fuels, J. Chem. Eng. Data. 64 (2019) 5529–5547. https://doi.org/10.1021/acs.jced.9b00652.

[180] A.J. Rowane, R.R. Mallepally, A. Gupta, M. Gavaises, M.A. McHugh, High-Temperature, High-Pressure Viscosities and Densities of n-Hexadecane, 2,2,4,4,6,8,8-Heptamethylnonane, and Squalane Measured Using a Universal Calibration for a Rolling-Ball Viscometer/Densimeter, Ind. Eng. Chem. Res. 58 (2019) 4303–4316. https://doi.org/10.1021/acs.iecr.8b05952.

[181] A. Vidal, C. Rodriguez, P. Koukouvinis, M. Gavaises, M.A. McHugh, Modelling of Diesel fuel properties through its surrogates using Perturbed-Chain, Statistical Associating Fluid Theory:, Int. J. Engine Res. (2018) 1118–1133. https://doi.org/10.1177/1468087418801712.

[182] Modelling of Diesel fuel properties through its surrogates using Perturbed-Chain, Statistical Associating Fluid Theory - Alvaro Vidal, Carlos Rodriguez, Phoevos Koukouvinis, Manolis Gavaises, Mark A McHugh, 2020, (n.d.). https://journals.sagepub.com/doi/abs/10.1177/1468087418801712 (accessed October 30, 2020).

[183] I. Demirdžić, M. Perić, Space conservation law in finite volume calculations of fluid flow, Int. J. Numer. Methods Fluids. 8 (1988) 1037–1050. https://doi.org/10.1002/fld.1650080906.

[184] F. Ducros, N. Franck, T. Poinsot, Wall-Adapting Local Eddy-Viscosity Models for Simulations in Complex Geometries, Numer. Methods Fluid Dyn. VI. (1998) 293–300. https://doi.org/0952492911.

[185] N. Kyriazis, P. Koukouvinis, M. Gavaises, Modelling cavitation during drop impact on solid surfaces, Adv. Colloid Interface Sci. 260 (2018) 46–64. https://doi.org/10.1016/j.cis.2018.08.004.

[186] S. Schmidt, I. Sezal, G. Schnerr Professor Dr.-Ing.habil, M. Talhamer, Riemann Techniques for the Simulation of Compressible Liquid Flows with Phase-Transistion at all Mach Numbers - Shock and Wave Dynamics in Cavitating 3-D Micro and Macro Systems, in: 2008: p. Session: TP-8: Computational Multi-Phase Flow. https://doi.org/10.2514/6.2008-1238.

[187] E.F. Toro, Riemann Solvers and Numerical Methods for Fluid Dynamics: A Practical Introduction, 3rd ed., Springer-Verlag, 2009. https://doi.org/10.1007/b79761.

[188] E. Lemmon, M. Huber, Thermodynamic Properties of n-Dodecane, Energy Fuels. 18 (2004) 960–967. https://doi.org/10.1021/ef0341062.

[189] J. Gross, G. Sadowski, Perturbed-Chain SAFT: An Equation of State Based on a Perturbation Theory for Chain Molecules, Ind. Eng. Chem. Res. 40 (2001) 1244–1260. https://doi.org/10.1021/ie0003887.

[190] M. Hopp, J. Gross, Thermal Conductivity from Entropy Scaling: A Group-Contribution Method, Ind. Eng. Chem. Res. 58 (2019) 20441–20449. https://doi.org/10.1021/acs.iecr.9b04289.

[191] O. Lötgering-Lin, J. Gross, Group Contribution Method for Viscosities Based on Entropy Scaling Using the Perturbed-Chain Polar Statistical Associating Fluid Theory, Ind. Eng. Chem. Res. 54 (2015) 7942–7952. https://doi.org/10.1021/acs.iecr.5b01698.

[192] V. Vinš, B. Planková, J. Hrubý, Surface Tension of Binary Mixtures Including Polar Components Modeled by the Density Gradient Theory Combined with the PC-SAFT Equation of State, Int. J. Thermophys. 34 (2013) 792–812. https://doi.org/10.1007/s10765-012-1207-z.

[193] M.J. Ivings, D.M. Causon, E.F. Toro, On Riemann solvers for compressible liquids, Int. J. Numer. Methods Fluids. 28 (1998) 395–418. https://doi.org/10.1002/(SICI)1097-0363(19980915).

[194] F.A. Jaberi, P.J. Colucci, Large eddy simulation of heat and mass transport in turbulent flows. Part 1: Velocity field, Int. J. Heat Mass Transf. 46 (2003) 1811–1825. https://doi.org/10.1016/S0017-9310(02)00484-2.

[195] C. Mueller, W. Cannella, J. Bays, T. Bruno, K. DeFabio, H.D. Dettman, R. Gieleciak, M. Huber, C.-B. Kweon, S.S. McConnell, W. Pitz, M. Ratcliff, Diesel Surrogate Fuels for Engine Testing and Chemical-Kinetic Modeling: Compositions and Properties, (2016) 1445–1461. https://doi.org/10.1021/ACS.ENERGYFUELS.5B02879.

[196] F. Caupin, A.D. Stroock, The Stability Limit and other Open Questions on Water at Negative Pressure, in: Liq. Polymorph., John Wiley & Sons, Ltd, 2013: pp. 51–80. https://doi.org/10.1002/9781118540350.ch3.

[197] D. Trevena, Cavitation and the generation of tension in liquids, J. Phys. Appl. Phys. 17 (2000) 2139–2164. https://doi.org/10.1088/0022-3727/17/11/003.

[198] I. Karathanassis, P. Koukouvinis, E. Kontolatis, Z. Li, J. Wang, N. Mitroglou, M. Gavaises, High-speed visualization of vortical cavitation using synchrotron radiation, J. Fluid Mech. 838 (2018) 148–164. https://doi.org/10.1017/jfm.2017.885.

[199] B.A. Reid, M. Gavaises, N. Mitroglou, G.K. Hargrave, C.P. Garner, E.J. Long, R.M. McDavid, On the formation of string cavitation inside fuel injectors, Exp. Fluids. 55 (2014) 001–013. https://doi.org/10.1007/s00348-013-1662-8.

[200] M. Dular, R. Bachert, The issue of Strouhal number definition in cavitating flow, J. Mech. Eng. 55 (2009) 666–674. http://dx.doi.org/10.1063/1.3699067.

[201] D. Cecere, A. Ingenito, E. Giacomazzi, L. Romagnosi, C. Bruno, Hydrogen/air supersonic combustion for future hypersonic vehicles, Int. J. Hydrog. Energy. 36 (2011) 11969–11984. https://doi.org/10.1016/j.ijhydene.2011.06.051.

[202] X. Long, Q. Liu, B. Ji, Y. Lu, Numerical investigation of two typical cavitation shedding dynamics flow in liquid hydrogen with thermodynamic effects, Int. J. Heat Mass Transf. 109 (2017) 879–893. https://doi.org/10.1016/j.ijheatmasstransfer.2017.02.063.

[203] P.F. Pelz, T. Keil, T.F. Groß, The transition from sheet to cloud cavitation, J. Fluid Mech. 817 (2017) 439–454. https://doi.org/10.1017/jfm.2017.75.

[204] C.E. Brennen, Hydrodynamics of Pumps, Concepts ETI, 1994. https://doi.org/10.1017/CBO9780511976728.

[205] G.K. Batchelor, An Introduction to Fluid Dynamics, Cambridge University Press, 1973. https://doi.org/10.1017/CBO9780511800955.

[206] K.-H. Kim, G. Chahine, J.-P. Franc, A. Karimi, Advanced Experimental and Numerical Techniques for Cavitation Erosion Prediction, Springer, 2014. ISBN: 978-94-017-8539-6.

[207] U.N. Environment, Emissions Gap Report 2020, UNEP - UN Environ. Programme. (2020). http://www.unenvironment.org/emissions-gap-report-2020.

[208] R. Lemaire, A. Faccinetto, E. Therssen, M. Ziskind, C. Focsa, P. Desgroux, Experimental comparison of soot formation in turbulent flames of Diesel and surrogate Diesel fuels, Proc. Combust. Inst. 32 (2009) 737–744. https://doi.org/10.1016/j.proci.2008.05.019.

[209] S. Kook, L.M. Pickett, Liquid length and vapor penetration of conventional, Fischer–Tropsch, coal-derived, and surrogate fuel sprays at high-temperature and high-pressure ambient conditions, Fuel. 93 (2012) 539–548. https://doi.org/10.1016/j.fuel.2011.10.004.

[210] M. Hawi, H. Kosaka, S. Sato, T. Nagasawa, A. Elwardany, M. Ahmed, Effect of injection pressure and ambient density on spray characteristics of diesel and biodiesel surrogate fuels, Fuel. 254 (2019) 138–151. https://doi.org/10.1016/j.fuel.2019.115674.

[211] R. Payri, J.P. Viera, Y. Pei, S. Som, Experimental and numerical study of lift-off length and ignition delay of a two-component diesel surrogate, Fuel. 158 (2015) 957–967. https://doi.org/10.1016/j.fuel.2014.11.072.

[212] A.J. Donkerbroek, M.D. Boot, C.C.M. Luijten, N.J. Dam, J.J. ter Meulen, Flame lift-off length and soot production of oxygenated fuels in relation with ignition delay in a DI heavy-duty diesel engine, Combust. Flame. 158 (2011) 525–538. https://doi.org/10.1016/j.combustflame.2010.10.003.

[213] Z. Han, A. Uludogan, G. Hampson, R. Reitz, Mechanism of Soot and NOx Emission Reduction Using Multiple-Injection in a Diesel Engine, SAE Trans. 105 (1996) 837–852. https://doi.org/10.4271/960633.

[214] N.M. Ribeiro, A.C. Pinto, C.M. Quintella, G.O. da Rocha, L.S.G. Teixeira, L.L.N. Guarieiro, M. do Carmo Rangel, M.C.C. Veloso, M.J.C. Rezende, R. Serpa da Cruz, A.M. de Oliveira, E.A. Torres, J.B. de Andrade, The Role of Additives for Diesel and Diesel Blended (Ethanol or Biodiesel) Fuels: A Review, Energy Fuels. 21 (2007) 2433–2445. https://doi.org/10.1021/ef070060r.

[215] F. Payri, J.V. Pastor, J.-G. Nerva, J.M. Garcia-Oliver, Lift-Off Length and KL Extinction Measurements of Biodiesel and Fischer-Tropsch Fuels under Quasi-Steady Diesel Engine Conditions, SAE Int. J. Engines. 4 (2011) 2278–2297. https://doi.org/10.4271/2011-24-0037.

[216] L.M. Pickett, D.L. Siebers, Soot in diesel fuel jets: effects of ambient temperature, ambient density, and injection pressure, Combust. Flame. 138 (2004) 114–135. https://doi.org/10.1016/j.combustflame.2004.04.006.

[217] G.E. Riva, A. Reggiori, G. Daminelli, Diesel Spray Combustion Rate Enhancement by Increasing Injection Pressure, SAE International, 1993. https://doi.org/10.4271/930926.

[218] M. Gavaises, Flow in valve covered orifice nozzles with cylindrical and tapered holes and link to cavitation erosion and engine exhaust emissions, Int. J. Engine Res. 9 (2008) 435–447. https://doi.org/10.1243/14680874JER01708.

[219] R. Payri, F.J. Salvador, J. Gimeno, L.D. Zapata, Diesel nozzle geometry influence on spray liquid-phase fuel penetration in evaporative conditions, Fuel. 87 (2008) 1165–1176. https://doi.org/10.1016/j.fuel.2007.05.058.

[220] A. Vidal, K. Kolovos, M.R. Gold, R.J. Pearson, P. Koukouvinis, M. Gavaises, Preferential cavitation and friction-induced heating of multi-component Diesel fuel surrogates up to 450MPa, Int. J. Heat Mass Transf. 166 (2021) 24. https://doi.org/10.1016/j.ijheatmasstransfer.2020.120744.

[221] Konstantinos Kolovos, Nikolaos Kyriazis, Phoevos Koukouvinis, Manolis Gavaises, Jason Z. Li, Robert M. McDavid, Large-eddy simulation of friction heating and turbulent cavitating flow in a Diesel injector including needle movement, Appl. Energy Combust. Sci. 14 (2020) 18. https://doi.org/10.3390/en14102923.

[222] E. Gomez Santos, J. Shi, R. Venkatasubramanian, G. Hoffmann, M. Gavaises, W. Bauer, Modelling and prediction of cavitation erosion in GDi injectors operated with E100 fuel, Fuel. 289 (2021) 119–923. https://doi.org/10.1016/j.fuel.2020.119923.

[223] C. Wang, M. Adams, T. Jin, Y. sun, A. Röll, F. Luo, M. Gavaises, An analytical model of diesel injector’s needle valve eccentric motion, Int. J. Engine Res. (2021) 146–164. https://doi.org/10.1177/1468087420987367.

[224] D.P. Schmidt, M.L. Corradini, The internal flow of diesel fuel injector nozzles: A review, Int. J. Engine Res. 2 (2001) 1–22. https://doi.org/10.1243/1468087011545316.

[225] J. Manin, M. Bardi, L.M. Pickett, R. Payri, Boundary condition and fuel composition effects on injection processes of high-pressure sprays at the microscopic level, Int. J. Multiph. Flow. 83 (2016) 267–278. https://doi.org/10.1016/j.ijmultiphaseflow.2015.12.001.

[226] W. Yuan, G.H. Schnerr, Numerical Simulation of Two-Phase Flow in Injection Nozzles: Interaction of Cavitation and External Jet Formation, J. Fluids Eng. 125 (2004) 963–969. https://doi.org/10.1115/1.1625687.

[227] M. GAVAISES, Modeling of diesel fuel injection processes, Ph Thesis Imp. Coll. Univ. Lond. (1997) 76–80.

[228] R. Payri, S. Molina, F.J. Salvador, J. Gimeno, A study of the relation between nozzle geometry, internal flow and sprays characteristics in diesel fuel injection systems, KSME Int. J. 18 (2004) 1222–1235. https://doi.org/10.1007/BF02983297.

[229] R. Payri, F.J. Salvador, A. García, A. Gil, Combination of Visualization Techniques for the Analysis of Evaporating Diesel Sprays, Energy Fuels. 26 (2012) 5481–5490. https://doi.org/10.1021/ef3008823.

[230] R.P. Fitzgerald, G.D. Vecchia, J.E. Peraza, G.C. Martin, Features of Internal Flow and Spray for a Multi-Hole Transparent Diesel Fuel Injector Tip, (2019) 9. https://ilass19.sciencesconf.org/246151.

[231] W. Yuan, J. Sauer, G.H. Schnerr, Modeling and computation of unsteady cavitation flows in injection nozzles, Mécanique Ind. 2 (2001) 383–394. https://doi.org/DOI:10.1016/S1296-2139(01)01120-4.

[232] M. Battistoni, S. Som, D.E. Longman, Comparison of Mixture and Multifluid Models for In-Nozzle Cavitation Prediction, J. Eng. Gas Turbines Power. 136 (2014) 12. https://doi.org/10.1115/1.4026369.

[233] C. Habchi, N. Dumont, O. Simonin, Multidimentional Simulation of Cavitating Flows in Diesel Injectors by a Homogeneous Mixture Modeling Approach, At. Sprays. 18 (2008) 129–162. https://doi.org/10.1615/AtomizSpr.v18.i2.20.

[234] J.W. Lindau, R.F. Kunz, D.A. Boger, D.R. Stinebring, H.J. Gibeling, High Reynolds Number, Unsteady, Multiphase CFD Modeling of Cavitating Flows, J. Fluids Eng. 124 (2002) 607–616. https://doi.org/10.1115/1.1487360.

[235] F. Peng Kärrholm, H. Weller, N. Nordin, Modelling Injector Flow Including Cavitation Effects for Diesel Applications, in: 2007: pp. 465–474. https://doi.org/10.1115/FEDSM2007-37518.

[236] H. Liu, J. Ma, F. Dong, Y. Yang, X. Liu, G. Ma, Z. Zheng, M. Yao, Experimental investigation of the effects of diesel fuel properties on combustion and emissions on a multi-cylinder heavy-duty diesel engine, Energy Convers. Manag. 171 (2018) 1787–1800. https://doi.org/10.1016/j.enconman.2018.06.089.

[237] N.I. Kolev, Multiphase Flow Dynamics 2: Mechanical Interactions, 4th ed., Springer-Verlag, 2012. https://doi.org/10.1007/978-3-642-20598-9.

[238] E.W. Lemmon, M.L. Huber, M.O. McLinden, Nist Standard Reference Database 23: Reference Fluid Thermodynamic and Transport Properties-Refprop, Version 8.0, (2007). https://www.nist.gov/publications/nist-standard-reference-database-23-reference-fluid-thermodynamic-and-transport-0.

[239] S.H. Park, H.K. Suh, C.S. Lee, Effect of Bioethanol−Biodiesel Blending Ratio on Fuel Spray Behavior and Atomization Characteristics, Energy Fuels. 23 (2009) 4092–4098. https://doi.org/10.1021/ef900068a.

[240] S.H. Park, S.H. Kim, C.S. Lee, Mixing Stability and Spray Behavior Characteristics of Diesel−Ethanol−Methyl Ester Blended Fuels in a Common-Rail Diesel Injection System, Energy Fuels. 23 (2009) 5228–5235. https://doi.org/10.1021/ef9004847.

[241] S.L. Toth, Experimental Study of Droplet Vaporization and Combustion of Diesel, Biodiesel and their blends in a Turbulent Environment at Elevated Pressure and Temperature Conditions, 187 (2015) 160. https://doi.org/DOI:10.1080/00102202.2014.991867.

[242] L. Zhang, S.-C. Kong, High-pressure vaporization modeling of multi-component petroleum–biofuel mixtures under engine conditions, Combust. Flame. 158 (2011) 1705–1717. https://doi.org/10.1016/j.combustflame.2011.01.002.

[243] G. Strotos, M. Gavaises, A. Theodorakakos, G. Bergeles, Numerical investigation of the evaporation of two-component droplets, Fuel. 90 (2011) 1492–1507. https://doi.org/10.1016/j.fuel.2011.01.017.

[244] G. Bergeles, Influence of species concentration on the evaporation of suspended multicomponent droplets, (n.d.). https://www.academia.edu/11547039/Influence_of_species_concentration_on_the_evaporation_of_suspended_multicomponent_droplets.

[245] O. Samimi Abianeh, C.P. Chen, A discrete multicomponent fuel evaporation model with liquid turbulence effects, Int. J. Heat Mass Transf. 55 (2012) 6897–6907. https://doi.org/10.1016/j.ijheatmasstransfer.2012.07.003.

[246] M.S. Wertheim, Fluids with highly directional attractive forces. I. Statistical thermodynamics, J. Stat. Phys. 35 (1984) 19–34. https://doi.org/10.1007/BF01017362.

[247] M.S. Wertheim, Fluids with highly directional attractive forces. II. Thermodynamic perturbation theory and integral equations, J. Stat. Phys. 35 (1984) 35–47. https://doi.org/10.1007/BF01017363.

[248] M.S. Wertheim, Fluids with highly directional attractive forces. III. Multiple attraction sites, J. Stat. Phys. 42 (1986) 459–476. https://doi.org/10.1007/BF01127721.

[249] M.S. Wertheim, Fluids with highly directional attractive forces. IV. Equilibrium polymerization, J. Stat. Phys. 42 (1986) 477–492. https://doi.org/10.1007/BF01127722.

[250] A.J. de Villiers, C.E. Schwarz, A.J. Burger, G.M. Kontogeorgis, Evaluation of the PC-SAFT, SAFT and CPA equations of state in predicting derivative properties of selected non-polar and hydrogen-bonding compounds, Fluid Phase Equilibria. 338 (2013) 1–15. https://doi.org/10.1016/j.fluid.2012.09.035.

[251] S. Leekumjorn, K. Krejbjerg, Phase behavior of reservoir fluids: Comparisons of PC-SAFT and cubic EOS simulations, Fluid Phase Equilibria. 359 (2013) 17–23. https://doi.org/10.1016/j.fluid.2013.07.007.

[252] D.-Y. Peng, D.B. Robinson, A New Two-Constant Equation of State, Ind. Eng. Chem. Fundam. 15 (1976) 59–64. https://doi.org/10.1021/i160057a011.

[253] G. Soave, Equilibrium constants from a modified Redlich-Kwong equation of state, Chem. Eng. Sci. 27 (1972) 1197–1203. https://doi.org/10.1016/0009-2509(72)80096-4.

[254] W. Yan, F. Varzandeh, E.H. Stenby, PVT modeling of reservoir fluids using PC-SAFT EoS and Soave-BWR EoS, Fluid Phase Equilibria. 386 (2015) 96–124. https://doi.org/10.1016/j.fluid.2014.11.022.

[255] W.A. Burgess, D. Tapriyal, B.D. Morreale, Y. Soong, H.O. Baled, R.M. Enick, Y. Wu, B.A. Bamgbade, M.A. McHugh, Volume-translated cubic EoS and PC-SAFT density models and a free volume-based viscosity model for hydrocarbons at extreme temperature and pressure conditions, Fluid Phase Equilibria. 359 (2013) 38–44. https://doi.org/10.1016/j.fluid.2013.07.016.

[256] K. Schou Pedersen, C. Hasdbjerg, PC-SAFT Equation of State Applied to Petroleum Reservoir Fluids, in: OnePetro, 2007. https://doi.org/10.2118/110483-MS.

[257] M.F. Gord, M. Roozbahani, H.R. Rahbari, S.J.H. Hosseini, Modeling thermodynamic properties of natural gas mixtures using perturbed-chain statistical associating fluid theory, Russ. J. Appl. Chem. 86 (2013) 867–878. https://doi.org/10.1134/S1070427213060153.

[258] OpenFOAM 2.4.0, OpenFOAM. (n.d.). https://openfoam.org/version/2-4-0/ (accessed May 22, 2019).

[259] R. Payri, B. Tormos, J. Gimeno, G. Bracho, The potential of Large Eddy Simulation (LES) code for the modeling of flow in diesel injectors, Math. Comput. Model. 52 (2010) 1151–1160. https://doi.org/10.1016/j.mcm.2010.02.033.

[260] F. Nicoud, F. Ducros, Subgrid-Scale Stress Modelling Based on the Square of the Velocity Gradient Tensor, Flow Turbul. Combust. 62 (1999) 183–200. https://doi.org/10.1023/A:1009995426001.

[261] Fangqing Liu, A Thorough Description Of How Wall Functions Are Implemented In OpenFOAM. In Proceedings of CFD with OpenSource Software, (2016) 34, (n.d.). http://www.tfd.chalmers.se/~hani/kurser/OS_CFD_2016/FangqingLiu/openfoamFinal.pdf (accessed April 6, 2021).

[262] A. Vidal, P. Koukouvinis, M. Gavaises, Vapor-liquid equilibrium calculations at specified composition, density and temperature with the perturbed chain statistical associating fluid theory (PC-SAFT) equation of state, Fluid Phase Equilibria. 521 (2020) 29. https://doi.org/10.1016/j.fluid.2020.112661.

[263] R. Saurel, F. Petitpas, R. Abgrall, Modelling phase transition in metastable liquids: application to cavitating and flashing flows, J. Fluid Mech. 607 (2008) 313–350. https://doi.org/10.1017/S0022112008002061.

[264] M. Hopp, J. Gross, Thermal Conductivity of Real Substances from Excess Entropy Scaling Using PCP-SAFT, Ind. Eng. Chem. Res. 56 (2017) 4527–4538. https://doi.org/10.1021/acs.iecr.6b04289.

[265] B.A. Reid, G.K. Hargrave, C.P. Garner, G. Wigley, An investigation of string cavitation in a true-scale fuel injector flow geometry at high pressure, Phys. Fluids. 22 (2010) 031703. https://doi.org/10.1063/1.3372174.

[266] G. Strotos, P. Koukouvinis, A. Theodorakakos, M. Gavaises, L. Wang, J. Li, R.M. McDavid, Fuel heating in high pressure diesel nozzles, Thiesel Valencia Spain. (2014) 10. https://doi.org/10.1016/j.ijheatfluidflow.2014.10.010.

[267] R. Salemi, R. McDavid, P. Koukouvinis, M. Gavaises, M. Marengo, Steady State and Transient, Non-isothermal Modeling of Cavitations in Diesel Fuel Injectors, in: 27th Annu. Conf. Liq. At. Spray Syst. ILASS Am. Conf., Journal of Physics: Conference Series Volume 656, Proceedings of the 9th International Symposium on Cavitation, CAV2015, December 6-10, Lausanne, Switzerland, 2015.

[268] M. Cristofaro, W. Edelbauer, M. Gavaises, P. Koukouvinis, Numerical simulation of compressible cavitating two-phase flows with a pressure-based solver, in: Ilass Eur. 28th Eur. Conf. Liq. At. Spray Syst., Editorial Universitat Politècnica de València, 2017: pp. 896–903. https://doi.org/10.4995/ILASS2017.2017.4629.

[269] H. Naseri, V. Koivunen, Convex Relaxation for Maximum-Likelihood Network Localization Using Distance and Direction Data, in: 2018 IEEE 19th Int. Workshop Signal Process. Adv. Wirel. Commun. SPAWC, 2018: pp. 1–5. https://doi.org/10.1109/SPAWC.2018.8445850.

[270] J. Dumond, F. Magagnato, A. Class, Stochastic-field cavitation model, Phys. Fluids. 25 (2013) 1–28. https://doi.org/10.1063/1.4813813.

[271] M.H. Arabnejad, A. Amini, M. Farhat, R.E. Bensow, Numerical and experimental investigation of shedding mechanisms from leading-edge cavitation, Int. J. Multiph. Flow. 119 (2019) 123–143. https://doi.org/10.1016/j.ijmultiphaseflow.2019.06.010.

[272] V.K. Kedrinskiy, Hydrodynamics of Explosion: Experiments and Models, Springer Science & Business Media, 2006. https://doi.org/10.1007/3-540-28563-6.

[273] C. Wang, A. Moro, F. Xue, X. Wu, F. Luo, The influence of eccentric needle movement on internal flow and injection characteristics of a multi-hole diesel nozzle, Int. J. Heat Mass Transf. 117 (2018) 818–834. https://doi.org/10.1016/j.ijheatmasstransfer.2017.10.057.

[274] W.H. Nurick, Orifice Cavitation and Its Effect on Spray Mixing, J. Fluids Eng. 98 (1976) 681–687. https://doi.org/10.1115/1.3448452.

[275] N. Mitroglou, M. McLorn, M. Gavaises, C. Soteriou, M. Winterbourne, Instantaneous and ensemble average cavitation structures in Diesel micro-channel flow orifices, Fuel. 116 (2014) 736–742. https://doi.org/10.1016/j.fuel.2013.08.060.

[276] R. Fortes Patella, T. Choffat, J.-L. Reboud, A. Archer, Mass loss simulation in cavitation erosion: Fatigue criterion approach, Wear. 300 (2013) 205–215. https://doi.org/10.1016/j.wear.2013.01.118.

[277] C.E. Brennen, Cavitation and Bubble Dynamics, Cambridge University Press, Cambridge, 2013. https://doi.org/10.1017/CBO9781107338760.

[278] J. Safarov, U. Ashurova, B. Ahmadov, E. Abdullayev, A. Shahverdiyev, E. Hassel, Thermophysical properties of Diesel fuel over a wide range of temperatures and pressures, Fuel. 216 (2018) 870–889. https://doi.org/10.1016/j.fuel.2017.11.125.

[279] M. Dular, O. Coutier-Delgosha, Numerical modelling of cavitation erosion, Int. J. Numer. Methods Fluids. 61 (2009) 1388–1410. https://doi.org/10.1002/fld.2003.

[280] A. Montorfano, F. Piscaglia, A. Onorati, A Moving Mesh Strategy to Perform Adaptive Large Eddy Simulation of IC Engines in OpenFOAM, in: 2014. https://doi.org/10.13140/RG.2.1.2269.8325.

[281] C.E. Brennen, Cavitation in Biological and Bioengineering Contexts, in: 2003. http://flow.me.es.osaka-u.ac.jp/cav2003/ILpaper/Cav03-IL-1.pdf.

[282] B.H. Maines, C.E. Brennen, Lumped parameter model for computing the minimum pressure during mechanical heart valve closure, J. Biomech. Eng. 127 (2005) 648–655. https://doi.org/10.1115/1.1934164.

[283] C. Brennen, Cavitation in Biological and Bioengineering Contexts, (2003). http://flow.me.es.osaka-u.ac.jp/cav2003/ILpaper/Cav03-IL-1.pdf.

[284] C.E. Brennen, Cavitation in medicine, Interface Focus. 5 (2015). https://doi.org/10.1098/rsfs.2015.0022.

[285] C. Brennen, Hydrodynamics of Pumps, Cambridge University Press, Cambridge, 2011. https://doi.org/10.1017/CBO9780511976728.